

UNIVERSIDADE DE LISBOA  
FACULDADE DE CIÊNCIAS  
DEPARTAMENTO DE FÍSICA



# **Mapping Microstructural Dynamics in a Mouse Stroke Model Using Advanced Diffusion MRI**

Rita Beatriz Ruivo Alves

**Mestrado Integrado em Engenharia Biomédica e Biofísica**  
Perfil em Sinais e Imagens Médicas

Dissertação orientada por:  
Noam Shemesh, PhD, Champalimaud Centre for the Unknown, Portugal  
Alexandre Andrade, PhD, Faculdade de Ciências da Universidade de Lisboa, Portugal



## ACKNOWLEDGMENTS

---

First of all, I would like to express my gratitude to my supervisor Dr. Noam Shemesh, for all the help, guidance and knowledge he has so joyfully provided me with, even in such an atypical year.

Over these months I got the opportunity to be in a lab where learning was part of a constant journey and I could not be more grateful. I would like to thank Rafael for his time, patience and important advice, Francisca for all the help, kindness and art attacks since the beginning, Beatriz for the tachycardiac yet blissful and didactic adventures, Cris for keeping us on balance and happy, and all the lab members for being always so nice and helpful.

I would also like to thank my internal supervisor Dr. Alexandre Andrade for the availability and clarifications throughout the traineeship.

Last but not the least, a special thanks to my sister Ana for all the inspiration and company, and to my parents for all the patience and support.



## ABSTRACT

---

Stroke is a leading cause of long-term disability and death worldwide, with ischaemic infarct accounting for approximately 80% of all cases. Currently, novel treatments depend on a deeper understanding of the local tissue milieu following ischemia. Therefore, non-invasive neuroimaging plays a crucial role in stroke research. Diffusion MRI (dMRI) is one of the most reliable imaging techniques, mainly for the early detection of ischemic stroke via detection of microstructural changes. However, dMRI is critically unspecific, thereby hampering the conclusive characterization of infarct core, salvageable tissue and response to treatment. To overcome this drawback, Correlation Tensor Imaging (CTI) – a ground-breaking approach enhancing sensitivity and specificity towards tissue microstructure via the resolution of non-Gaussian diffusion sources – was applied for the first time towards the characterization of ischemic tissue (*ex vivo* and *in vivo*) and assessment of the mechanisms underlying dMRI contrasts in a mouse stroke model at an early stage post ischemic insult. In this study, a photothrombotic stroke model was used to induce a focal infarct in the barrel cortex and dMRI *ex vivo* datasets were acquired with CTI pulse sequences written in house. For corroboration of results, *in vivo* datasets were additionally acquired. The stroke model reproducibly induced well-delimited infarction cores in the targeted region in all animals. Our results suggest that CTI is capable of resolving microscopic features of ischemic tissue in-vivo, which until now were obfuscated or conflated in conventional dMRI measurements. Particularly, intra-compartmental kurtosis ( $K_{intra}$ ), one of the resolved sources, shows higher sensitivity and specificity towards ischemic alterations when compared to other sources of kurtosis. These are critical first steps towards resolving the contributions of cytotoxic and vasogenic edema sources as well as potential for revealing salvageable tissue or ongoing excitotoxicity.

**Keywords:** Diffusion MRI, Stroke, Ischemia, Mouse model



## RESUMO

---

O acidente vascular cerebral (AVC) corresponde a uma das principais causas de morte e invalidez a nível mundial, sendo o AVC isquémico o mais predominante, perfazendo mais de 80% dos casos. Este traduz-se no bloqueio de um ou mais vasos sanguíneos devido à formação de coágulos, comprometendo a oxigenação no local e o fornecimento de nutrientes como consequência da redução do fluxo sanguíneo. O único tratamento aceite para o AVC baseia-se na administração de agentes trombolíticos. Porém, a sua aplicabilidade é muito reduzida pois o intervalo de tempo exigido para a sua atuação é demasiado curto (menos de 4 horas desde a última vez em que o sujeito se apresentou assintomático). De momento, o desenvolvimento de técnicas inovadoras encontra-se dependente de um conhecimento mais aprofundado do tecido envolvente no decorrer do acidente isquémico. Posto tal, as técnicas de neuroimagiologia de cariz não invasivo, como a imagem por ressonância magnética (IRM), apresentam um papel crucial na investigação nesta área. A importância da ressonância magnética de difusão (dMRI, do inglês *diffusion MRI*) tem vindo a ser cada vez mais favorecida, especialmente na deteção do enfarte e no estudo do microambiente na zona respetiva. Contudo, as métricas convencionais de dMRI apenas disponibilizam informação relativa, no máximo, a um sumatório de efeitos não Gaussianos da difusão da água nos tecidos, o que a torna numa técnica consideravelmente inespecífica. Esta falta de especificidade pode então refletir-se numa incorreta caracterização do núcleo da lesão, de tecido recuperável e da resposta ao tratamento, no sentido em que os mecanismos subjacentes ao contraste de dMRI obtido são desconhecidos. No âmbito deste trabalho, de forma a aumentar a sensibilidade e especificidade da dMRI na informação obtida em contexto de AVC isquémico, a metodologia de imagem por contraste do tensor de correlação (CTI, do inglês *Correlation Tensor Imaging*), desenvolvida no nosso laboratório, foi aplicada num modelo de AVC isquémico em murgancho (*Mus musculus*). A CTI permite a obtenção de informações mais específicas acerca de efeitos de difusão provenientes das fontes de curtos (relativos a anisotropia, dispersão na orientação, variância na difusão nos tecidos e propriedades não Gaussianas). Esta técnica baseia-se na expansão cumulativa do sinal adquirido em sequências avançadas de codificação de difusão dupla (DDE, do inglês *Double Diffusion Encoding*), em que ambas as codificações podem ser aplicadas em direções e magnitudes independentes (caracterizadas por vetores independentes  $q_1$  e  $q_2$ ).

Todos os procedimentos em animais foram previamente aprovados pelas autoridades nacionais e internacionais competentes, e foram realizados de acordo com a Diretiva EU 2010/63. Murganhos macho C57BL/6J (N = 12;  $26,4 \pm 6,5$  g) com 11 semanas foram utilizados. O modelo fototrombótico de Rose Bengal foi usado de forma a induzir um enfarte focalizado na região do córtex de barril com uma solução de um corante fotossensível (15 mg/ml). Em animais do grupo experimental (N = 5), a solução foi administrada de forma intravenosa (10 µl/g peso do animal) e a zona cortical de interesse foi irradiada com uma fonte de luz fria durante 15 minutos. Os animais do grupo de controlo (N = 5) foram submetidos a procedimentos idênticos, à exceção da irradiação responsável pelo desencadeamento da lesão, mantendo o tempo de espera suposto. Os cérebros do grupo de AVC e do grupo de controlo foram perfundidos 3 h após o fim do período com ou sem iluminação e utilizados para aquisições *ex vivo*. Além disso, dois animais foram usados para examinação *in vivo*: um submetido à indução do AVC para validação com os resultados *ex vivo*, e outro animal saudável foi usado para efeitos corroborativos com estudos anteriores.

Os cérebros foram examinados no scanner Aeon da Bruker de 16.4 T. As imagens por difusão *ex vivo* foram adquiridas com sequências de DDE com base em EPI (do inglês *Echo Planar Imaging*) escritas *in house*. Usou-se um protocolo com um total de 5 combinações  $q_1$ - $q_2$  de magnitudes diferentes (1498,0 – 0; 1059,2 – 1059,2; 1059,2 – 0; 749,0 – 749,0 e 749,0 – 0 mT/m), associando cada combinação a uma aquisição. Para combinações em que as magnitudes eram iguais entre vetores, foram usadas 135 direções paralelas e perpendiculares, resultando em 7 aquisições com valor b total de 750, 1500 ou 3000

mm/s<sup>2</sup>. Os restantes parâmetros foram: TR/TE = 3000/49 ms, FOV = 11 × 11 mm<sup>2</sup>, matriz = 78 × 78, resolução de voxel no plano de 141 × 141 μm<sup>2</sup>, 25 fatias coronais com espessura de 0,5 mm, δ/Δ/τ<sub>m</sub> = 1,5/10/10 ms e 2 segmentos. 20 imagens foram adquiridas sem gradientes de difusão aplicados (i.e., b = 0 mm/s<sup>2</sup>). Cada exame durou aproximadamente 14 h na totalidade.

No caso das aquisições *in vivo*, os animais foram sedados (isoflurano 2,5%) e examinados no scanner *Biospec* da *Bruker* de 9.4 T. As imagens por difusão foram adquiridas com um protocolo otimizado em comparação com o utilizado nas sequências *ex vivo*, diferindo nos seguintes parâmetros: as combinações  $q_1$ - $q_2$  de magnitude foram de 518,79 – 0; 366,84 – 366,84; 366,84 – 0; 259,4 – 259,4 e 259,4 – 0 mT/m. As combinações de direções foram idênticas às utilizadas nas aquisições *ex vivo*, resultando também em 7 aquisições com valor b total de 625, 1250 ou 1500 mm/s<sup>2</sup>, TR/TE = 2800/44,5 ms, FOV = 12 × 12 mm<sup>2</sup>, matriz = 78 × 78, resolução de voxel no plano de 181 × 181 μm<sup>2</sup>, 5 fatias coronais com espessura de 0,85 mm, δ/Δ/τ<sub>m</sub> = 4/10/10 ms e 1 segmento. Cada exame durou aproximadamente 1 h e 15 min.

O processamento dos dados englobou a correção do sinal ao nível do ruído, alinhamento dos dados e correção ao nível de *Gibbs ringing*. As métricas de difusão convencionais, tais como a difusão média, a anisotropia fracional, a difusão radial e axial (MD, FA, RD e AD, respetivamente) foram extraídas pelo tensor de difusão ( $D$ ). No âmbito das fontes resolvidas pela CTI, a fonte de curtose excedente total ( $K_T$ ) foi obtida a partir de  $D$  e do tensor de curtose ( $W$ ), as curtoses anisotrópica e isotrópica ( $K_{aniso}$  e  $K_{iso}$ ), ditas fontes intercompartimentais, foram extraídas a partir do tensor  $D$  e do tensor de correlação do deslocamento  $Z$  (de quarta ordem na expansão cumulativa), e a fonte de curtose intracompartimental ( $K_{intra}$ ) foi extraída a partir da subtração das fontes intercompartimentais à fonte  $K_T$ . De forma a analisar os mapas obtidos para as métricas de curtose 3 h após enfarte ao nível de substância branca e cinzenta, regiões de interesse foram definidas (com base nos mapas de MD e FA) no hemisfério ipsilateral ou ipsilesional (relativo à lesão), e no hemisfério contralateral (não afetado), dos animais que sofreram o AVC. Regiões de interesse no grupo de controlo foram também definidas no hemisfério ipsilateral. Após associar os dados obtidos de cada hemisfério a diferentes subgrupos, foram realizadas comparações entre subgrupos para as diferentes métricas de curtose e uma análise ANOVA para testar diferenças significativas entre subgrupos, permitindo assim uma análise de especificidade de cada métrica aos efeitos do AVC. Foi ainda realizada uma análise da sensibilidade de cada métrica perante a lesão no hemisfério ipsilesional para todos os animais do grupo de AVC através da quantificação de voxels sensíveis à lesão em cada animal, quer ao nível da lesão total, quer ao nível das substâncias branca e cinzenta. Uma breve análise histológica foi produzida para uma comparação qualitativa com os mapas das diferentes fontes de curtose e associação com degeneração e perda celular.

Os resultados indicaram diferenças significativas ( $p < 0,05$ ) para as métricas  $K_T$  e  $K_{intra}$  entre o hemisfério ipsilateral do grupo de AVC e o hemisfério contralateral do mesmo grupo, bem como entre o hemisfério ipsilateral do grupo de AVC e o hemisfério ipsilateral do grupo de controlo (em substância cinzenta e substância branca). Porém, a métrica de  $K_{intra}$  foi a que mais se destacou, visto ter mostrado sensibilidade para o AVC na substância cinzenta perante outras métricas. Os mapas de curtose *in vivo* mostraram-se consistentes com os mapas *ex vivo*.

Em comparação com estudos anteriores, os resultados obtidos nas métricas de difusão (MD, FA, RD e AD) demonstraram congruência com a literatura, tendo os valores de  $K_T$  seguido a tendência dos valores de curtose média (MK) obtidos noutros estudos de AVC em murgancho. A menor sensibilidade para o AVC em  $K_T$ , quando comparada com  $K_{intra}$ , por exemplo, sugere que certos efeitos de curtose se poderão anular, informação essa anteriormente desconhecida. Os nossos resultados, além de favorecerem maior sensibilidade comparativamente às métricas convencionais em contexto de AVC, acentuam também a especificidade de cada fonte de curtose perante o tecido isquémico, permitindo uma possível relação com mecanismos patofisiológicos a ocorrer na fase aguda-subaguda do AVC, tais como fenómenos citotóxicos e vasogénicos. Ao resolver as fontes de curtose em tecido isquémico, foi-nos



possibilitada uma maior compreensão dos mecanismos microscópicos subjacentes, que, num formato mais sensível e específico, propicia uma caracterização de AVC inovadora e uma maior eficácia no tratamento associado.

**Palavras-chave:** Ressonância magnética por difusão, acidente vascular cerebral, AVC, modelo animal



## TABLE OF CONTENTS

---

<b>LIST OF FIGURES .....</b>	<b>XIII</b>
<b>LIST OF TABLES .....</b>	<b>XVII</b>
<b>LIST OF ACRONYMS.....</b>	<b>XIX</b>
<b>1. Introduction .....</b>	<b>1</b>
1.1 Motivation .....	1
<b>2. Background.....</b>	<b>3</b>
2.1 Stroke .....	3
2.1.1 Pathophysiology of Ischemic stroke.....	5
2.1.2 Animal Models of Brain Ischemia .....	7
2.2 Magnetic Resonance Imaging .....	10
2.2.1 Magnetic Resonance Physics .....	10
2.2.2 Signal Detection .....	13
2.2.3 Image Formation .....	15
2.2.4 Contrast Mechanisms .....	18
2.2.5 MRI Pulse Sequences.....	19
2.3 Diffusion Magnetic Resonance Imaging .....	20
2.3.1 Diffusion Principles.....	20
2.3.2 Diffusion MRI Modelling and Signal Representation in DWI.....	25
2.3.3 Double Diffusion Encoding Principles.....	27
2.4 Correlation Tensor Imaging (CTI) .....	29
2.4.1 CTI Theory .....	29
2.4.2 Correlation Tensor Imaging Extraction via Double Diffusion Encoding.....	31
2.5 Non-MR Imaging Methods for Detecting Acute Ischemic Stroke.....	32
2.6 MRI in Stroke.....	33
2.6.1 Diffusion-Weighted Imaging for Characterizing Stroke .....	34
2.7 Thesis Objectives .....	36
<b>3. Materials and Methods .....</b>	<b>37</b>
3.1. Photothrombotic Stroke Model .....	37
3.1.1. Rose Bengal Solution Preparation and Pre-surgery Protocol.....	37
3.1.2. Animal Preparation.....	37
3.1.3. Surgery and Target Area Illumination.....	39
3.1.4. Sample Preparation for <i>ex vivo</i> Experiments.....	41
3.2 Histology .....	41
3.3. dMRI Experiments .....	42
3.3.1 <i>Ex vivo</i> experiments.....	42
3.3.2 <i>In vivo experiments</i> .....	44

3.2.3 Data Analysis .....	46
<b>4. Results .....</b>	<b>49</b>
4.1. <i>Ex vivo</i> .....	49
4.1.1. Photothrombotic Stroke .....	49
4.1.2. dMRI Experiments .....	52
4.1.2 ROIs Analysis .....	60
4.1.2.a. Sensitivity Analysis .....	60
4.1.2.b. Specificity Analysis.....	61
4.2 Histological Staining .....	63
4.3. <i>In vivo</i> .....	64
<b>5. Discussion .....</b>	<b>67</b>
5.1 Technical Aspects.....	67
5.2. dMRI Findings .....	68
5.2.1. CTI .....	69
<b>6. Conclusions .....</b>	<b>71</b>
<b>7. References .....</b>	<b>73</b>
<b>8. Appendix .....</b>	<b>81</b>

## LIST OF FIGURES

---

<b>Figure 2. 1</b> – The most common sites of arterial and cardiac abnormalities provoking ischemic insult. ....	16
<b>Figure 2. 2</b> – In situ thrombotic occlusion in a patient with intracranial atherosclerosis. ....	16
<b>Figure 2. 3</b> – Putative cascade of events in focal cerebral ischemia. ....	17
<b>Figure 2. 4</b> – The main pathways implicated in ischemic cell death. ....	19
<b>Figure 2. 5</b> – (Left) The posterior part of the human circle of Willis. (Right) Extracranial arterial collateral circulation. ....	20
<b>Figure 2. 6</b> – Schematic representation of the C57BL/6J cerebral vessels. ....	22
<b>Figure 2. 7</b> – Magnetic fields lead to the alignment of nuclei with NMR required criteria. ....	24
<b>Figure 2. 8</b> – The Zeeman effect. ....	24
<b>Figure 2. 9</b> – Protons assume one of two possible states in the presence of an external magnetic field. ....	24
<b>Figure 2. 10</b> – Net magnetization in the absence and presence of an external magnetic field. ....	26
<b>Figure 2. 11</b> – (A) Rotating frame depicting net magnetization after the application of the 90° RF pulse. (B) laboratory frame with the same RF pulse application. ....	26
<b>Figure 2. 12</b> – FID following a 90° RF pulse. ....	29
<b>Figure 2. 13</b> – Necessary elements for a slice selection in a pulse sequence. ....	30
<b>Figure 2. 14</b> – Necessary pulse sequence elements for frequency and phase encoding within a slice. ....	31
<b>Figure 2. 15</b> – (Left) Pulse sequence identical to the observed in Figure 2.14. (Right) Pattern traversed by the sequence from (Left) in k-space. ....	32
<b>Figure 2. 16</b> – Selection of TR and TE values for T1 contrast (vertical orange dashed lines) and T2 contrast (vertical black dashed lines). ....	33
<b>Figure 2. 17</b> – (Left) A single-echo RF Spin Echo pulse sequence. (Right) Pulse sequence used for Gradient Echo acquisitions. ....	34
<b>Figure 2. 18</b> – (Left) An EPI pulse sequence. (Right) Its k-space trajectory. ....	35
<b>Figure 2. 19</b> – (Left) The botanist Robert Brown noticed the motion of pollen grains when suspended in water (1827). (Right) Particles have a tendency, on average, to move from high concentration regions to low concentration regions, resulting in a net flux. ....	36
<b>Figure 2. 20</b> – Gaussian displacement distribution for different diffusion coefficient values. ....	37
<b>Figure 2. 21</b> – Constant gradient field spin echo approach presented by Carr and Purcell in 1954. ....	37
<b>Figure 2. 22</b> – Spin echo sequence with proposed application of a time-dependent field gradient by Stejskal and Tanner in 1965. ....	38
<b>Figure 2. 23</b> – (A) isotropic diffusion and (B) anisotropic diffusion. ....	39
<b>Figure 2. 24</b> – Diffusion tensor ellipsoid, considering it as the envelope where a spin, which is placed at its centre, will diffuse with the same probability. ....	40
<b>Figure 2. 25</b> – DDE sequence representation within a double spin echo framework. ....	42
<b>Figure 2. 26</b> – Representation of inter-compartmental and intra-compartmental kurtosis sources. ....	44
<b>Figure 2. 27</b> – Non-contrast CT shows several early ischemic changes. ....	46
<b>Figure 2. 28</b> – In vivo MR images, photograph of brain specimen (Brain), from rat in superacute group (~ 1 hour post ischemic insult). ....	48
<b>Figure 3. 1</b> – (Left) Plastic anesthetising container above electrical heating pad. (Right) Isoflurane vaporizer with controlled gas monitoring. ....	53
<b>Figure 3. 2</b> – Stereotaxic frame set up with a (A) mouth bite bar, (B) ear bars for head fixation, (C) system of tubes for gas circulation and (D) body temperature pad. ....	53
<b>Figure 3. 3</b> – (Left) Cold light source with port adaptative to the (right) optic fibre guide. ....	54

<b>Figure 3. 4</b> – (A) and (B) Stereotaxic frame holder with (A) designed 3D printed in-house for possible and correct placing of the optic fibre guide (C). .....	54
<b>Figure 3. 5</b> – (Left) Surgical set-up before animal positioning. (A) Optic fibre light guide tip attached to stereotaxic holder for reference point and illumination step. (B) Ear bars for head fixation. (C) Bite bar attached to a nose cone for gas circulation. (D) .....	55
<b>Figure 3. 6</b> – Coronal slice from anatomical map concerning the target cortical region (S1BF, selected in blue) for focal photothrombotic induction.. .....	55
<b>Figure 3. 7</b> – Mouse brain sample from control group immersed in Fluorinert inside a 10-mm NMR tube with a stopper to prevent from floating. ....	56
<b>Figure 3. 8</b> – Study design representative scheme.....	57
<b>Figure 3. 9</b> – Acquisition parameters.....	58
<b>Figure 3. 10</b> – The 5 gradient DDE combinations (left) and respective gradient strengths combinations (right) used for the in vivo CTI protocol, acquired for 115 directions. ....	60
<b>Figure 3. 11</b> – Manually drawn masks of representative control brains.....	61
<b>Figure 3. 12</b> – Representative dataset (in vivo stroked animal) prior to PCA denoising (A) and after PCA denoising (B). ....	62
<b>Figure 3. 13</b> – T2-weighted images from a mouse from the stroke group before Gibbs ringing correction (A) and after Gibbs ringing correction (B).....	62
<b>Figure 3. 14</b> – Three representative slices from the derived mean diffusivity (MD) map of an extracted brain from the stroke group for lesion delineation. ....	63
<b>Figure 4. 1</b> – Raw T2-weighted images from all ex vivo brains 3 h post stroke onset for reproducibility analysis. 9 representative sagittal slices are presented from right to left. ....	65
<b>Figure 4. 2</b> – Raw T2-weighted images from one representative extracted brain from the stroke group. Representative coronal slices are presented from rostral to caudal direction (ex vivo). ....	66
<b>Figure 4. 3</b> – Raw T2-weighted sagittal images from one representative extracted brain from the stroked group.....	66
<b>Figure 4. 4</b> – Raw RARE images from one representative extracted brain from the stroked group. ....	67
<b>Figure 4. 5</b> – Raw T2-weighted images from one representative extracted brain from the control group. ....	67
<b>Figure 4. 6</b> – Double diffusion encoding images from a representative mouse brain over one direction. ....	68
<b>Figure 4. 7</b> – MD, FA, RD and AD maps for ex vivo acquisitions for representative stroked ex vivo brain.....	69
<b>Figure 4. 8</b> – Kurtosis sources map ( <i>parula</i> ) for 3 representative slices from a from a stroked ex vivo brain from Figure 4.7. ....	70
<b>Figure 4. 9</b> – Kurtosis sources map ( <i>parula</i> ) for 25 representative slices from a control brain, ex vivo. ....	71
<b>Figure 4. 10</b> – Kurtosis maps for 8 representative slices from the control brain sample from Figure 4.9. ....	72
<b>Figure 4. 11</b> – Kurtosis sources map ( <i>parula</i> ) for 25 slices from a stroked brain, ex vivo, . ....	73
<b>Figure 4. 12</b> – Kurtosis sources map ( <i>parula</i> ) for 25 slices from another stroked brain, ex vivo, presenting reproducibility when compared to Figure 4.11.....	74
<b>Figure 4. 13</b> – Kurtosis maps for 8 representative slices from the stroked ex vivo brain from Figure 4.11.....	75
<b>Figure 4. 14</b> – Sensitivity analysis in different metrics across different ROIs. ....	75
<b>Figure 4. 15</b> – Specificity analysis after ANOVA (multiple comparisons) across different regions of interest (ROIs). ....	76

<b>Figure 4. 16</b> – Specificity analysis after ANOVA (multiple comparisons) across different regions of interest (ROIs). .....	76
<b>Figure 4. 17</b> – Raw T2-weighted images from the acquired in vivo mouse 3 h post stroke onset. A total of 5 coronal slices were acquired and are presented from rostral to caudal direction. The red arrows point towards the lesion site. ....	77
<b>Figure 4. 18</b> – Raw T2-weighted images from the acquired in vivo mouse 3 h post stroke onset. 21 sagittal slices are presented from right to left. The red arrows point towards the lesion site.....	78
<b>Figure 4. 19</b> – Kurtosis sources map ( <i>parula</i> ) for in vivo acquisitions for control animal. $K_T$ presents higher values than any other sources. $K_{aniso}$ values reveal high intensities in white matter, whereas $K_{iso}$ shows lower intensity values for both white and gray matter. ....	80
<b>Figure 5. 1</b> – Comparison between histological H&E and Nissl staining in a representative slice from a stroked brain and its counterpart slice in the CTI maps. ....	83





## LIST OF TABLES

---

<b>Table 3.1</b> - Manually selected values for ROI thresholding of white matter (WM) and gray matter (GM) for both stroke and control groups of animals.....	59
<b>Table 4.1</b> - Photothrombotic infarct volumes from extracted ex vivo brains 3 h post ischemic onset....	63
<b>Table 4.2</b> - Voxel quantification across selected ROIs.....	72



## LIST OF ACRONYMS

---

<b>AD</b>	Axial Diffusivity
<b>ADC</b>	Apparent Diffusion Coefficient
<b>ADP</b>	Adenosine Diphosphate
<b>AMPA</b>	$\alpha$ -amino-3-hydroxy-5-methyl-4-isoxazolepropionic acid
<b>ANOVA</b>	Analysis of Variance
<b>ASL</b>	Arterial Spin Labelling
<b>ATP</b>	Adenosine Triphosphate
<b>ATP</b>	Adenosine Triphosphate
<b>BBB</b>	Blood Brain Barrier
<b>BOLD</b>	Blood-Oxygen-Level-Dependent
<b>CBF</b>	Cerebral Blood Flow
<b>CBV</b>	Cerebral Blood Volume
<b>CMR<sub>glu</sub></b>	Cerebral Metabolic Rate of Glucose
<b>CMRO<sub>2</sub></b>	Cerebral Metabolic Rate of Oxygen
<b>CSD</b>	Cortical Spreading Depolarization
<b>CT</b>	Computed Tomography
<b>CTA</b>	Computed Tomography Angiography
<b>CTI</b>	Correlation Tensor Imaging
<b>dMRI</b>	Diffusion Magnetic Resonance Imaging
<b>DC</b>	Direct Current
<b>DDE</b>	Double Diffusion Encoding
<b>DKI</b>	Diffusion Kurtosis Imaging
<b>DSC</b>	Dynamic Susceptibility Contrast
<b>DTI</b>	Diffusion Tensor Imaging
<b>DWI</b>	Diffusion-Weighted Imaging
<b>EEG</b>	Electroencephalogram
<b>EPI</b>	Echo Planar Imaging
<b>FA</b>	Fractional Anisotropy
<b>FID</b>	Free Induction Decay
<b>FMISO</b>	Fluoromisonidazole
<b>FMZ</b>	Flumazenil
<b>FOV</b>	Field of View
<b>GABAA</b>	$\gamma$ -Aminobutyric Acid Type A
<b>GE</b>	Gradient Echo
<b>GM</b>	Grey Matter
<b>HE</b>	Hematoxylin–Eosin
<b>ICA</b>	Internal Carotid Artery
<b><i>K<sub>aniso</sub></i></b>	Anisotropic Kurtosis
<b><i>K<sub>intra</sub></i></b>	Intracompartmental Kurtosis
<b><i>K<sub>iso</sub></i></b>	Isotropic Kurtosis
<b><i>K<sub>T</sub></i></b>	Total Kurtosis
<b>LAD</b>	Large Artery Disease
<b>M1</b>	Primary Motor Cortex
<b>MCA</b>	Middle Cerebral Artery
<b>MCAO</b>	Middle Cerebral Artery Occlusion

<b>MD</b>	Mean Diffusivity
<b>MK</b>	Mean Kurtosis
<b>MR</b>	Magnetic Resonance
<b>MRA</b>	Magnetic Resonance Angiography
<b>MRI</b>	Magnetic Resonance Imaging
<b>MRS</b>	Magnetic Resonance Spectroscopy
<b>MTT</b>	Mean Transit Time
<b>NMDA</b>	N-Methyl-D-aspartate
<b>NMR</b>	Nuclear Magnetic Resonance
<b>NODDI</b>	Neurite Orientation Dispersion and Density Imaging
<b>NSAID</b>	Nonsteroidal Anti-Inflammatory Drug
<b>ODF</b>	Orientation Distribution Function
<b>OEF</b>	Oxygen Extraction Fraction
<b>PCA</b>	Principal Component Analysis
<b>PET</b>	Positron Emission Tomography
<b>PFA</b>	Paraformaldehyde
<b>PGSE</b>	Pulsed Gradient Spin Echo
<b>PWI</b>	Perfusion-Weighted Imaging
<b>RARE</b>	Rapid Acquisition with Relaxation Enhancement
<b>RD</b>	Radial Diffusivity
<b>RF</b>	Radiofrequency
<b>RNS</b>	Reactive Nitrogen Species
<b>ROI</b>	Region of Interest
<b>ROS</b>	Reactive Oxygen Species
<b>SDE</b>	Single Diffusion Encoding
<b>SE</b>	Spin Echo
<b>SNR</b>	Signal-to-Noise Ratio
<b>SPECT</b>	Single-Photon Emission Computed Tomography
<b>T<sub>1</sub></b>	Longitudinal relaxation time
<b>T<sub>2</sub></b>	Transverse relaxation time
<b>T1WI</b>	T <sub>1</sub> -Weighted Imaging
<b>T2WI</b>	T <sub>2</sub> -Weighted Imaging
<b>TE</b>	Echo Time
<b>rtPA</b>	Recombinant Tissue Plasminogen Activator
<b>TR</b>	Repetition Time
<b>TV</b>	Total Local Variation
<b>WM</b>	White Matter
<b>WMTI</b>	White Matter Tract Integrity

# 1. Introduction

## 1.1 Motivation

Stroke is a dominant cause of disability and mortality in modern society, second only to coronary heart disease (Mathers et al., 2017). This imposes increasing burdens on society, healthcare systems, patients, and their families. Stroke can manifest in two main ways: haemorrhagic, if it arises from a rupture of a blood vessel; or ischemic, if triggered by an occlusion of a blood vessel (Grysiewicz et al., 2008). The latter accounts for approximately 80-85% of all cases (Prinz & Endres, 2016). The pathophysiological succession of events in stroke is relatively well characterized. On the onset of ischemia, oxygen- and energy-deprived neurons cease to function within a few seconds, and as energy-dependent cellular processes fail, structural damage ensues after only 2 minutes post-ischemia. At this stage neurons are unable to preserve their usual transmembrane ionic gradients, leading to an ion and water imbalance, resulting then in apoptotic and necrotic cell death cascades and eventually in a functional impairment which depends on the specific location of the stroke in the brain ((Hossmann, 2006; Murphy & Corbett, 2009; Murphy et al., 2008).

Hitherto the only approved therapy for acute ischemic stroke is based on the administration of recombinant tissue plasminogen activator (or intravenous alteplase), rtPA (Roth, 2011). For the activator to be administered, a time window with a maximum of ~4 hours post ischemia onset is necessary to avoid risks associated with the drug itself. Due to its narrow time window of action, only 5% of acute stroke patients are estimated to be treated with rtPA worldwide, which emphasises the importance of accurate and rapid diagnosis of acute ischemic stroke (Wu et al., 2010). Although it is known since the 1970s that Computed Tomography (CT) can rule out haemorrhagic stroke and can at times be useful for a rough evaluation of acute ischemia, CT lacks sensitivity towards stroke timing (< 50% within 6 hours post onset). Other imaging methods, such as Ultrasound Sonography, despite promising in the evaluation of cerebrovascular disease, which is the case for transcranial Doppler ultrasound (TCD), is limited when it comes to detecting occlusions with elevated efficacy only several hours post ischemia (Sarkar et al., 2007). Positron Emission Tomography (PET) plays an important role in the detection of ischemic penumbra (i.e., tissue at risk of infarction). However, not only does it require radiation exposure and time-consuming modalities but is also hampered by poor spatial and temporal resolution (Wey et al., 2014).

MRI is a non-invasive and safe imaging modality that permits longitudinal and three-dimensional assessment of tissue morphology, metabolism, physiology, and function. MRI can provide diverse sources of contrast that correspond to molecular properties such as rotational and translational dynamics of molecules as well as to influences from the microscopic environment in which these molecules resides (Callaghan, 1991). In the context of stroke, relaxation-based Magnetic Resonance Imaging (MRI) such as T1 and T2 weighted imaging (T1WI and T2WI) lack the sensitivity for ischemia (Srinivasan et al., 2006; Wey et al., 2013). However, diffusion MRI (dMRI) and perfusion MRI enable the in vivo multiparametric assessment of a wide range of pathophysiologicals, including stroke. In particular, dMRI relies on water molecules' Brownian motion to map microscopic alterations in the tissue that are evident only a few minutes after stroke onset, making dMRI one of the "gold standards" for stroke management (Baird & Warach, 1998).

Linking the underlying biological mechanisms with observed (d)MRI signals has always been very challenging due to the unspecific nature of water, on which MRI relies as an endogenous "reporter". A prominent approach for dMRI involves the so-called "signal representation approach", where the diffusion signal is expanded with a cumulant expansion. For example, Diffusion Tensor Imaging (DTI) (Basser et al., 1994) and more recently the Diffusion Kurtosis Imaging (DKI) (Jensen et al., 2005) are

examples of such signal representations, which typically provide information in well-aligned structures. However, DTI cannot account for effects such as orientation dispersion, anisotropy, non-Gaussian diffusion and polydispersity (Le Bihan & Johansen-Berg, 2012). While DKI ameliorates some issues and enables a somewhat better characterization of structures that are less coherently organized, the interpretation of DKI findings is still limited due to the low specificity of the kurtosis tensor. Indeed, kurtosis can arise from different sources that are inherently conflated in DKI; in stroke, this hampers the conclusive characterization of infarct core, penumbra and response to treatment. Another approach to analyse diffusion data involves tissue models (compartment models) that were developed to relate specific tissue features to their respective diffusion signals. Models such as Neurite Orientation Dispersion and Density Imaging (NODDI) and White Matter Tract Integrity (WMTI) – considered (Adluru et al., 2014; Fieremans et al., 2011), in the context of pathology. However, these models heavily rely on assumptions; violation thereof – which are very likely in realistic tissues – can severely compromise the accuracy, sensitivity and specificity (Henriques et al., 2019), invoking the need for more advanced model-free approaches.

Animal models have played a pivotal role in investigating tissue microstructure and dMRI in general and in disease in particular. Longitudinal investigations in these models contributed many insights into disease progression, given the heterogeneity of etiologies and the subsequent demanding effort to understand the related pathophysiology. Microscopic features in the infarct were discovered using animal models, and numerous methodologies aiming at identifying penumbra and testing neuroprotective agents were validated in experimental models of ischemia (Hossmann & Mies, 2007). In addition, the fact that the majority of advanced microstructural models are built in pre-clinical settings enables the development of important tools striving for the validation of new therapies.

The present project applies a novel dMRI approach relying on diffusion correlation tensors – Correlation Tensor Imaging (CTI) – to improve sensitivity and specificity of dMRI when probing acute microstructural alterations in a mouse stroke model. By harnessing advanced diffusion encoding sequences in high-field MRI systems, information on ischemic mechanisms so far conflated because of single diffusion encoding limitations was discovered. Microscopic fractional anisotropy ( $\mu$ FA), the diffusion tensor magnitude variance, and the intra compartmental kurtosis ( $K_{intra}$ ) (Henriques, Jespersen, & Shemesh, 2020), were all revealed using this approach. By resolving these kurtosis sources, we were able to better comprehend the microscopic mechanisms underlying stroke, which at a more specific and sensitive state bodes well for novel characterizations of stroke and treatment efficacy.

The results observed along the project showed consistency in terms of stroke model reproducibility, with well delimited infarcts, as further presented by the MRI data, but also (and most importantly) in terms of CTI estimated sources upon biological alterations at an early time point post ischemia, with reliable results across all samples. The potential of CTI in stroke imaging was evoked by performing a specificity and sensitivity analysis. Hence, important information concerning each kurtosis source effects on microscopic tissue ischemic alteration was conveyed. Reproducible and robust *ex vivo* maps were obtained, pointing towards ( $K_{intra}$ ) as the metric able to better substantiate the biological effects underlying different stages of edema. Data were validated with histology (haematoxylin-eosin (HE) and Nissl) to assess neuronal loss and damage, depicting possible relationships between tissue properties and the obtained contrasts, at a preliminary histological point of view. *In vivo* data were consistent with the *ex vivo* maps, which allowed to confirm that our findings were not biased by *ex vivo* conditions.

## 2. Background

This chapter exposes two main topics. The first presents stroke in a more comprehensive perspective, focusing then on ischemic infarcts and their pathological cascade, as well as state-of-the-art imaging techniques aiming at acute detection. The second topic covers fundamental concepts on Magnetic Resonance (MR), introduces the theory behind diffusion MRI as the gold standard technique towards early stroke detection, and its role in assessing information on microstructural ischemic tissue properties at early stages post infarct.

### 2.1 Stroke

Stroke is the second most lethal cause of death worldwide, as well as a widespread source of adult disability in developed countries, therefore forming a burden for patients and families which has been projected to rise to 61 million disability-adjusted life years by 2020 (Norrving, 2014). It corresponds to the neurological manifestation of a significant decrease in cerebral blood flow caused by a disruption of blood supply in a circumscribed brain region, which leads to a focal neurologic deficit rapidly developing, and can either be ischemic or haemorrhagic. The former, which accounts for approximately 80-85 % of all cases, is triggered by an occlusion of a blood vessel, whereas the latter one is based on a rupture of a blood vessel (Grysiewicz et al., 2008; Hossmann, 2006).

Ischemic stroke is based on two important regions, the ischemic core and penumbra. The core is usually defined as the irreversibly injured part following cell death, whereas the ischemic penumbra is characterized as being “tissue at risk”, i.e., the perilesional zone which is functionally compromised yet still preserves its structural integrity, having constrained blood supply but maintained energy metabolism (Dirnagl & Walz, 2016). Basically, while absolute blood flow in the core is diminished to a range  $< 1$  ml/g/min, regional blood flow in the penumbral region remains at 2-4 ml/g/min (Ebinger et al., 2009). It is crucial to consider both terms separately, especially when it comes to widening the tissue salvaging time window.

As for the different ischemic infarct subtypes, these can be classified according to where the blood clot is developed, relatively to the obstruction site: embolism – if it arises from another location in the circulatory system, commonly the heart (hence the term “cardiac embolism” – Figure 2.1 – is commonly addressed, with regard to embolisms which are, on their majority, originated by atrial fibrillation, i.e. an irregular heart rate) or large arteries of the upper neck and chest; thrombotic occlusion – if it arises within the constricted vessel (*in situ*), usually due to excessive thrombus formation in areas of atherosclerotic plaque, sometimes provoking total occlusion of the vessel (Amarenco et al., 2009; Donnan et al., 2009). The latter might occur as a result of branch occlusion (an important cause of lacunar infarcts), hypoperfusion (prone to watershed stroke) or large artery disease (LAD), which is the major cause of cerebral infarction in developed countries, known to have its main pathology based on thrombosis superimposed on atherosclerosis. However, besides thrombotic occlusion *in situ* (Figure 2.2), LAD is also a potential precursor to artery-to-artery embolism since certain characteristics of atherosclerotic plaques have been proved to generate embolisms. In this profile, the embolism derives from intraplaque inflammation and subsequent cytokine activation, leading to ulceration and intraplaque haemorrhage. This procoagulation environment is prone to thrombi formation, likely to be broken up by forceful blood flow and migrate to a further vessel (Norrving, 2014).

Numerous stroke risk factors have been recognized by epidemiologic studies, whether they are modifiable or not. Some not modifiable factors include age (ischemic infarct risk raises with age due to atherosclerosis rates also increasing), race (blacks are more prone to ischemic insult than Hispanics and whites), sex (generally more prevalent in men) and family history. Causes involving lifestyle and

environment are typically considered as modifiable and hypertension, diabetes, smoking and atrial fibrillation are well-established factors included in this group (Grysiewicz et al., 2008).

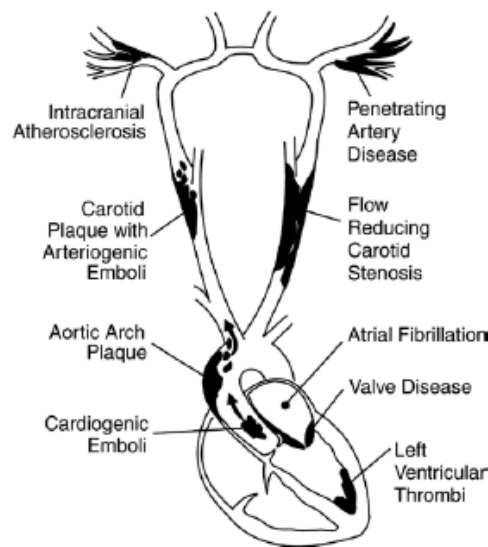


**Figure 2.1** – The most common sites of arterial and cardiac abnormalities provoking ischemic insult. Adapted from (Albers et al. 2004).

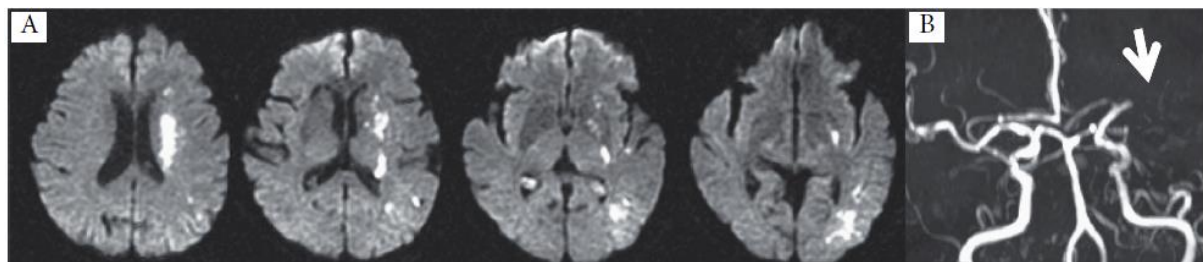


**Figure 2.2** – in situ thrombotic occlusion in a patient with intracranial atherosclerosis. (A) DWI showed acute infarcts in the left lenticulocapsular and neighbouring areas between middle cerebral artery (MCA) and posterior cerebral artery. (B) Magnetic Resonance Angiography (MRA) presented thrombotic occlusion of the left MCA. Adapted from (Norrving, 2014) .

Several non-invasive imaging techniques have confirmed that brain infarcts tend to grow (Hoehn-Berlage et al., 1995) and that this growth can be differentiated into three important phases: acute, subacute and chronic phase. When the acute phase first takes place, tissue injury (established after a few minutes post ischemia onset) is the direct result of the induced energy failure as well as the subsequent terminal cell membranes depolarisation due to ischemia, leading to so-called cytotoxic edema. During the following subacute phase, the core tends to enlarge into the peri-infarct penumbra until both match, after 4-6 h, during which molecular cell injury occurs. The chronic phase of injury has vasogenic edema as its main phenomena simultaneous with inflammation and likely cell death, and can last from days to weeks, still contributing to injury development (Hossmann, 2006). In addition to the spatiotemporal pattern of the lesion which is evolving, there are alterations which resemble longitudinal neuronal plasticity. It is still not fully known how these processes are reflected in the functional outcome (e.g., in the recovery or loss of functionality in affected organs downstream of the area affected by the lesion).



### 2.1.1 Pathophysiology of ischemic stroke

Since stroke is a heterogeneous disorder associated with numerous pathogenic mechanisms, it is crucial to understand the factors underlying the disease to determine appropriate treatment and prevention strategies in different patients. Ischemic infarct generates a cascade of processes resulting in cell death (ionic imbalance and excitotoxicity, oxidative/nitrosative stress, inflammation, apoptosis and peri-infarct depolarization), which evolve in both temporal and complex occurrences (Figure 2.3) starting from the onset of the infarct (after blood flow and energy supply are compromised in the brain) and lasting up to days in a chronic phase (González et al., 2011). These ischemic cell death mechanisms intervene with injury within neurons, glia, and vascular elements, and will be described in detail below. Nonetheless, it is important to keep in mind that molecular injury differs according to whether ischemia assumes a transient focal or permanent ischemia profile (Hossmann, 2006; Xing et al., 2012).

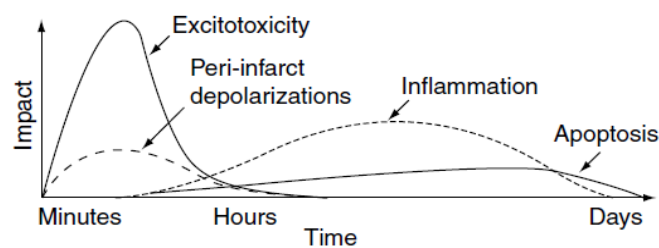


**Figure 2.3**– Putative cascade of events in focal cerebral ischemia. The x-axis illustrates the cascade development chronologically, whereas the y-axis reflects the impact of each element on the final outcome (Dirnagl et al. 1999).

The first event in the cascade involves energetic considerations. In the area suffering from blood supply, adenosine triphosphate (ATP) synthesis becomes hampered and deficient. However, ATP consumption continues due to the high energy demands of brain tissue. The loss of neuronal ionic homeostasis provokes a dramatic decline in total ATP levels, and lactate acidosis develops. At the same time, neurotransmitter releases occur, hence inhibition of reuptake also follows. Specifically, glutamate, the main excitotoxic neurotransmitter, binds to ionotropic N-Methyl-D-aspartate (NMDA) and  $\alpha$ -amino-3-hydroxy-5-methyl-4-isoxazolepropionic acid (AMPA) receptors (iGluRs), promoting calcium overloading influx. For this reason, phospholipases and proteases are triggered, which in turn degrade essential membranes and proteins. In parallel, the glutamate receptors stimulate an excessive influx of sodium and water, leading to cell swelling, edema and extracellular space shrinkage, collectively referred to as cytotoxic edema (Hossmann, 2006).

High calcium, sodium, and adenosine diphosphate (ADP) levels in ischemic cells stimulate excessive mitochondrial dysfunction and generation of reactive oxygen species (ROS) and reactive nitrogen species (RNS), directly damaging lipids, proteins, nucleic acid, and carbohydrates (Figure 2.4) (González et al., 2011; Xing et al., 2012). All these damaging factors will eventually result in neuronal death comprising necrosis, apoptosis, and autophagy.

Simultaneous with the above-mentioned events, cortical spreading depolarization (CSD) also occurs post-ischemia, intervening when potassium concentrations exceed a critical threshold, and is characterized by an intense depolarization of membranes (neuronal and glial) slowly propagating. Thus, a near-complete cell membrane depolarization and temporary neuronal activity depression occur due to an ionic imbalance resulting from the sodium and calcium pumps dysfunction (Kao et al., 2014).

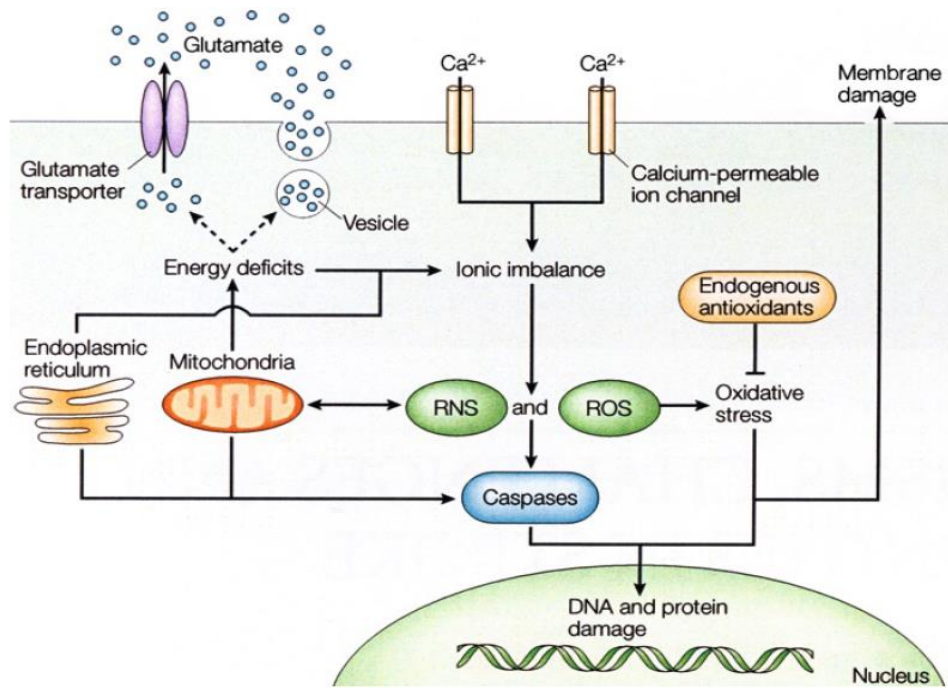


**Figure 2.4** – The main pathways implicated in ischemic cell death: excitotoxicity, ionic imbalance, oxidative and mitrostatic stresses, and apoptotic-like mechanisms. After ischemic onset, loss of energy substrates leads to mitochondrial dysfunction and generation of reactive oxygen species (ROS) and reactive nitrogen species (RNS). Additionally, energy deficits lead to ionic imbalance, and excitotoxic glutamate efflux and build-up of intracellular calcium. Downstream pathways ultimately include direct free radical damage to membrane lipids, cellular proteins, and DNA, as well as calcium-activated proteases, plus caspase cascades that dismantle a wide range of homeostatic, reparative, and cytoskeletal proteins. Adapted from (Dalkara et al. 2003).

Within the core, excitotoxic and necrotic cell death occurs within minutes, and the tissue undergoes irreversible damage in the absence of prompt and adequate reperfusion. Despite this, cells in the neighbouring areas are supported by collateral circulation and their fate is dependent on numerous factors, such as the degree of ischemia and the timing of reperfusion. There are two major collateral systems to consider: the circle of Willis and Heubner's leptomeningeal anastomoses. Both are responsible for interconnecting the main supplying arteries of the brain, i.e., the right and left posterior, middle and anterior cerebral arteries. The former is in charge of the blood supply redistribution under conditions of vascular occlusion of the carotid or vertebral arteries, and in case flow resistance increases in these vessels, blood perfusion pressure declines throughout this collateral system (Figure 2.5) (Hossmann, 2006).

After exhaustion in the blood perfusion system, the most peripheral branches of the brain arteries are the first to suffer a blood flow decrease. The pial network in Heubner's anastomoses system (Figure 2.5) determines the severity and volume of the induced ischemic infarct according to the distance from the occlusion of the brain artery to its origin from the circle of Willis (Liebeskind, 2003). Both the number and diameter of the anastomoses differ from patient to patient, being proportional to collateral supply efficacy from the adjacent non-constricted vascular regions. Here, a rise in perfusion pressure is observed in peripheral branches of the arteries, in contrast to the circle of Willis, hence preferentially protecting the surrounding areas. Given the elevated variability across individuals, there is a broad range of infarct volumes. In terms of microcirculation, in focal ischemia it is progressively affected because of different mechanisms: by an increase in viscosity in the blood, by the adhesion of leukocytes to the wall of the vessel, and by the capillaries compression (due to astroglia swelling) (Hossmann, 2006). In the peripheral region supported by this collateral circulation, i.e., ischemic penumbra, cell death occurs relatively slowly via the active cell-death mechanisms mentioned above.

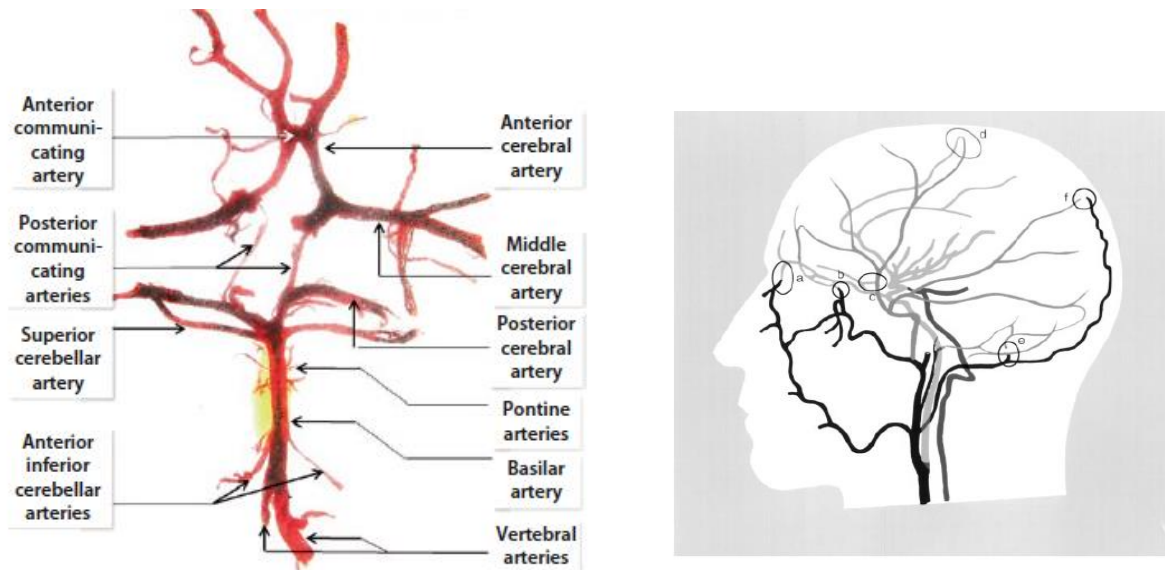


**Figure 2.5** – (Left) The posterior part of the human circle of Willis. Adapted from (Schröder, Moser, & Huggenberger, 2020) (Right) Extracranial arterial collateral circulation. Anastomoses from the facial (a), maxillary (b), and middle meningeal (c) arteries to the ophthalmic artery and dural arteriolar anastomoses from the middle meningeal artery (d) and occipital artery through the mastoid foramen (e) and parietal foramen (f) are shown. Adapted from (Norrving, 2014; Liebeskind, 2003).

## 2.1.2 Animal Models of Brain Ischemia

Experimental animal models are crucial to comprehend the mechanisms underlying cerebral ischemic events, the subsequent mechanisms of neuronal survival, as well as to promote new therapeutic interventions.

There are two important models of ischemic stroke – global and focal – each accounting for different mechanisms. The former is developed upon transient circulatory arrest, in which there is a total loss of cerebral blood flow (CBF) within seconds, with electroencephalogram (EEG) activity ceasing in less than a minute (Dirnagl & Walz, 2016). The focal ischemia model, on the other hand, involves a permanent or transient CBF reduction in the region of a cerebral artery and its branches. It can be induced either using a thrombotic or embolic occlusion of an artery, specially the middle cerebral artery (MCA) (Bogousslavsky et al., 1988). Since human ischemic stroke usually results from MCA occlusion (MCAO), models based on this artery occluding approach resemble the clinical picture the most (Longa, Weinstein, Carlson, & Cummins, 1989; Mhairi, 1992). The intra-luminal suture model (used in a considerable number of neuroprotection experiments), for instance, is based on the insertion of a surgical filament via the internal carotid artery (ICA) to reach and occlude the MCA (Chiang et al., 2011; Howells et al., 2010). Although it enables reproducible lesions, is well established in rats and mice, allows for transient – reflecting human stroke with therapy-induced or spontaneous reperfusion – and permanent – mimicking human stroke without reperfusion – ischemia, it has high mortality rates when severe ischemia is provoked.

Thromboembolic models are also widely used in rats and mice and are advantageous due to how closely they may represent the human ischemic stroke pathophysiology, proving to be suitable for studying thrombolytic agents, the effect of thrombolysis and combined strategies, and the reperfusion injury mechanism (Dirnagl & Walz, 2016). Nonetheless, it presents high variability in lesion size and spontaneous recanalization, unless it is *in situ*. If that is the case, although well localized, it still requires craniectomy.

The endothelin-1 model is another focal ischemia model candidate, based on the direct application of endothelin-1 (a potent vasoconstrictor) on the exposed MCA or cortex, and hence requiring craniectomy (I. M. Macrae, Robinson, Graham, Reid, & McCulloch, 1993; Sharkey, 1993). Despite this disadvantage, it facilitates anatomical targeting of the lesion (Howells et al., 2010). A group of cerebral artery occlusion through electrocoagulation or mechanical methods contemplating techniques which require open surgical access have also been broadly used, such as the electrocoagulation-surgical model described by Tamura and colleagues in 1980 (I. Macrae, 2011; Tamura, Graham, McCulloch, & Teasdale, 1981), or methods predicated by the use of an adjustable surgical ligature or micro-aneurysm clips (Shigeno, Teasdale, McCulloch, & Graham, 1985; van Bruggen et al., 1999). These models produce to great reliability and low mortality, but a high level of expertise or mastery is necessary. A more recent transient model is the distal middle cerebral artery occlusion (dMCAo), which consists of a compression in the distal portion of the MCA for 60 minutes via a blunted needle. This process is followed by 24 h of reperfusion (Morancho et al., 2012). Although it involves skull and primary motor cortex (M1) portion exposition, it is considered to be a less invasive method than the intra-luminal filament technique (Canazza et al., 2014).

Finally, photochemical models have been broadly used to mimic the ischemic clot formation. The photothrombotic Rose Bengal stroke model, first proposed by Rosenblum and El-Sabban in 1977 (Rosenblum & El-Sabban, 1977) and later improved by Watson and colleagues in 1985 (Watson et al., 1985) allows the induction of a focal ischemia through photo-activation of the Rose Bengal dye. Immediately after illumination the dye is activated and singlet oxygen is produced, culminating in endothelial damages, platelet aggregation and thrombi formation – determining the stoppage of local blood flow. Without requiring craniectomy, this model enables a non-invasive induction of a focal ischemic stroke with elevated reproducibility and survival rate (>98%) (Porritt et al., 2012).

Several models of focal ischemia have been used to mimic distinct human stroke conditions, considering that stroke in humans is heterogeneous and depends on the site of ischemia, its severity, duration and associated comorbidities. Hence, it is quite impossible to obtain an animal model which mimics all human aspects of stroke. Aspects such as mortality rate, the need or not for craniectomy, the involving variability in lesion size, the degree of similarity with lesion development and reproducibility should be considered.

For this project I opted to reproduce a photothrombotic stroke approach in a mouse model (Watson et al., 1985) since it does not require craniectomy, enables the selection of a well-defined infarcted area and its technical variations are well known to allow for the induction of subcortical stroke and stroke with a penumbra (Dirnagl & Walz, 2016). In addition, this model is known to have a high level of reproducibility (Labat-gest & Tomasi, 2013). Although the photochemical model can encounter several pitfalls, such as the early breakdown of the blood-brain barrier due to the photooxidative damage of endothelial cells, it is still considered an excellent model for stroke and penumbra.

When approaching animal models in stroke, one should keep in mind the differences between humans and, in this case, rodents. Starting by considering the differences in anatomy and physiology, both rats and mice have considerably less white matter than humans and present lissencephaly (i.e., their gray matter is not gyrated). CBF values in mice are approximately twice to three times more elevated when compared to humans and the circle of Willis in rodents can sometimes be incomplete or have some anomalies. The circle of Willis corresponding arteries in mice are presented in Figure 2.6. Although resembling at first sight the human circle, important differences such as the fact that posterior cerebral artery does not originate from the basilar artery in mice, as it does in humans. Furthermore, there is lack of olfactory arteries in humans (they suppress postnatally) and the mouse internal carotid artery lacks a siphon (Schröder et al., 2020). Since animals rarely develop occlusion of cerebral arteries in a spontaneous way, experimental occlusion is required to mimic branches occlusions of the circle.

Additionally, rodents present a poor collateral which is likely to have an influence on the severity of ischemic lesion outcome (Hermann & Doeppner, 2016).

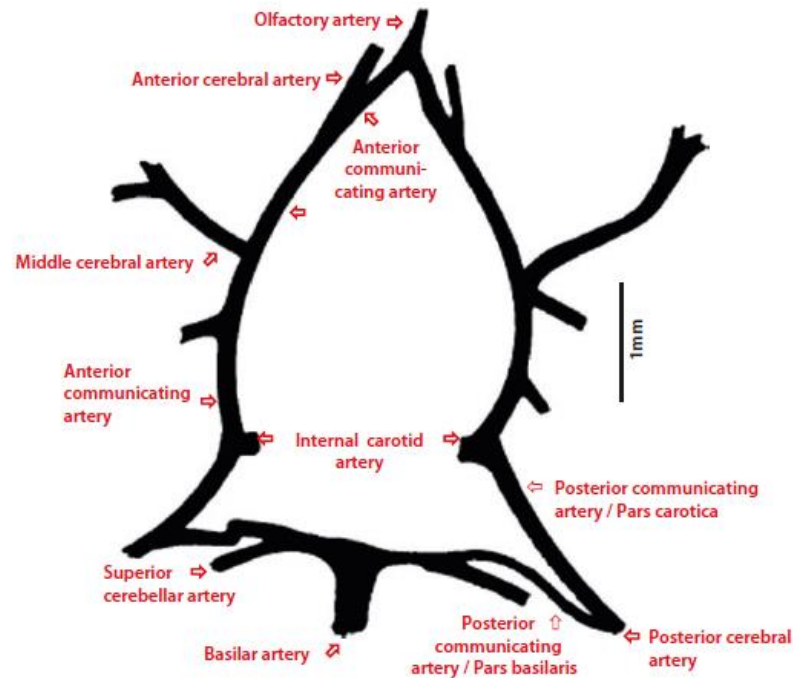


**Figure 2.6** – Schematic representation of the C57BL/6 cerebral vessels. Extracted from (Schröder et al., 2020)

Nevertheless, a rather crucial difference between animal models and human stroke is related to the different penumbral thresholds which subsequently lead to varying rates when it comes to infarct evolution. In rodents, the tissue at risk (penumbra) 2 hours post stroke encounters CBF from 20 to 40% of control values, whereas in humans, the penumbral area at 6 hours has a CBF from 10 to 30% of control. From a broader point of view, the stroke evolution occurs from 2 to 4 hours in rodents and up to 48 hours in humans (although variable) (Ginsberg, 2003; Heiss et al., 2001). Despite these points, the similarity in fundamental biological processes (cell death and survival) between humans and rodents is irrefutable, corroborated by the resemblance observed when it comes to molecular processes underlying ischemic death (Danial & Korsmeyer, 2004). However, it should be mentioned that rodents, particularly mice, are attractive for research due to their genetic homogeneity and because their molecular biology is rather well understood. Moreover, transgenic technologies can be applied easily in mice and rodent stroke models have been found very useful in reconstructing crucial steps of neural death and cell repair.

## 2.2 Magnetic Resonance Imaging

Magnetic resonance imaging (MRI) is a non-invasive imaging technique which generates three dimensional images through the measurement of magnetic moments of nuclear spins. MRI is able to accomplish high spatial and temporal resolutions and, due to its excellent safety profile, it offers the ability to execute longitudinal studies without risks associated with the imaging technique itself. Therefore, MRI is a versatile and powerful tool for research in general and pathology in particular. This section will provide an overview of MR physics, signal generation and acquisition, image encoding and reconstruction, and contrast generation in MRI images.

### 2.2.1 Magnetic Resonance Physics

#### 2.2.1.a. Nuclear Spins

Nuclear Magnetic Resonance (NMR), previously known as Nuclear Induction by Bloch (Bloch, 1946), is the spectral precursor of MRI, and serves as the basis for all MRI physics. It is based on complex interactions between nonzero nuclear spins and magnetic fields, which give rise to the complex phenomena collectively termed “NMR”. Nonzero spin nuclei carry a magnetic moment ( $\mu$ ) and an associated angular momentum ( $J$ ). Analogous to a magnet bar spinning, protons experience a gyroscopic motion, i.e., precession the changing magnetic field creates a magnetic moment  $\mu$ , the moving mass generates  $J$ . In order to present the vectors defining the current flow and rotation to have the same direction, a scalar factor between  $\mu$  and  $J$  was assumed and is presented in equation 2.1.

$$\mu = \gamma J \quad (2.1)$$

where  $\gamma$  is the gyromagnetic ratio – a unique quantity for a given nucleus describing the rate of precession per magnetic field unit. The sum of all magnetic moments from spins of different orientations generates a net magnetization of a spin system,  $M$  – a vector whose orientation is along the longitudinal direction and whose magnitude is proportional to the difference between the number of spins in both parallel and antiparallel states (Figure 2.7), described below (Huettel et al., 2014).

#### 2.2.1.b. Spins in an External Magnetic Field

In the presence of an external main magnetic field,  $B_0$ , nuclear spins align parallel and anti-parallel with the field’s main direction, with the associated energy levels split into two different energy states, with each state’s energy level  $E$  defined by:

$$E = -\mu \cdot B_0 \quad (2.2)$$

This splitting is described by the Zeeman effect (Figure 2.8). The interaction is characterized by a precession motion, with the aligned spins rotating around the field’s main direction in a gyroscopic motion (Figure 2.9) (Huettel et al., 2014). The differences between the populations of spins in the different energy levels is very small, in the parts per million range, but this can be sufficient to generate an interaction in the energy equivalent to the difference between states; if such energy is provided to the system, the spins can absorb or emit energy in the form of an electromagnetic radiation.



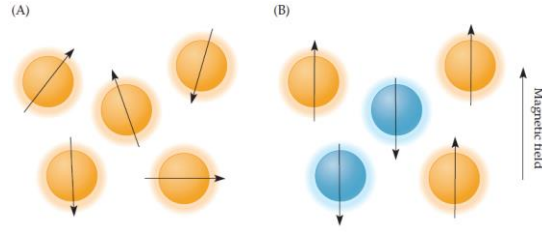


**Figure 2.7** – Magnetic fields lead to the alignment of nuclei with NMR required criteria. (A) Without an external magnetic field, protons in free environment will have their spin axes randomly aligned. (B) After an external magnetic field is induced, each proton's axis of spin will either align parallelly or antiparallelly to the magnetic field. More of the spins will assume the parallel state, leading to a parallel net magnetization relative to the scanner's magnetic field. Extracted from (Huettel et al., 2014).

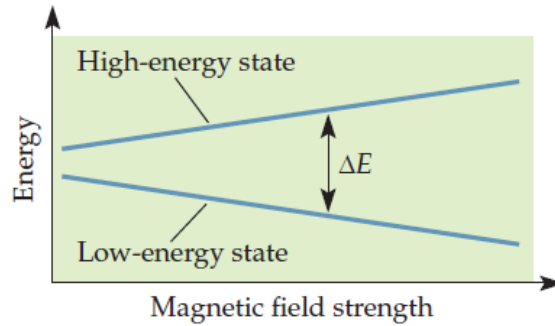


**Figure 2.8** – The Zeeman effect. The energy difference ( $\Delta E$ ) between the two different energy states increases according to the strength of the magnetic field. Spins are more likely to remain in the lower energy states as the energy difference rises. Extracted from (Huettel et al., 2014).

The frequency  $\omega_0$  at which the spins precess around  $B_0$ , also known as the Larmor frequency, is defined as  $\omega_0 = \gamma B_0$ . Since the spins are rotating, a resonance condition must be satisfied for energy to be absorbed by the system. If an applied  $B_1$  field is applied with the correct frequency matching the Larmor frequency, in a plane perpendicular to the main axis of the field:

$$\omega_1 = \gamma B_1 \quad (2.3)$$

where  $B_1$  is the magnetic field intensity and  $\gamma$  is the gyromagnetic ratio constant.

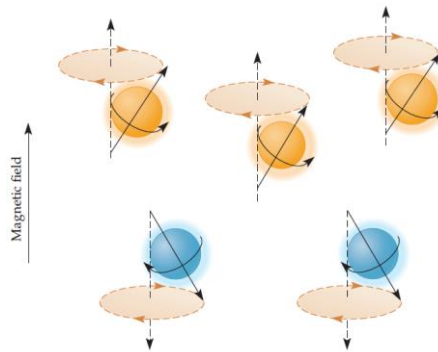


**Figure 1.9** – Protons assume one of two possible states in the presence of an external magnetic field: the parallel, lower energy state (in orange) and the antiparallel, higher energy state (in blue). Extracted from (Huettel et al., 2014).

### 2.2.1.c. Spin System Excitation and Relaxation

MRI takes advantage of electromagnetic radiofrequency (RF) energy proton absorption due to the fact that the hydrogen Larmor frequency belongs to the range of RF in NMR. Considering a net magnetization from the sum of all magnetic moments in the system in the presence of a  $B_0$  field aligned with the z-axis, its longitudinal component will be evident whereas its transverse magnetization will be null at this point (along the xy plane), as it is possible to be observed in Figure 2.10.

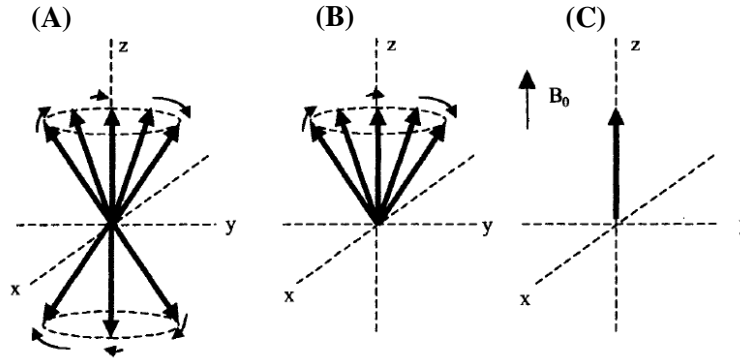


**Figure 2.10** – Net magnetization in the absence and presence of an external magnetic field. (A) Representation of individual magnetic moments from a spin system, precessing around the longitudinal axis, in which there are more protons aligned with the field than against it. (B) The excess number of protons on the parallel state cancels the effect of the number of protons on the antiparallel state. (C) The net magnetization  $M$  has only a longitudinal component ( $M_{xy} = 0$ ). Extracted from (Webb, 2003)

Once the RF pulse is applied (also referred to as  $B_1$  field) by a transmit coil, energy is absorbed by the protons with aligned spins, and if the waves are delivered continuously at the Larmor frequency, there will be a point in which the number of spins in each state will be equal and there is no net magnetization  $M$  along the longitudinal direction because it has been fully transferred into the transverse plane, described by a movement known as nutation. To ease the visualization of this phenomenon, it is possible to adopt a rotating frame of reference as shown in Figure 2.11. In this rotating frame, the z-axis maintains its orientation when compared to the laboratory frame, but  $x'$  and  $y'$  are now the laboratory frame  $x$  and  $y$ , except for the fact they rotate at the Larmor frequency. The amplitude of  $M$  depends on the coherence between those spins and culminates when they precess with the same frequency and at the same phase.

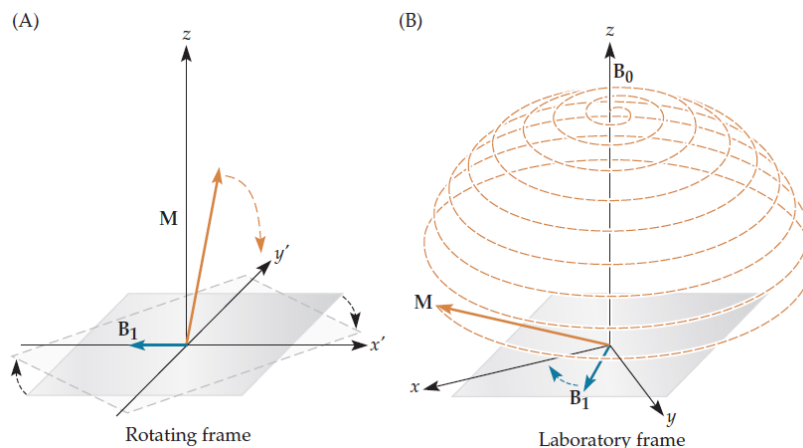


**Figure 2.11** – (A) Rotating frame depicting net magnetization after the application of the  $90^\circ$  RF pulse. (B) Laboratory frame with the same RF pulse application. Extracted from (Huettel et al., 2014).



After the net magnetization is tipped into the transverse plane by the ideal 90° RF pulse, over time the spin-spin interactions (intrinsic source) provoke a loss of coherence between the spins, leading to an exponential decay characterized by a transverse relaxation constant  $T_2$  which defines the net magnetization component  $M_{xy}$  in equation 2.4. In addition, spatial variations in the field strength (extrinsic source) result in spatial differences in precession frequencies, thus leading to incoherence within spins. The compilation of both intrinsic and extrinsic sources results in a signal loss referred to as  $T_2^*$ , corresponding to a relaxation constant always shorter than  $T_2$ .

When there is a loss of energy in the spin system, right after excitation, the emitted energy is detected by the receiver coils, causing a longitudinal recovery up to approximately two thirds of its value before the pulse was applied, characterized by the longitudinal relaxation constant  $T_1$ . In this relaxation there is spin lattice interaction reflected by the high-energy state spins returning to their original low-energy state, with net magnetization assuming its initial direction, parallel to the  $B_0$  field (Webb, 2003), (Huettel et al., 2014). The longitudinal net magnetization  $M_z$  can be described in equation 2.5, which in addition to  $M_{xy}$  lead to important terms in the Bloch equation (equation 2.6), describing the behaviour of the net magnetization within a spin system when there is a varying magnetic field (Bloch, 1946).

$$\vec{M}_{xy} = \vec{M}_0 e^{-\frac{t}{T_2}} \quad (2.4)$$

$$\vec{M}_z = \vec{M}_0 (1 - e^{-\frac{t}{T_1}}) \quad (2.5)$$

$M_0$  corresponds to the initial net magnetization.

$$\frac{d\vec{M}}{dt} = \gamma \vec{M} \times B + \frac{1}{T_1} (\vec{M}_0 - \vec{M}_z) - \frac{1}{T_2} (\vec{M}_x + \vec{M}_y) \quad (2.6)$$

The above equation describes the MR phenomena, in which the net magnetization vector of a spin system,  $M$ , precesses around the main magnetic field axis at the Larmor frequency, with its change in the longitudinal direction regulated by  $T_1$  and its variation in the transverse plane regulated by  $T_2$ .  $B$  corresponds to the total magnetic field experienced by the system, assuming that it is the sum of two magnetic fields, the excitation pulse  $B_1$  and the static magnetic field  $B_0$ .

## 2.2.2 Signal Detection

The nuclear spins excitation by a RF pulse can be understood in terms of transitions between energy levels, as explained previously in subchapter 2.2.1.b. By considering that there is a coil placed around the sample with its symmetry axis transverse to the field  $B_0$  and that in the laboratory frame any transverse magnetization (that is precessing at the Larmor frequency) will induce an oscillatory electromotive force (emf) at frequency  $\omega_0$ , a quantitative analysis of the signal amplitude can be performed. This amplitude is proportional to the transverse magnetization and the detection process is regulated by Faraday's law, which in turn is dependent on the magnetization vector. Hence, only transverse magnetization will induce signal, enhancing its importance. The RF receivers work based on an inherently phase sensitive process known as heterodyning, i.e., mixing the signal emf with a reference RF oscillator output. Direct current (DC) quadrature output signals are obtained where the mixing reference is oscillating at the Larmor frequency. If we consider any other reference mixing frequency  $\omega_r$ , the signal will be oscillating at the offset frequency  $\Delta \omega = \omega_0 - \omega_r$  (Callaghan, 1991).

The detection process mathematics are described using complex numbers in which the real part and the imaginary part represent the  $x$ -direction and the  $y$ -direction in the rotating frame, respectively. In cartesian notation, the laboratory frame magnetization at time  $t$  after the pulse is:

$$M(t) = [M_0 \cos\omega_0 t \mathbf{i} + M_0 \sin\omega_0 t \mathbf{j}] \times e^{-\frac{t}{T_2}} \quad (2.7)$$

Hence, the heterodyne signal at offset frequency, in complex number notation, by contrast, is:

$$S(t) = S_0 e^{i\phi} \times e^{i\Delta\omega t} \times e^{-\frac{t}{T_2}} \quad (2.8)$$

where  $\phi$  corresponds to the absolute receiver phase and  $S_0$  describes the signal amplitude promptly following the pulse.

The NMR signal is measured as an oscillating and decaying emf induced by the magnetization in free precession (in the time domain) known as Free Induction Decay (FID). FID is then Fourier transformed to be represented in the frequency domain, as shown in Figure 2.12 (for the case where  $\phi = 0$ )

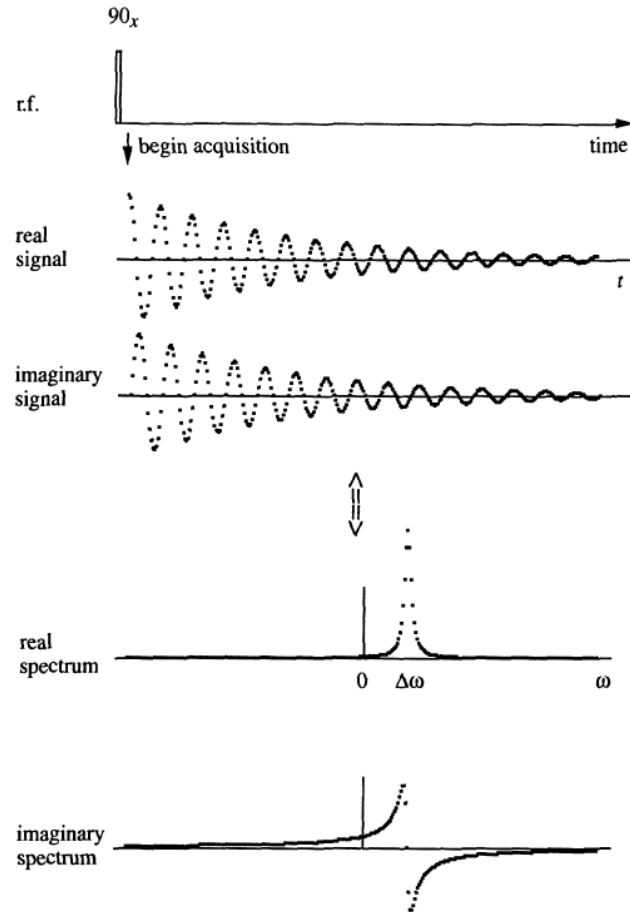


**Figure 2.12** – FID following a  $90^\circ$  RF pulse. Both the real and imaginary signal parts correspond to the in-phase and quadrature receiver outputs. Here, the signal is depicted with a null receiver phase, and on a complex Fourier transformation, it provides real absorption and imaginary dispersion spectra at the offset frequency. Extracted from (Callaghan, 1991).

This spectrum provides information about the different chemical shifts in the system, but it does not allow to discern spatial properties in the sample; in other words, it is not possible to discriminate signal from differently located protons.

### 2.2.3 Image Formation

In 1973, Lauterbur realized that, by applying a continuous magnetic field gradient using specialized coils, spins at distinct locations would precess at different frequencies. The use of such gradient coils enabled the separation of the signal frequencies into spatially-dependent components thus delivering information about the nuclei spatial distribution (Lauterbur, 1973). This Nobel prize winning discovery allowed us to trade off NMR's spectral dimension by spatial dimensions.

#### 2.2.3.a. Slice Selection

In slice-selective (or 2-dimensional) MRI, every single slice is excited separately via the application of a slice-selective RF pulse, which is applied during the application of a gradient – normally assumed to be along the z-axis. The aim is for the pulse to tip the spins' magnetization in that slice only, affecting the protons precessing within the desired frequency band. For that, the static z-axis gradient, when introduced, allows us to tune the Larmor frequencies of all spins exclusive to the slice to match the excitation pulse frequency. In order to excite a rectangular slice along the z direction, one should opt for a sinc-modulated pulse since its Fourier transform is a rectangular function – hence, a rectangular frequency response, as intended. The slice thickness  $T$  depends both on the frequency bandwidth  $\Delta\omega_s$  of the pulse and the slice selecting gradient strength, described by:

$$T = \frac{\Delta\omega_s}{\gamma G_z} \quad (2.9)$$

where  $\gamma$  is the gyromagnetic ratio of the nucleus and  $G_z$  is the strength of the gradient field (Webb, 2003).

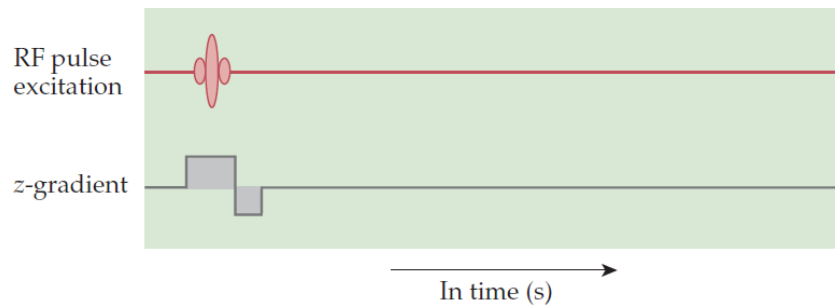


**Figure 2.13** – Necessary elements for a slice selection in a pulse sequence. A rephasing z-gradient (by convention) is applied to counteract the effects due to dephasing subsequent to the positive gradient influence (phase coherence is lost). Extracted from (Huettel et al., 2014).

As presented in Figure 2.13, a rephasing z-gradient is applied in order to counteract the effects because of dephasing due to the positive gradient influence. This opposite polarity gradient responds to the loss of phase (i.e., accumulated change in angle as the result of rotation over time) coherence.

#### 2.2.3.b. Phase and Frequency Encoding

When the slice is selected, it is important to mention that all excited spins provide equal contribution at this stage to the MR signal generation, i.e., spatial information within the slice has not yet been encoded. At this point, all signals along the z direction are integrated, and the missing two dimensions need to be encoded by two different encoding schemes. The first one is Phase Encoding and corresponds to a sequential application of another gradient at a distinct spatial axis (conventionally

labelled as  $G_y$ ) for a given time period, with the role of pre-setting the spins phases in a controlled manner along the y-axis, prior to the second encoding scheme – Frequency Encoding. This last scheme, on the other hand, corresponds to an application of a gradient in a different direction from the previous one (conventionally labelled as  $G_x$ ) in order to generate a spatially dependent frequency while signal is being acquired (Huettel et al., 2014). Basically, the phase encoding gradient is turned on and off prior to data acquisition, whereas the frequency encoding gradient is turned on during acquisition, as shown in Figure 2.14. Given the fact that the phase-encoding process must be repeated  $N_p$  times (in order for a different phase encoding to be acquired each time) and that  $N_r$  data points are acquired during the readout, it is possible to say that the resulting dataset has the two-dimensional size of  $N_p \times N_r$  (Bernstein, King, & Xiaohong, 2004).

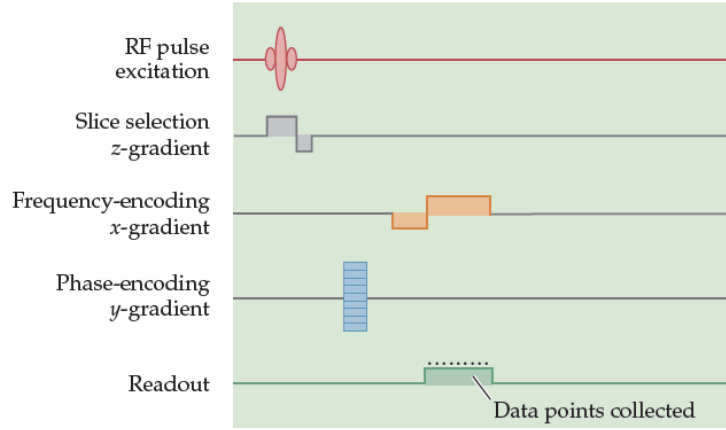


**Figure 2.14** – Necessary pulse sequence elements for frequency and phase encoding within a slice. The phase-encoding gradient is commonly applied before the frequency-encoding gradient in order for spins phase differences to accumulate along that direction (though it is possible for the encoding gradients to be acquired simultaneously). Extracted from (Huettel et al., 2014).

After slice selection, considering it leaves two dimensions to be Fourier encoded, the MR signal  $S(t)$  equation can be described as:

$$S(t) = \iint_{xy} M_{xy} e^{-i\gamma \int_0^t (G_x(\tau)x + G_y(\tau)y) d\tau} dx dy \quad (2.10)$$

where  $G_x$  and  $G_y$  correspond to the time-varying gradients fields at any given instant  $\tau$ .

When it comes to data acquisition it is rather important to understand how the spatial-frequency domain matrix of data – designated k-space (Ljunggren, 1983) – works. By defining the axis of k-space as we consider that:

$$k_x(t) = \frac{\gamma}{2\pi} \int_0^t G_x(\tau) d\tau \quad (2.11)$$

and

$$k_y(t) = \frac{\gamma}{2\pi} \int_0^t G_y(\tau) d\tau \quad (2.12)$$

Thus, equation 2.10 is equivalent to:

$$S(t) = \iint_{xy} M_{xy} e^{-i2\pi k_x(t)x} e^{-i2\pi k_y(t)y} dx dy \quad (2.13)$$

Since the MR signal can be represented by a function in a coordinate system having  $k_x$  and  $k_y$  as its two axes, it should be noticed that this system has units in spatial frequency (1/distance). By considering  $k_x$  and  $k_y$  as time integrals of the gradient waveform, it is easier to understand that through the waveform manipulation, it becomes possible to control the sampling path of k-space when signal is being acquired.

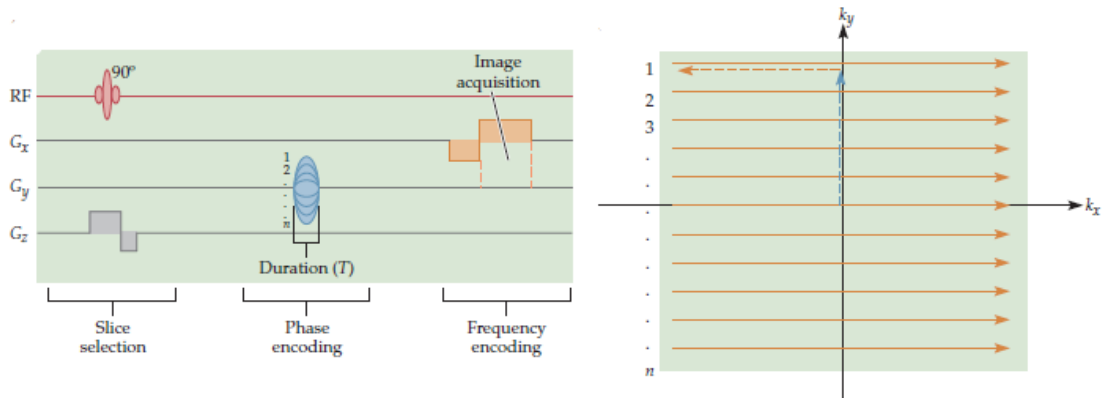


**Figure 2.15** – (Left) Pulse sequence identical to the observed in Figure 2.14. (Right) Pattern traversed by the sequence from (Left) in k-space. Each k-space line is acquired after a separate excitation, then the application of the  $G_y$  at a particular strength (resulting in an upward or downward motion in k-space) and at last the application of the  $G_x$  at a constant strength and duration (resulting in a rightward motion in k-space). Adapted from (Huettel et al., 2014).

By applying the Fourier transform to this sampled time-dependent signal  $S(t)$ , the various frequencies specific to a point in the image are calculated and the image can be reconstructed. Both spatial resolution and signal-to-noise ratio (SNR) are important characteristics reflecting image quality in MRI, considering SNR as the ratio between the amplitude of the signal received and the average noise of the image. The spatial resolution is defined by the size of the voxel in an image, and it is possible to be obtained considering the field of view (FOV), the matrix size – which corresponds to the number of rows and columns in an image – and slice thickness. It is noteworthy to highlight that if the spacing between nearby data points in k-space decreases, the FOV of the reconstructed image increases, whereas if the extent of k-space increases, the pixel size diminishes (higher resolution). However, the measured signal is lower and temporal resolution is affected negatively due to the fact that more k-space lines require acquisition and subsequently a longer acquisition period of time.

## 2.2.4 Contrast Mechanisms

To understand image contrast, two primary types of contrast should be considered: static and motion contrasts.

### 2.2.4.a. Static Contrasts

Static contrasts account for differences in relaxation constants ( $T_1$ ,  $T_2$ ,  $T_2^*$ ), density (e.g., proton density), chemical concentration and particular types of molecules concentrations. Motion contrasts, on the other hand, are sensitive to the atomic nuclei movement, providing information about dynamics such as blood oxygenation (in fMRI), capillary irrigation (in perfusion-weighted imaging) and water diffusion (in diffusion-weighted imaging), which shall be focused on later. Different tissues such as white matter or gray matter have different relaxation properties, easily noticeable in an MRI image. However, one should carefully choose the suitable parameters for a given image contrast. Echo Time (TE) – the time between the RF pulse application and signal acquisition, depicted in Figure 2.16 – and Repetition Time (TR) – the time between consecutive pulse sequences – are two of the most important parameters to contemplate, since their combination in a pulse sequence will define the obtained relaxation contrast. The amount of  $T_1$  relaxation weighting is determined by TR, whilst the amount of  $T_2$  relaxation weighting is controlled by TE. Considering that the MR signal depends also on the imaged tissue properties, rather than only on the original magnetization – dependent on proton density – the transverse magnetization – translated to detectable MR signal – can be now described as shown in equation 2.14.

$$M_{xy}(t) = M_0 \left( 1 - e^{-\frac{TR}{T_1}} \right) e^{-\frac{TE}{T_2}} \quad (2.14)$$

Equation 2.14 enables the manipulation of a particular tissue signal by altering TR and TE. Through the measurement of signal differences between types of tissue, one can compare MR signals from different tissues types, and hence a contrast between them. For example, in  $T_1$ -contrast images, the contrast between light and dark measures the relative difference in the  $T_1$  property of tissues. This is why white matter appears as light gray, gray matter as dark gray and fluid as black. In the case of  $T_2$ -contrast images, the contrast measures different tissue properties causing gray matter to appear as light, white matter to appear as dark and fluid to appear very bright. This results from the longer time it takes for the fluid to lose its transverse magnetization, when compared to other tissues. In the case of  $T_1$ , its contrast is explained given the fact it also takes longer than other tissues to recover its longitudinal magnetization component. Figure 2.16 provides an example of the necessary TR and TE values to generate  $T_1$  and  $T_2$  contrasts in different tissues.

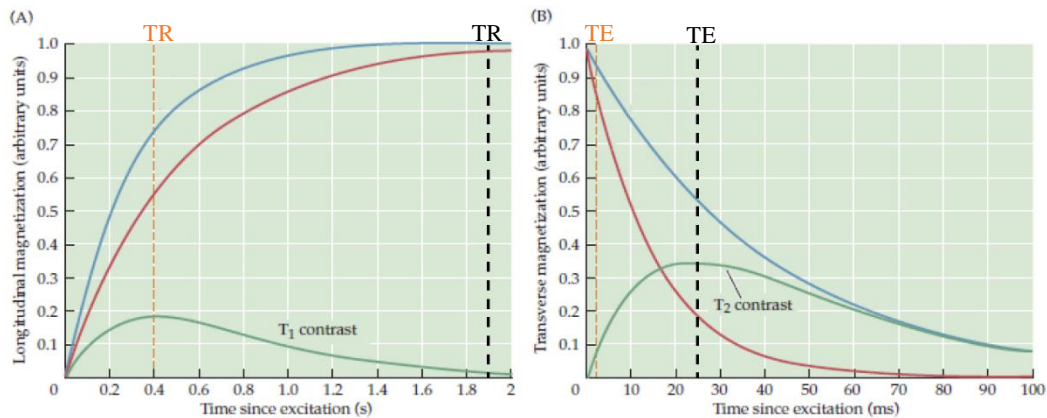


**Figure 2.16** – Selection of TR and TE values for  $T_1$  contrast (vertical orange dashed lines) and  $T_2$  contrast (vertical black dashed lines). The use of intermediate TR and short TE on two tissues (red and blue lines) will maximize  $T_1$  differences between tissues and minimize  $T_2$  differences between tissues, providing a  $T_1$  contrast. The use of long TR and intermediate TE on two tissues will maximize the  $T_2$  differences between tissues while minimizing the  $T_1$  differences between tissues. The green lines show relative contrast associated with different TR (A) and TE (B) values. Adapted from (Huettel et al., 2014).

$T_2^*$  contrast stands as a type of contrast which relies on the  $T_2^*$  values of tissue, briefly introduced in subchapter 2.2.1.c. The  $T_2^*$  signal decay is influenced by the effects of the inherent spin-spin interaction ( $T_2$ ) and the coherence loss due to field inhomogeneities (Chavhan et al., 2009). The  $T_2^*$  signal decay is always quicker than the  $T_2$  decay and its contrast is enabled by intermediate TE and long TR values.  $T_2^*$ -weighted images are usually used for blood-oxygen-level-dependent functional MRI (BOLD-fMRI) since it is able to provide useful information about the presence of deoxygenated haemoglobin, for instance, which is paramagnetic (i.e., concentrates magnetic field lines, increasing the local magnetic field strength), and hence decreases magnetic field homogeneity.

#### 2.2.4.b. Motion Contrasts

Motion contrasts, as previously presented in the beginning of subchapter 2.2.4, offer information on the characteristics underlying proton dynamics. Here, pulse sequences sensitive to motion (blood flow, blood oxygenation or water diffusion), are selected and both structural and functional information can be provided. Magnetic resonance angiography (MRA), which non-invasively provides images with respect to large blood vessels structure, and diffusion tensor imaging (DTI), explained in detail in the following chapter, are examples of imaging techniques entailing motion contrasts. Another commonly used technique is perfusion-weighted imaging (PWI), a type of MRI which provides information on tissue blood flow – such as regional blood volume, mean transit time (MTT) and regional blood flow – in small vessels by using contrast agents (Barbier et al., 2001).

#### 2.2.5 MRI Pulse Sequences

Although there is a wide variety of pulse sequences used in MRI, they are likely to be based on two elementary and very commonly used sequences: the spin echo (SE) sequence and the gradient-echo (GE) sequence. As proposed by Hahn in 1950, the dephasing due to inhomogeneities can be reversed through a subsequent application of a  $180^\circ$  RF pulse as it is shown in Figure 2.17 (left) (Hahn, 1950). Here, the SE sequence begins with a  $90^\circ$  pulse, followed by a  $180^\circ$  refocusing pulse allowing for true spin-spin relaxation without being influenced by field inhomogeneities. This  $180^\circ$  pulse flips the direction of the precession at the TE/2 time point and aims at reversing the loss of phase coherence, which should be reached by time TE. In this case, the sequence is influenced by  $T_2$  and no longer by  $T_2^*$ . The GE sequence, as presented in Figure 2.17 (right), is composed by a gradient reversal on the frequency-encoded axis which forms the echo, only using gradients for this purpose and for signal refocusing. This type of sequence, as opposed to SE, will be sensitive to field inhomogeneities since there is no refocusing  $180^\circ$  pulse, hence being influenced by  $T_2^*$  (Bernstein et al., 2004).

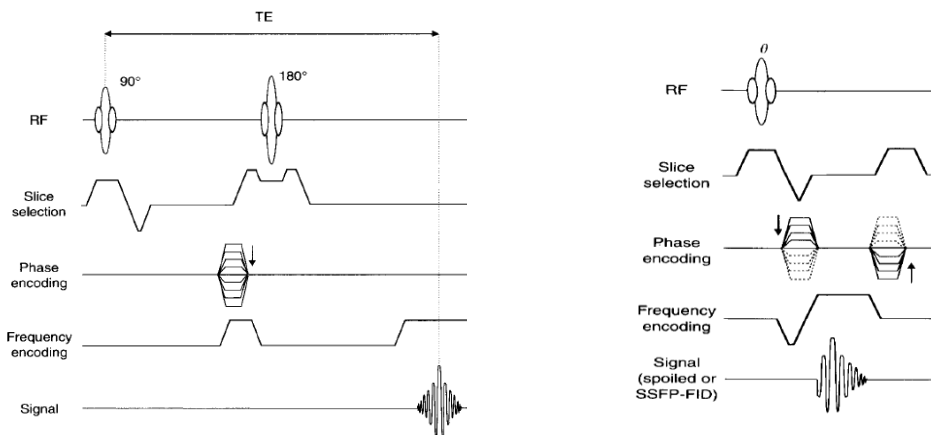


**Figure 2.17** – (Left) A single-echo RF Spin Echo pulse sequence. (Right) Pulse sequence used for Gradient Echo acquisitions Adapted from (Bernstein et al., 2004).

One important aspect that has become increasingly important in imaging is to acquire data rapidly. Accelerating the acquisitions greatly improves the feasibility of clinical imaging and enables new contrasts to be imposed (e.g., functional MRI). One of the most successful acceleration approaches in MRI is the Echo Planar Imaging (EPI) pulse sequence, by far one of the fastest MRI sequences, proposed by Mansfield in 1977, which led to a Nobel Prize in 2003 (shared with Lauterbur, whose contributions were explained in subchapter 2.2.3). To accelerate data acquisition, EPI employs several bipolar – two lobes with opposite polarity – readout gradients so that a train of gradient echoes is induced (since gradient echoes can be produced at a much faster rate than RF spin echoes), as presented in Figure 2.18, after a single excitation from a transmitter coil. By being accompanied by a phase encoding gradient “blip”, each echo is spatially encoded such that the entire k-space is filled and a 2D image can be constructed after a single shot (Bernstein et al., 2004). Due to the fact that all of k-space needs to be filled following this single pulse, it is worth mentioning that data needs to be acquired before significant  $T_2^*$  decay occurs (Huettel et al., 2014). The speed provided by this ultrafast imaging has proved to be advantageous in many MR applications, such as perfusion imaging, cardiac imaging, and diffusion imaging. However, EPI is prone to some artifacts when compared to conventional spin-echo and gradient-echo imaging, such as ghosting in the phase-encoded direction. These “ghosts” can arise from different factors like concomitant magnetic fields or eddy currents but can be attenuated or removed with postprocessing techniques or reconstruction.

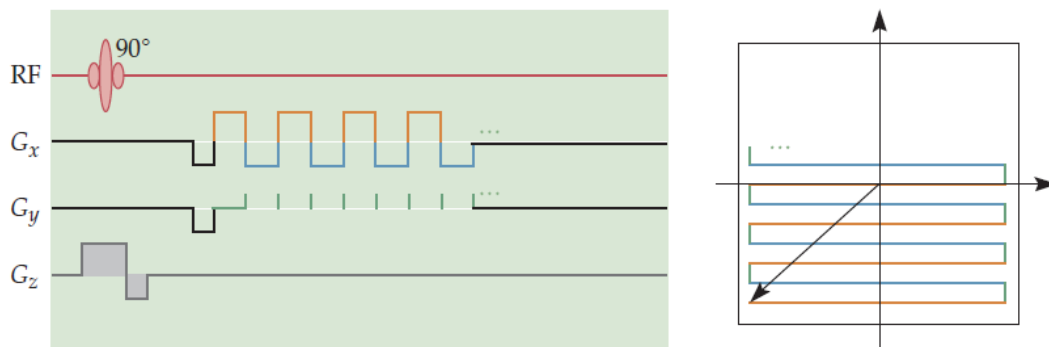


**Figure 2.18** – (Left) An EPI pulse sequence. (Right) Its k-space trajectory. The black arrow points at the starting initially negative  $G_x$  and  $G_y$  gradients which are used to move to the bottom left of k-space. Both representations are colour coded in order to ease the comparison between pulse sequence and k-space representation. Adapted from (Huettel et al., 2014).

## 2.3 Diffusion Magnetic Resonance Imaging

A diffusion weighting contrast is based upon the application of controlled magnetic field gradients that weigh the diffusion process into the MR signal and results in its attenuation. By probing the diffusion process, diffusion-weighted MRI provides with a way to characterize tissue microstructure, hence potentially reporting also on pathological alterations at a microscopic level. This subchapter details the main principles of diffusion that would be essential for the comprehension of the role of signal representation (further described) especially when mapping tissue abnormalities.

### 2.3.1 Diffusion Principles

Diffusion is a thermal mass transport phenomenon occurring in nature and giving origin to a particle or molecular mixing. Diffusion was first noticed by the botanist Robert Brown in 1827 as a motion based on random translation trajectories which were then witnessed in pollen grains moving



randomly when suspended in water (Figure 2.19) (Brown, 1829). The Fick's law explains this mixing process by relating the diffusive flux to a difference in concentration by:

$$J(r, t) = -D\nabla c(r, t) \quad (2.15)$$

where  $J(r, t)$  corresponds to the net particle flux vector,  $D$  is the diffusion coefficient and  $c(r, t)$  is the particle concentration. Fick's second law is achieved by combining equation 2.15 with the conservation of mass law introduced by Lavoisier, resulting in the diffusion equation:

$$\frac{\partial c(r, t)}{\partial t} = D\nabla^2 c(r, t) \quad (2.16)$$

In the case of diffusion, the flux is proportional to the diffusion coefficient and the concentration gradient. However, it is worth mentioning that the diffusion coefficient is an intrinsic medium property and depends on the size of the molecules that are diffusing, as well as on the microstructural characteristics of the environment and the temperature. In equilibrium there is no net molecular flux, and in the absence of a net concentration gradient, it is known that molecules will still move randomly and microscopically, according to what discovered by Brown.

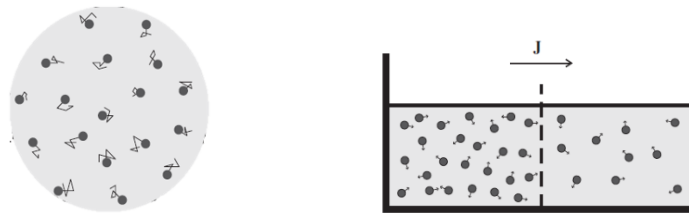


**Figure 2.19** – (Left) The botanist Robert Brown noticed the motion of pollen grains when suspended in water (1827). (Right) Particles have a tendency, on average, to move from high concentration regions to low concentration regions, resulting in a net flux, in accordance with Fick's first law. Adapted from (Kubicki & Shenton, 2014).

By using a probabilistic framework, Einstein was able to explain such random motions in an ensemble of particles experiencing diffusion, introducing the “displacement distribution” in order to quantify the fraction of particles that traverse a given distance  $\Delta r$  in a given time (Einstein, 1905). As presented in Figure 2.20, in free diffusion the displacement distribution is a Gaussian function:

$$P(r|r_0, t) = \frac{N}{\sqrt{2n\pi Dt}} e^{-\frac{|\Delta r|^2}{2nDt}} \quad (2.17)$$

with  $\Delta r = r - r_0$ , means  $\mu = 0$  and variance  $\sigma^2 = 2Dt$ , considering that  $N$  particles start from the origin  $r_0$  at time  $t = 0$ , and  $n$  stands for the number of dimensions. The larger the diffusion coefficient, the broader the displacement probability. For instance, media in gas state has larger diffusion coefficient than liquids.

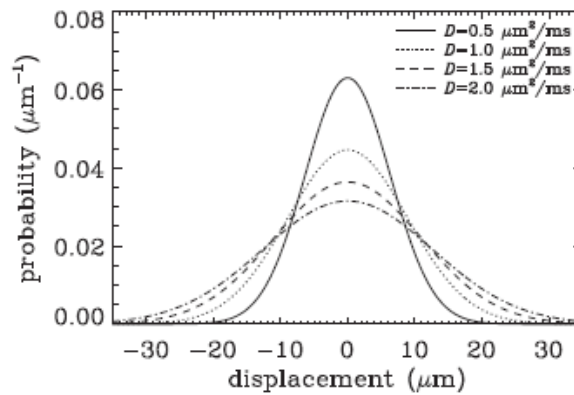


**Figure 2.20** – Gaussian displacement distribution for different diffusion coefficient values. The larger the diffusion coefficient, the broader the displacement probability. Extracted from (Kubicki & Shenton, 2014).

The mean square displacement for free diffusion can be calculated from equation 2.17:

$$\langle (r - r_0)^2 \rangle = \int_{-\infty}^{\infty} (r - r_0)^2 P(r|r_0, t) dr dr_0 = 2nDt \quad (2.18)$$

with  $n = 1$  if diffusion is along one dimension,  $n = 2$  if it is along two dimensions and  $n = 3$  if it is along three dimensions.

Measuring diffusion using NMR signals has been a very active field of development since the very beginning of the field. Diffusion weighting is based on the application of controlled gradient magnetic fields used to quantify the direction of diffusion of water molecules and given their presence it is possible to attenuate the MR signal further than the one caused by common  $T_2$  relaxation. Back in 1950, Hahn reported a reduction of signal of the spin echo and explained it based on a spin dephasing provoked by translational diffusion when considering an inhomogeneous magnetic field (Hahn, 1950). However, there was not a direct method to measure the diffusion coefficient of a solution with spin-labelled molecules. It was only in 1954 when Carr and Purcell provided a reformulated and extended version of Hahn’s approach to diffusion sensitization that this measurement was enabled. Based on the application of a constant field gradient during the experiment and using Hahn’s NMR spin echo sequence, as presented in Figure 2.21, (Carr H. Y. & E.M., 1983), the idea is to apply a “magnetic field gradient” such that spins differently located precess at different angular frequencies, hence acquiring different phase shifts. Since then, NMR has been of high importance when it comes to measuring molecular diffusion. Some years later, Torrey generalized the previously mentioned Bloch equations (equation 2.4, 2.5 and 2.6) in order for them to include the effects arising from diffusion (Torrey, 1956).

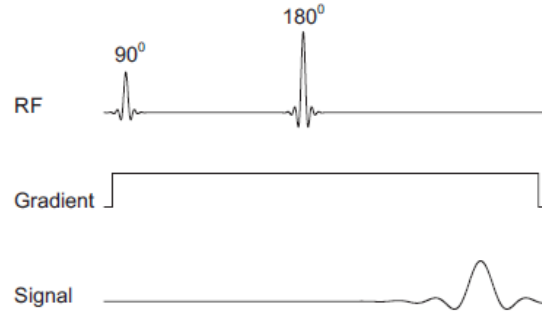


**Figure 2.21** - Constant gradient field spin echo approach presented by Carr and Purcell in 1954. Extracted from (Basser & Ozarslan, 2014)

The previous constant diffusion-encoding gradient approach does not allow, however, to distinct between encoding time (pulse duration,  $\delta$ ) and diffusion time (separation of the two pulses,  $\Delta$ ) Stejskal and Tanner proposed the application of a diffusion-gradient in two matched pulses, each placed before and after the  $180^\circ$  pulse, also known as the pulsed gradient spin echo (PGSE) sequence, as shown in Figure 2.22 (Stejskal & Tanner, 1965).

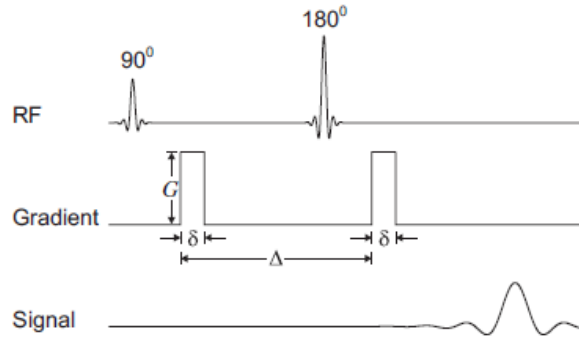


**Figure 2.22** - Spin echo sequence with proposed application of a time-dependent field gradient by Stejskal and Tanner in 1965. Extracted from (Basser & Ozarslan, 2014).

In this framework, it is worth mentioning that by assuming a “narrow pulse” regime, the diffusion gradients are so short that the diffusion occurring between these pulses’ application can be disregarded. Hence, by considering that each gradient pulse induces a given net phase change, in which the particle is at a given position, and that the  $180^\circ$  RF pulse applied in between reverses the phase change occurring prior to it, the resulting net phase change is given by:

$$\phi_2 - \phi_1 = -q(x_2 - x_1) \quad (2.19)$$

where  $\phi_1$  is the net phase change induced by the first gradient pulse and  $\phi_2$  is the net phase change resulting from the second gradient pulse.  $x_1$  and  $x_2$  correspond to the particle position during the application of the first pulse and second pulse, respectively. The quantity  $q = \gamma\delta G$  was considered, where  $G$  corresponds to the gradient pulse magnitude.

Assuming that particles are moving randomly throughout an excited volume, the gained phase increment during the first period  $\phi_1$  does not (generally) cancel the phase decrement occurring upon the second period  $\phi_2$ . Thus, since there is a resulting phase dispersion among these spins’ population, the signal is attenuated.

By dividing the diffusion-attenuated signal,  $S(q)$ , by the signal in the absence of gradients,  $S_0 = S(0)$ , a quantity  $E(q)$  can be introduced (i.e.,  $E(q) = S(q)/S_0$ ). This way, relaxation effects are

eliminated, and  $E(q)$  is exclusively diffusion dependent, leading to the MR signal attenuation proposed by (Stejskal, 1965):

$$E(q) = \int \rho(x_1) \int P(x_1, x_2, \Delta) e^{-iq(x_2 - x_1)} dx_2 dx_1 \quad (2.20)$$

where  $\rho(x_1)$  is the spin density when the first pulse is first applied. This quantity quantifies the likelihood of finding a spin at location  $x_1$ .  $P(x_1, x_2, \Delta)$  corresponds to the diffusion propagator, which accounts for the likelihood of a particle, which was at location  $x_1$ , ending up at  $x_2$  after a time  $\Delta$ .  $e^{-iq(x_2 - x_1)}$  encompasses the phase change resulting from diffusion.

The propagator is Gaussian when diffusion is free, and subsequently the MR signal attenuation is provided by:

$$E(q) = e^{-q^2 D (\Delta - \frac{\delta}{3})} = e^{-bD} \quad (2.21)$$

where  $b = q^2 \left( \Delta - \frac{\delta}{3} \right) = (\gamma \delta G)^2 \left( \Delta - \frac{\delta}{3} \right)$ . This  $b$  quantity, b-factor or “b-value” is used to characterize the degree of sensitivity which is induced on diffusion. Assuming isotropic diffusion (Figure 2.23 (A)) along all directions,  $D$  stands as the apparent diffusion coefficient (ADC) – the calculated value of the diffusion coefficient. However, this is not the case for water molecules in the brain, where they can have a given preference to diffuse in a certain direction (anisotropic diffusion, Figure 2.23 (B)). In neural tissue, water molecules tend to diffuse more freely according to the fibre direction, giving rise to the possibility of relating quantified orientational preference to axonal orientations. By considering the diffusion tensor anisotropic diffusion is more properly addressed (with free diffusion in a homogeneous media, (Stejskal & Tanner, 1965)). Thus,  $D$  is now a symmetric tensor, fully describing molecular mobility along each axis, as well as correlation between displacements along these axes (Basser & Ozarslan, 2014). As for the b-value, this previously scalar quantity is now replaced by the b matrix, expressed in the coordinates of the gradients reference frame.

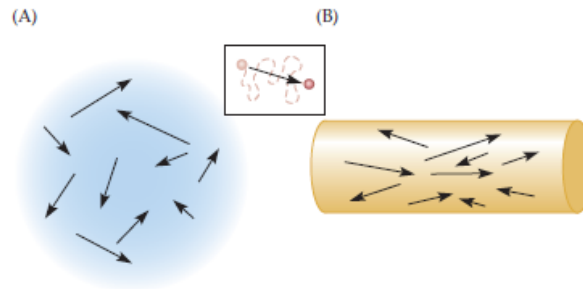


**Figure 2.23** - (A) isotropic diffusion and (B) anisotropic diffusion. Extracted from (Huettel et al., 2014).

Through gradient application one can enhance diffusive attenuation as mentioned in the case of spin echoes, as previously mentioned. This attenuation leads to a rather different contrast mechanism when compared to the previously presented mechanisms, giving rise to diffusion-weighted images, which have been used extensively in neuroimaging.

### 2.3.2 Diffusion MRI modelling and Signal Representation in DWI

Seeking sensitivity and specificity remains an important challenge in dMRI. The characterization of white matter using DWI has proven to be very sensitive to alterations related to neurological diseases and microstructural modelling can link the diffusion MRI signal to biological properties since the early 1990's, with a first attempt by Latour et al. in 1994 aiming at the modelling of the diffusion signal in packed erythrocytes surrounded by an extracellular environment (Latour et al., 1994). For example, the NODDI multi-compartment model (Adluru et al., 2014), which uses a Watson orientation distribution function (ODF) and the WMTI, a two-compartment model which derives parameters as a function of diffusion and kurtosis metrics, have been important candidates to assess alterations in tissue under ischemic conditions (Hui et al., 2012), but since their assumptions were proved to be invalid, it remains a challenge for these to correctly estimate tissue's microstructure (Henriques et al., 2019).

#### 2.3.2.a. Diffusion Tensor Imaging (DTI)

On the other hand, signal representations, sometimes referred to as “statistical models” aim to characterize properties from the dMRI signal without specifically linking the signals to an underlying biological component, i.e., without assumptions on the underlying tissue. The cumulant expansion – a logarithm expansion of the signal in polynomials, stands as the most common signal representation. In the case of DTI – an example of an expansion up to the first order in  $b$  (Novikov et al., 2018) – it was introduced to describe anisotropic diffusion, and is widely used to study, among others, structural connectivity and tractography of pathological WM (Horsfield & Jones, 2002; Sotak, 2002). The diffusion ellipsoid is described as a three-dimensional tensor – a  $3 \times 3$  covariance matrix known to describe the diffusion displacement of a single voxel:

$$D = \begin{bmatrix} D_{xx} & D_{xy} & D_{xz} \\ D_{xy} & D_{yy} & D_{yz} \\ D_{xz} & D_{yz} & D_{zz} \end{bmatrix} \quad (2.22)$$

which is based on a vector fields collection regulated by three main axes (i.e., the three logical axes of the scanner measurement frame) and off-diagonal elements which reflect the displacements correlation along those main axes, yielding the eigenvalues ( $\lambda_1, \lambda_2, \lambda_3$ ) and corresponding eigenvectors ( $\epsilon_1, \epsilon_2, \epsilon_3$ ). The tensor is possible to be visualized as an ellipsoid, having its radii characterized by the eigenvalues and the directions of the principal axes characterized by the eigenvectors, as presented in Figure 2.24 (Basser et al., 1994).

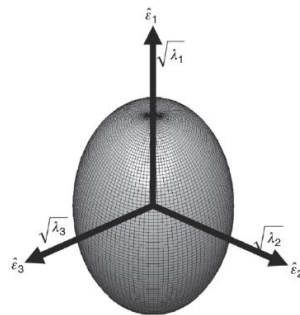


**Figure 2.24** – Diffusion tensor ellipsoid, considering it as the envelope where a spin, which is placed at its centre, will diffuse with the same probability. The square root of the eigenvalues ( $\lambda_1, \lambda_2, \lambda_3$ ) were the reference for the scaling of the axes, with the principal axes accounting for the corresponding eigenvectors ( $\hat{\epsilon}_1, \hat{\epsilon}_2, \hat{\epsilon}_3$ ). Extracted from (Jones, 2014).

The diffusion tensor can be estimated via fitting an adaptation of the Stejskal and Tanner equation to a minimum of six diffusion-weighted images acquired for a minimum of six gradient directions (non-colinear), and an image without diffusion weighting, i.e.,  $b\text{-value} = 0 \text{ s/mm}^2$ , described by:

$$S(n, b) = S_0 e^{-bn^T D n} = S_0 e^{-b \sum_{i=1}^3 \sum_{j=1}^3 n_i n_j D_{ij}} \quad (2.23)$$

with  $n$  accounting for a unit vector along a given direction ( $n_x, n_y, n_z$ ).  $S(n, b)$  corresponds to the signal of the diffusion-weighted voxels. The tensor eigenvalues provide relevant values of diffusivity which can be further used to compute important quantities, such as mean diffusivity (MD), radial diffusivity (RD), axial diffusivity (AD) and fractional anisotropy (FA) (Basser, 1995).

Thus, instead of being characterized by a single scalar coefficient, diffusion is now characterized by a symmetric tensor,  $D$ , known for quantifying the relative diffusivity of water into directional components in a single voxel. A rather interesting example can be seen in white matter, which shows major anisotropy, causing a preferential diffusion along the length of the nerve fibres, and slower diffusion perpendicular to the main axis. Through DTI, data from diffusion provides information on orientation of the fibres from the microscopic diffusion process for each voxel (Bihan, 1995). The mean diffusivity which is proportional to the mean-squared displacement of the water molecules (itself influenced mainly by existence of microscopic obstacles to diffusion); the anisotropy of the system (through fractional anisotropy (FA) – a scalar quantity which can be obtained for each voxel to manifest the water molecules preference to diffuse in an anisotropic or isotropic way and its values are limited from 0 to 1 (Huettel et al., 2014)); and the parallel and perpendicular diffusivities which reflect the microscopic restrictions along the different dimensions. These three parameters characterize the average tensor, represented by an ellipsoid, namely, the ellipsoid size, the eccentricity, and the size of the main ellipsoid axes, respectively.

However, DTI can only capture mono-exponential signal decays, which makes the single tensor representation not always enough for complex system characterization. Among its limitations are the incapability of DTI-based fibre tractography to determine fibre crossings, and its low specificity to histological features (Beaulieu, 2002).

### 2.3.2.b. Diffusion Kurtosis Imaging (DKI)

DKI, on the other hand, emerged as an expansion of DTI in 2005 (Jensen et al., 2005), after the confirmation that water in biological structures had a non-Gaussian behaviour (Assaf & Cohen, 1998; Niendorf et al., 1996). Unlike DTI, by extending the signal representation to second order in  $b$ , it is able to quantify the degree of non-Gaussian diffusion in pathological structures, quantifying the water diffusion profile deviation from Gaussian distribution and has proven to be more specific than the previously mentioned microstructural models (Hui et al., 2012), since it can better characterize areas characterized by lower orientational coherence. The diffusion kurtosis tensor (a fourth-order tensor),  $K$ , can be estimated and describes the diffusional excess-kurtosis – capable of measuring the deviation from the Gaussian distribution (where  $W = 0$ ) – along the three-dimensional direction. Its negative values are related to a less peaked distribution, when compared to the Gaussian distribution, while its positive values reveal a more peaked distribution. Negative kurtosis can be induced by the interactions between water molecules and the compartments barriers or macromolecules.

To fit  $D$  and  $W$  from the diffusion-weighted images, one should consider the extended equation 2.23, defined as:

$$S(n, b) = S_0 e^{-b \sum_{i=1}^3 \sum_{j=1}^3 n_i n_j D_{ij} + \frac{1}{6} b^2 MD^2 \sum_{i=1}^3 \sum_{j=1}^3 \sum_{k=1}^3 \sum_{l=1}^3 n_i n_j n_k n_l W_{ijkl}} \quad (2.24)$$

Considering that b-values are quadratic terms, the kurtosis tensor requires at least 22 measurements, hence 15 independent gradient directions are required for both tensors' analysis.

Despite being more sensitive than DTI, DKI still does not provide specificity. Particularly, since DKI cannot decouple the negative kurtosis effects of tissue interacting water molecules from the positive kurtosis effects of compartment's diffusion variance, the relationship between non-Gaussian effects and tissue properties is hard to establish (Jensen et al., 2005).

Single diffusion encoding (SDE) (terminology introduced by (Shemesh et al., 2016)) contemplates methods that are based on the diffusion MRI data acquired after applying single pairs of diffusion-weighted pulse gradients according to the Stejskal and Tanner experiment explained above, used for instance to obtain measures provided by conventional DTI and DKI metrics. These methods probe the displacements of spins along a single axis, which incurs an inherent averaging over the ensemble of diffusing spins in the imaging voxel. Thus, SDE methods are not able to tackle the characterization of complex systems because of microscopic and mesoscopic features conflation, hence lacking specificity.

### 2.3.3 Double Diffusion Encoding Principles

Advanced diffusion encodings (Cory et al., 1990) – such as double diffusion encoding (DDE) (terminology also introduced by (Shemesh et al., 2016)) or q-space trajectory encoding (Szczeplankiewicz et al., 2014) – are able to resolve microstructural properties from confounding tissue compartment orientation dispersion effects like microscopic fractional anisotropy ( $\mu$ FA), i.e., normalized form of microscopic diffusion anisotropy – information that cannot be captured by SDE techniques without imposing strict model constraints. Particularly, the DDE sequence, first proposed as double pulse gradient spin echo (d-PGSE) in 1990 by Cory et al. and analysed theoretically in detail by Mitra (Mitra, 1995), is based on two diffusion-encoding gradient pulse pairs ( $G_1$  and  $G_2$ ), separated by a mixing time ( $t_m$ ) (Figure 2.25). It was shown that, in angular DDE experiments with long mixing time, the amplitude of the signal modulation as a function of the angle between the two gradient pulse pairs is sensitive to microscopic anisotropy (Jensen et al., 2005), i.e., the average anisotropy of the various components in the ensemble independent of their orientation distribution. Hence, microscopic anisotropy can be measured without relying on specific microstructural models. In comparison with q-space trajectory encoding, DDE techniques have the advantage of not ignoring non-Gaussian diffusion effects due to the interaction of water molecules with tissue obstacles (Cheung et al., 2009).

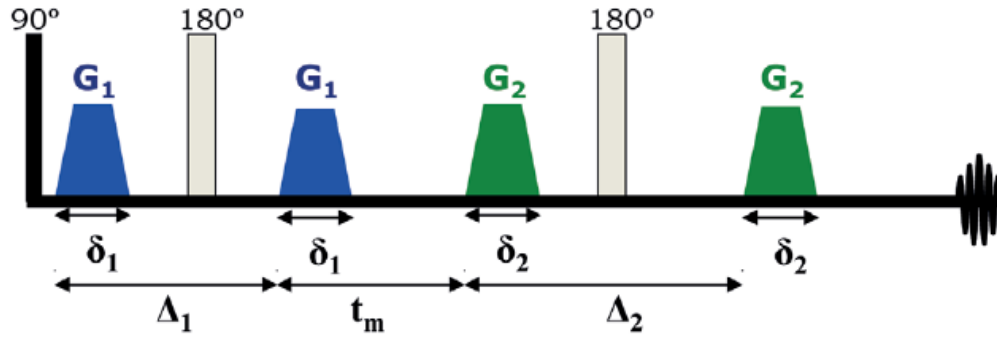


**Figure 2.25** – DDE sequence representation within a double spin echo framework.  $\Delta_1$  and  $\Delta_2$  are the diffusion times,  $\delta_1$  and  $\delta_2$  are the pulse durations,  $G_1$  and  $G_2$  are the gradient amplitudes, and  $t_m$  is the mixing time Adapted from (Shemesh et al., 2016).

The ensuing CTI methodology and its ability to disentangle diffusion kurtosis sources will be presented below, in subchapter 2.4.



## 2.4 Correlation Tensor Imaging (CTI)

Based on a cumulant expansion of the DKI tensor and relying on advanced diffusion sequences, namely double diffusion encoding, CTI was recently presented as a novel methodology capable of resolving kurtosis sources, thereby enhancing sensitivity and specificity towards metrics that are inherently conflated in conventional DWI. The present chapter will introduce single and DDE sequences, the theory behind CTI and how it enables to separate non-Gaussian diffusion sources.

### 2.4.1 CTI Theory

CTI is a novel technique whose framework is based on the cumulant expansion of DDE. In addition to measuring the microscopic diffusion anisotropy, CTI aims to resolving different sources of kurtosis (Henriques, Jespersen, & Shemesh, 2020). Kurtosis, reflecting the degree of tissue non-Gaussianity, can arise from multiple sources, which can be associated with inter-compartmental or intra-compartmental diffusivities: a) anisotropic kurtosis ( $K_{aniso}$ ) or microscopic anisotropy, related to anisotropy from distinct microenvironments – the source arises from the variance across different eigenvalues of the individual diffusion tensor  $D^c$ ; b) isotropic kurtosis ( $K_{iso}$ ) or diffusion from isotropic tensors, corresponding to the mean diffusivities variances in different compartments – notice that mean diffusivity or  $\bar{D} = \text{trace}(D)/3$ ; c) intra-compartmental kurtosis ( $K_{intra}$ ), from the interaction of water molecules with barriers and obstacles of compartments both intra and extracellularly.

DDE's cumulant expansion includes information on the correlation tensor  $Z$  which in turn holds direct information on the isotropic and anisotropic kurtosis contribution ( $K_{aniso}$  and  $K_{iso}$ ). Through CTI,  $K_{intra}$  can then be inferred from the subtraction of the total kurtosis  $K_T$  measured from DKI's kurtosis tensor and the other kurtosis contributions (equation 2.27). Considering equation 2.25 as a similar version of equation 2.23:

$$E_{\Delta} = \langle e^{-q_i q_j \Delta D_{ij}^c} \rangle \quad (2.25)$$

where  $E_{\Delta}$  corresponds to the diffusion-weighted signal decay for a given  $q$ -vector  $q$  with a corresponding magnitude of  $q = \gamma \delta g$ , with  $\gamma$  accounting for the gyromagnetic ratio,  $\delta$  for the gradient pulse duration and  $g$  for the gradient intensity. Here,  $\Delta$  reflects the diffusion time – time duration between the single diffusion encoding module gradient – and  $D_{ij}^c$  correspond to the individual tensor's elements.  $\langle . \rangle$  accounts for the average over several compartments and the superscript 'c' means that it reflects individual component properties (Henriques et al., 2020).

After decomposing the previous equation up to fifth order in  $q$ , both the total diffusion tensor  $D$  and total kurtosis tensor  $W$  are possible to be obtained by:

$$\log E_{\Delta}(q) = -q_i q_j \Delta D_{ij} + \frac{1}{6} q_i q_j q_k q_l \Delta^2 \bar{D}^2 W_{ijkl} + \mathcal{O}(q^6) \quad (2.26)$$

where  $D_{ij}$  and  $W_{ijkl}$  are the elements of the total diffusion and kurtosis tensor, respectively. Equation 2.26 is analogous to equation 2.24, but it follows Einstein's convention and is expressed in function of the  $q$  vector. This equation is followed by the factoring out of orientation dispersion (through powder-averaging of the mean signal decays for a number of directions and constant magnitude  $q$ ) and aims at the expansion of equation 2.25 in cumulants in order to extract the total excess-kurtosis ( $K_T$ ) of the powdered average decays. In addition, for restricted diffusion effects to be considered, the elements of the individual intra-compartmental kurtosis and diffusion tensors shall be contemplated by replacing  $D_{ij}$

by  $D_{ij}^c$  and  $\bar{D}$  by  $\bar{D}^c$  in equation 2.26. Like this, the elements of the individual intra-compartmental kurtosis tensor resulting from restricted diffusion are considered.

The total excess kurtosis ( $K_T$ ) is thus given by:

$$K_T = \frac{6}{5} \frac{\langle V_\lambda(D^c) \rangle}{\bar{D}^2} + 3 \frac{V(\bar{D}^c)}{\bar{D}^2} + \frac{\langle (\bar{D}^c)^2 K_T^c \rangle}{\bar{D}^2} \quad (2.27)$$

with  $K_T^c$  reflecting the powder averaged signals excess-kurtosis in terms of an individual compartment, and the denominators rely on  $\bar{D}^2$  since it reflects the diffusivity over all compartments (Jespersen et al., 2013).  $V_\lambda(D^c)$  represents the eigenvalue variance of an individual tensor  $D^c$ , and  $V(\bar{D}^c)$  is the mean diffusivities variance across microenvironments.

In equation 2.27 each addend reflects different sources. The first, second and third addends account for  $K_{aniso}$ ,  $K_{iso}$  and  $K_{intra}$ , as shown in Figure 2.26.

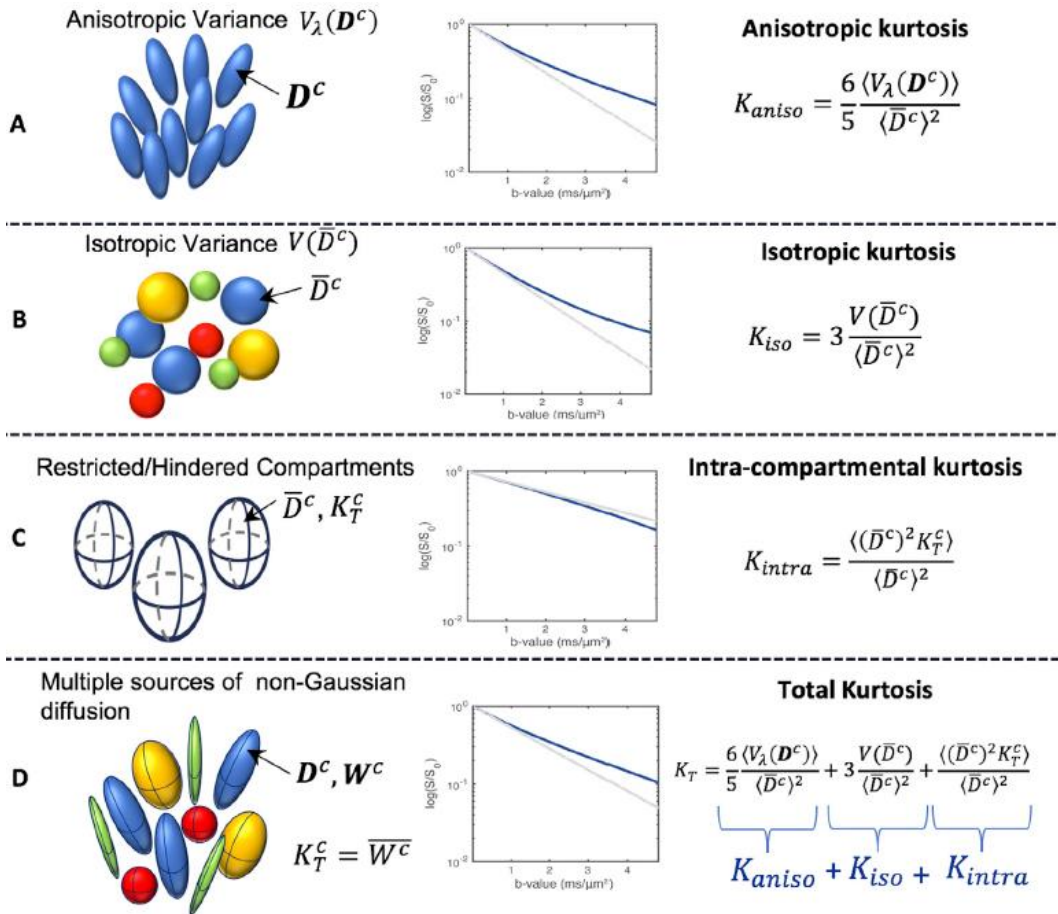


**Figure 2.26** – Representation of inter-compartmental and intra-compartmental kurtosis sources. (A) Kurtosis is possible to arise in the dMRI signal decay in the case of replicas of the single diffusion tensor ( $D^c$ ) being dispersed (mesoscopically) in various directions –  $K_{aniso}$ . (B) Kurtosis may also arise from polydisperse tensor traces, with no orientation dispersion –  $K_{iso}$ . (C) Kurtosis can also arise from non-Gaussian, restricted diffusion –  $K_{intra}$ . Extracted from (Henriques et al., 2020).

## 2.4.2 Correlation Tensor Imaging Extraction via Double Diffusion Encoding

The correlation tensor imaging approach relies on DDE's cumulant expansion with signal expressed in terms of 2<sup>nd</sup> order tensors ( $Q$ , encoding information on the time dependence of  $D$ ) and 4<sup>th</sup> order tensors ( $Z$  and  $S$ ), in addition to the previously considered diffusion and kurtosis tensors ( $D_{ij}$  and  $W_{ijkl}$ ). Intra-compartment kurtosis ( $K_{intra}$ ) is possible to be derived from  $Z$  and  $D$ , hence obtained by subtracting  $K_{aniso}$  and  $K_{iso}$  from  $K_T$  (equation 2.28) (Henriques et al., 2020).

$$K_{intra} = K_T - K_{aniso} - K_{iso} \quad (2.28)$$

Thus, considering that DDE encompasses two diffusion encoding modules described by different  $q$ -vectors ( $q_1$  and  $q_2$ ) and assuming equal diffusion times  $\Delta_1 = \Delta_2 = \Delta$ , the signal can be expressed by (Henriques et al., 2020) :

$$\begin{aligned} \log E_{\Delta}(q_1, q_2) = & -(q_{1i}q_{1j} + q_{2i}q_{2j})\Delta D_{ij} + q_{1i}q_{2j}Q_{ij} \\ & + \frac{1}{6}(q_{1i}q_{1j}q_{1k}q_{1l} + q_{2i}q_{2j}q_{2k}q_{2l})\Delta^2 \bar{D}^2 W_{ijkl} \\ & + \frac{1}{4}q_{1i}q_{1j}q_{2k}q_{2l}Z_{ijkl} + \frac{1}{6}(q_{1i}q_{1j}q_{1k}q_{2l} + q_{2i}q_{2j}q_{2k}q_{1l})S_{ijkl} + \mathcal{O}(q^6) \end{aligned} \quad (2.29)$$

For the purpose of CTI it is advantageous to suppress the  $Q$  and  $S$  tensors by applying a long mixing time in the DDE experiments (Jespersen, 2012), or by combining DDE acquisitions with inverted  $q_2$  vectors.

## 2.5 Non-MR imaging methods for detecting acute ischemic stroke

Acute ischemia and the criteria to rule out haemorrhagic stroke have been evaluated since the 1970s by non-contrast Computed Tomography (CT) at a useful speed, low cost and widespread availability (Figure 2.27) (Lodder, 1984; Russel, 1997). Head CT scans can detect ischemia within 6 h post onset and its sensitivity has been suggested to be comparable with conventional T2-weighted magnetic resonance imaging (T2WI) (Mohr et al., 1995). However, CT techniques evolved towards other purposes rather than just aiming at the exclusion of haemorrhagic stroke (Norrving, 2014). One example is CT angiography (CTA), which improves the sensitivity to which early ischemic changes can be identified with better contrast and information on collateral circulation. CT Perfusion is also an approach for imaging tissue at risk by measuring regional cerebral blood volume (rCBV) and dividing it by the mean transit time (MTT) for further calculation of regional cerebral blood flow (CBF) – defined as the blood volume that flows per unit mass per unit time in tissue. The radiation required for this CT approach is, however, substantial, making it unfeasible for serial measurements. Techniques like single-photon emission computed tomography (SPECT) and Xenon-SPECT use radiotracers. Despite its safety, the former is not able to measure metabolism and absolute CBF, whereas the latter one accounts for a quantitative CBF measurement but cannot provide good spatial resolution (H. Y. Wey et al., 2013).

Imaging techniques are especially important in the context of furthering our understanding on the impact of acute neurological deficits on functional outcomes, and, in particular, they are crucial for identifying “tissue at risk” as early as possible. Positron Emission Tomography (PET) was the first technique to demonstrate penumbra’s existence back in 1981 by being able to identify it as tissue with reduced CBF but normal Cerebral Metabolic Rate of Oxygen ( $CMRO_2$ ) – the rate of oxygen consumption by the brain (Baron et al., 1981). This technique evaluates the involved pathology and offers semi-quantitative or quantitative hemodynamic data. Inside PET there is a range of techniques, such as the multi tracer PET with  $^{15}O$  (which offers quantitative maps of CBF, cerebral blood volume (CBV) - defined as ml of blood per 100 g of brain tissue,  $CMRO_2$  and cerebral metabolic rate of glucose ( $CMR_{glu}$ )).

The penumbral region has reduced CBF but maintained  $CMRO_2$  secondary to increased oxygen extraction fraction (OEF), which is the ratio of oxygen that a tissue takes from the brain blood flow to preserve function and morphological integrity. This method is limited due to high variability in CBF values in the penumbral area. This issue gave origin to other PET techniques, like PET with flumazenil (FMZ) - a selective  $\gamma$ -Aminobutyric acid type A (GABAA) receptor antagonist –, but they remain invasive, and can be time consuming when using certain radiotracers, with poor spatial and temporal resolution. PET with fluoromisonidazole (FMISO) – a radiotracer for imaging hypoxia – is another branch arising from PET which is able to label the penumbral area based on acquiring where the tissue is metabolically active and not able to re-oxidize the metabolite to the initial form (hypoxic tissue). This technique holds, however, some drawbacks regarding the time required before image can be attained and unexpected binding to not penumbral tissue (Merino & Warach, 2010; H. Y. Wey et al., 2013).

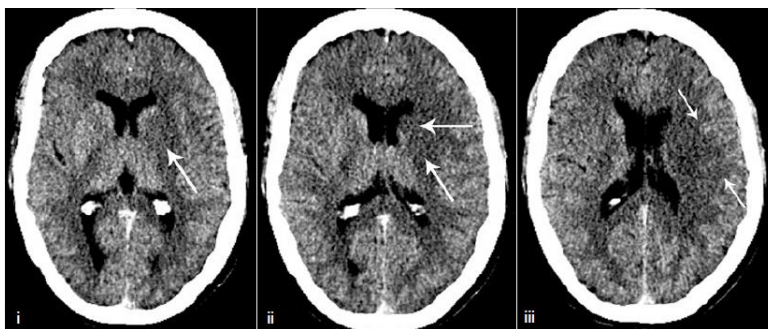


**Figure 2.27** – (a) Patient last seen normal at 10 pm, found early the following morning with right hemiplegia and severe aphasia. Non-contrast CT shows several early ischemic changes: (i, ii) Lenticular nucleus and caudate head hypodensity (arrows), and (iii) cortical swelling with sulcal effacement (arrows). Extracted from (González et al., 2011).

## 2.6 MRI in stroke

As previously mentioned, an important goal for imaging in the scope of stroke is to be able to detect it as acutely as possible, targeting sensitivity towards important alterations that might be occurring because of stroke cascade of events. Both T2-weighted imaging (T2WI) and T1-weighted imaging (T1WI) are efficient at identifying vasogenic edema at a subacute-to-chronic stage (~24 h) (Quast et al., 1993), with 90% of visible infarctions in the case of T2WI and only 50% in T1WI (Yuh et al., 1991). Regarding sensitivity at a more acute phase, conventional MRI assumes a poor performance with a sensitivity lower than 50% when imaging stroke within the first 6 hours post ischemia (Gonza et al., 1999; Mohr et al., 1995). Moreover, distinguishing necrotic tissue from tissue at risk is not possible through T2WI only, making it necessary to combine with Diffusion-weighting imaging (DWI) in order to approach salvageable tissue at an early point in time (Welch et al., 1995).

Since a CBF disturbance occurs first upon an ischemic infarct, some perfusion MRI techniques, in addition to CT-perfusion, have also been developed to detect the decline in CBF. For example, dynamic susceptibility contrast (DSC) MRI – which requires a gadolinium-based contrast agent bolus injection – and arterial spin labelling (ASL) MRI – which utilizes a unique contrast mechanism relying on RF pulse labelling of inflowing blood requiring no additional contrast agent – both provide a good depiction of the reduced blood flow (Copen et al., 2011). Still, the requirement of potentially toxic contrast agents for the former make it somewhat less attractive, while the latter's efficacy and optimal imaging parameters remain to be determined in a clinical setting. Furthermore, neither method reports on the underlying cellular-level changes to the tissues, hence not being considered ideal so far for vascular diseases imaging (H. Y. Wey et al., 2013).

Blood-brain barrier (BBB) permeability imaging takes advantage of the BBB disruption after acute stroke. The BBB is a boundary which has the function to separate blood from tissue in healthy conditions. It allows passive diffusion of small molecules and active metabolite transportation. Hence, it corresponds to a potential candidate for stroke prediction and can offer information associated with tissue regeneration (Ding et al., 2006; Pillai et al., 2009). For the measurement of its permeability, DSC MRI can be used to monitor the contrast agents' leakage into brain tissue.

MR spectroscopy (MRS), by providing non-invasive information about the metabolic pattern of the brain parenchyma *in vivo* can be approached to assess the concentration of lactate and pH since they are indicators of impaired metabolism in ischemia (de Graaf, 2018), and also to measure microscopic anisotropy properties without interference due to macroscopic features of the tissue, via advanced dMRI sequences (Shemesh et al., 2014).

Functional MRI (fMRI) techniques such as blood oxygen-level dependent (BOLD) are useful to study functional recovery and plasticity in populations. Furthermore, it has been reported that sensorimotor function was in some focal stroke studies accompanied by contralesional activation (Dijkhuizen et al., 2001) up until a subacute phase, and perilesional cortical areas recruitment (Dijkhuizen et al., 2003).

To enable a higher sensitivity towards salvageable tissue, multimodal MRI techniques have been also approached. During the first hours post infarct onset, the region defined on the diffusion-weighted image appears smaller than the area appearing aberrant on the CBF maps. As time progresses this small area tends to expand and reach a point where it matches the area defined perfusion-weighted images (PWI). Thus, the observed difference between PWI and DWI images is often referred to as “perfusion-diffusion mismatch”, a potential candidate for identifying the penumbral region. Given the fact that the correlation between the mentioned mismatch and the penumbra (usually defined by the metabolic status of the tissue) is still uncertain, this technique still has not reached a routine clinical practice state (Meng et al., 2004; Qian et al., 2016).

### 2.6.1 Diffusion-Weighted Imaging for Characterizing Stroke

Diffusion-weighted magnetic resonance imaging (diffusion MRI) has become a powerful means for the early detection of ischemic stroke since the 90s (Baird & Warach, 1998; Moseley, Cohen, et al., 1990). The influence of tissue microstructure on the diffusion properties of brain water molecules makes this technique sensitive to alterations in the microscale. When ischemia occurs, abnormal water diffusion can be noticed as it manifests hyperintensity in DWI (Figure 2.28). An important discovery was pursued by Moseley in 1990 based on a significant drop of water diffusion (sudden decrease in ADC) (by 30 to 50%) witnessed in a cat brain minutes after the occlusion of the middle cerebral artery (MCAO) (Moseley, Kucharczyk, et al., 1990). The origin of this signal alteration led to several questions within the research field as its interpretation is pathophysiologically inconclusive. Several hypotheses have been put forth for explaining these observations. For instance, the cellular swelling (associated with cytotoxic edema) caused by the water extra-intracellular influx caused by the loss of ion homeostasis, subsequent to the failure in the  $\text{Na}^+$ ,  $\text{K}^+$  -ATPase transmembrane pump (Hossmann, 2006). Due to this swelling, the hypothesis stands on a possible net decrease of ADC considering the water shift from the faster diffusing extracellular space to the intracellular space, slower diffusing. Despite these occurrences, the diffusion intra-extracellular rate differences, according to some studies, were not relevant enough for the observed ADC reduction magnitude (Chang et al., 1973; Colson et al., Mariette, & Cambert, 2005). One more hypothesis would be the influence of the neurite beading to be sufficient to account for the observed ADC decrease by restricting water mobility intracellularly along the neurite's length (Budde & Frank, 2010). Thus, cell swelling, and subsequent neurite beading are considered to be critical contributors, leading to the general agreement that microstructural alterations are associated with alterations in the diffusivity observed in the tissue.

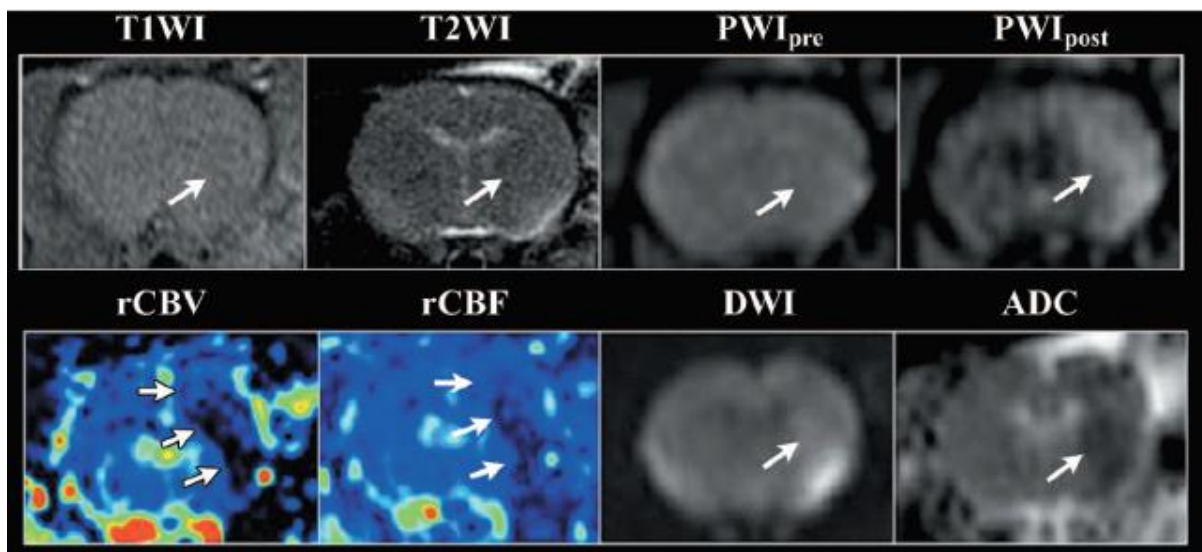


**Figure 2.28** – In vivo MR images, photograph of brain specimen (Brain), from rat in acute group (~1 hour post ischemic insult). Top row: While virtually invisible on T1-weighted (T1WI) MR image, T2-weighted (T2WI) MR image, and baseline echo-planar perfusion-weighted (PWI<sub>e</sub>) MR image (2000/40), pre ischemic lesion is well delineated on first-pass perfusion-weighted MR image (PWI<sub>t</sub>) as hyperintense area (arrow). Middle row: Impaired perfusion in ischemic lesion (arrows) is reflected on maps of relative cerebral blood flow (rCBF) and relative cerebral blood volume (rCBV). At this early time point, however, lesion (arrow) on diffusion-weighted MR image (DWI) and ADC map appears smaller than that on perfusion-weighted MR image (top row), which suggests presence of penumbra or rescuable region. Extracted from (F. Chen et al., 2004)

### **2.6.1.a Diffusion Tensor Imaging**

Since it has been pointed out that the diffusion anisotropy and average diffusion in white matter were time course dependent, the use of DTI for accurate diagnosis and prognosis of stroke should be highlighted (Sotak, 2002). DTI is capable of compiling information on both these types of processes, as well as demyelination and enables diffusion measurements in multiple directions, given the fact that water does not have a homogenous diffusion in all directions but a facilitated one instead (along the fibre tracts). This has been corroborated with the DTI changes which have been demonstrated to occur at the same time of remodelling and function recovery when histological studies were pursued (Granziera et al., 2007).

Changes in the white matter post ischemic lesion were registered in some studies with DTI. As ischemia progresses, FA decreases while ADC pseudo normalizes (W. A. Copen et al., 2001; Merino & Warach, 2010)- It was suggested that the decreases in FA post-stroke, no longer acutely, might be related to degeneration processes (cells and myelin breakdown) in regions with elevated coherence (van der Zijden et al., 2008). Since alterations in the microstructure of the brain tissue observed with this technique correlate with functional deficits, it is fair to assume it provides a functional recovery valuation (van Meer et al., 2012).

At a chronic phase, it is important to mention that the brain also remodels and generates new neurons and synaptic connections, crucial for the comprehension and improvement of patients outcome. Still, the mechanisms responsible for this reorganization are yet to be fully understood. DTI has been used to analyse structural integrity and connectivity restoration. Although its reliability in stroke imaging, dMRI in its conventional metrics is known to have its specificity compromised by partial volume effects contamination arising from free fluid resulting from vasogenic edema, for instance (González et al., 2011).

### **2.6.1.b Diffusion Kurtosis Imaging**

As a more advanced technique, DKI yields diffusional kurtosis, a metric added to the previously mentioned diffusion information (provided by DTI). This complementary information allows for a better characterization of tissue microstructure, since it contemplates all non-Gaussian effects occurring within the ischemic milieu. It has been reported that kurtosis maps show distinct lesion heterogeneity, which is not apparent on ADC maps, and present higher absolute percent change when compared to complementary diffusion metrics from conventional diffusion studies (Hui et al., 2012). Moreover, Hui et al. suggested that ischemia preferentially changes the intra-axonal environment, corroborating with the beading hypothesis when trying to understand the prompt ADC decrease after ischemic onset (Hui et al., 2012).

Reported results by Cheung et al. indicate that that DKI is more sensitive than DTI when detecting changes concerning the brain's microstructure also at a chronic stage post stroke, and that perilesional regions displayed relevant changes in kurtosis when comparing FA or mean diffusivity (MD) (Cheung et al., 2009).

Therefore, increased values in mean kurtosis until a subacute stage indicate a more complex and heterogeneous water microenvironment within the ischemic lesion (Jensen et al., 2005)(Jensen & Helpert, 2010), and has been suggested to be associated to higher reactive astrogliosis (Zhuo et al., 2012). Additionally, Rudrapatna et al. found that DKI could perceive structural tissue alterations and sensitively detect angiogenesis and functional reconstruction in the surrounding ischemic areas post stroke (Rudrapatna et al., 2014).



Despite being more sensitive than DTI and a promising biomarker of tissue heterogeneity, DKI still does not provide specific measures since it conflates all kurtosis sources, hampering the distinction between each source's influence on the ischemic tissue. Particularly, since DKI cannot decouple the negative kurtosis effects of tissue interacting water molecules from the positive kurtosis effects of compartment's diffusion variance, the relationship between non-Gaussian effects and tissue properties is hard to establish (Jensen et al., 2005).

## **2.7 Thesis objectives**

In order to tackle the lack of specificity which conventional DKI cannot resolve in brain ischemia and enhance sensitivity towards ischemic tissue, CTI stands as a potential methodology to satisfy these shortcomings needs. Hence, given the potentiality and versatility of the method in resolving kurtosis sources *ex vivo* and *in vivo*, the aim of this project relies on its application on a photochemical model of ischemic stroke in mice. The aim is to assess, with this advanced methodology, microscopic dMRI dynamics occurring at an early stage post ischemic insult in order to infer which kurtosis sources are more specific and sensitive to the underlying pathological events. To accomplish this, an *ex vivo* set of experiments was pursued, along with a further *in vivo* corroborative attempt.



### 3. Materials and Methods

#### 3.1. Photothrombotic Stroke Model

A photothrombotic Rose Bengal stroke model was used to induce a focal infarction in the barrel cortex of mice through photo-activation of Rose Bengal dye, previously delivered intravenously. All animal experiments were preapproved by the competent institutional and national authorities and carried out according to European Directive 2010/63.

Rodent models have played important roles in investigating disease in general and ischemia in particular. This study focused on the photothrombotic model of ischemia both *ex vivo* and *in vivo*.

##### 3.1.1. Rose Bengal Solution Preparation and Pre-surgery Protocol

In order for the photothrombotic ischemic infarct to be induced, equipment for surgery procedures, illumination and isoflurane anaesthesia were required, as well as materials for the Rose Bengal solution preparation. Prior to surgery, Rose Bengal sodium salt (95%, 330000-5G, Sigma-Aldrich, Darmstadt, Germany) was weighted, transferred into a 1.5 ml Eppendorf and dissolved in sterile saline until a final concentration of 15 mg/ml was reached. The solution was then mixed with a vortex and the recipient was covered *a posteriori* with aluminium foil to protect the solution from light. Hereinafter, the blend was filtrated through a 0.2  $\mu\text{m}$  sterile filter (15181499, Fisherbrand, Fisher Scientific, Lisbon, Portugal), directly at a 1 ml syringe (15489199, Terumo, Fisher Scientific, Lisbon, Portugal) connected to the filter. The syringe was then adapted to a 30 G needle (15391557, Terumo, Fisher Scientific, Lisbon, Portugal) and kept covered in aluminium foil at room temperature. In order to relieve pain and reduce inflammation, a  $\sim 100\ \mu\text{l}$  solution of Meloxicam (Nonsteroidal anti-inflammatory drug (NSAID)) was delivered subcutaneously with a 1 ml syringe connected to a 26 G needle (15301557, Terumo, Fisher Scientific, Lisbon, Portugal) 30 minutes prior to the surgery onset for pre-emptive analgesia and post-operatively every 24 hours for 3 days. All surgical instruments were autoclaved, and the surgical area was sanitized before initiating the surgery. To minimize the risk of contamination, the area where the animal was prepared was apart from the surgical field.

The light output power, aimed at reaching the surface of the skull for further irradiation, was measured via a handheld power meter console (PMD100D, Thorlabs, United States of America), reaching a colour temperature of 3200K and beam light intensity of  $10\ \text{W}/\text{cm}^2$ .

##### 3.1.2. Animal Preparation

Adult 11-week-old male C57BL/6J mice ( $N = 11$ ) were used in these experiments, weighing from 24.3 to 29.2 g. The animals were grown with a 12 h /12 h light/dark cycle with *ad libitum* access to food and water and kept in a temperature-controlled room before and right after surgery.

For the anaesthesia induction, the animal was placed in a transparent custom-built plastic anesthetizing container, or induction chamber (941443, VetEquip, USA) (Figure 3.1, left), on top of an electrical heating pad, to prevent body temperature drops and thus hypothermic risk. Gas anaesthesia with a mixture of medical air and 4% isoflurane (Vetflurane, Virbac, France) was monitored and maintained by an isoflurane vaporizer (911103, VetEquip, USA) (Figure 3.1, right). Once its righting reflex – its ability to correct and maintain a stable posture – and any reaction to firm foot squeeze were lost, the mouse would be considered to be adequately anesthetized.

At this point the mouse was weighed using an analytical scale (Traveler TA1501, Ohaus, Switzerland) and carefully transferred to the surface pad on the stereotaxic frame, in prone position, having its head placed with its upper incisors secured with a mouth bite bar and a nose cone for continuous gas circulation. Ear bars (8229221722, KOPF Instruments, CA, USA) were then used for a safe and efficient head fixation (into external meatus) (Figure 3.2). The isoflurane concentration was reduced to 2.5 % and the rectal probe was inserted to guarantee monitoring of the body temperature at  $36.5 \pm 0.5$  °C and maintain it at physiological levels. Eye ointment (9852004, Vitaminoftalmina A, DAVI, Portugal) was applied in both eyes to prevent the corneas from drying. A hair trimmer (20635, Andis, USA) was utilized to remove fur from the scalp, which was further wiped to remove any loose fur.



**Figure 3.1** – (Left) Plastic anesthetizing container above electrical heating pad. (Right) Isoflurane vaporizer with controlled gas monitoring.

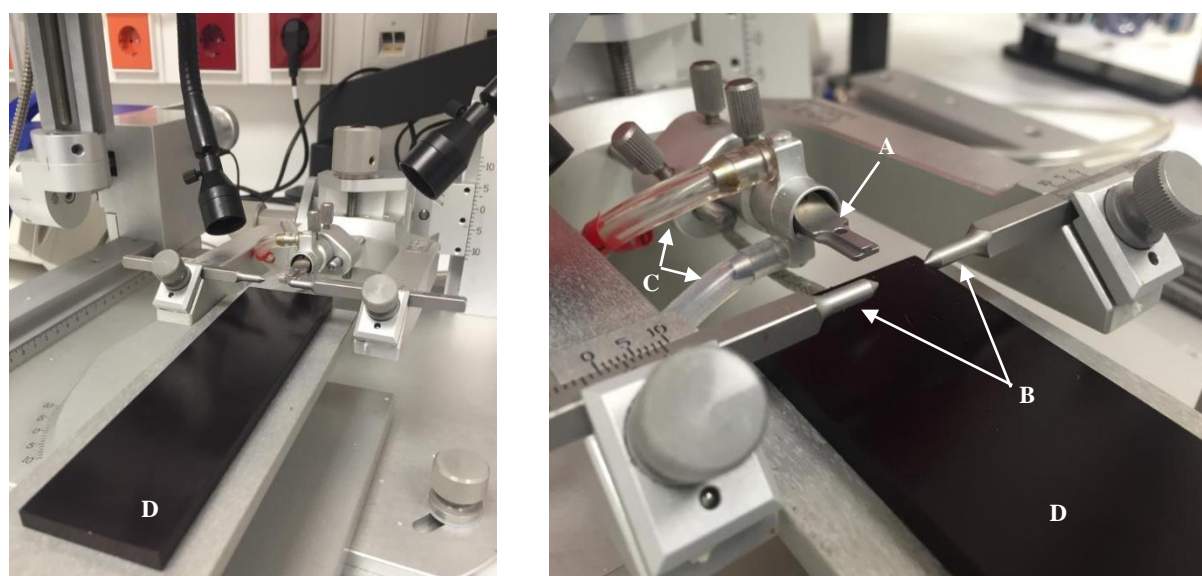


**Figure 3.2** – Stereotaxic frame set up with a (A) mouth bite bar, (B) ear bars for head fixation, (C) system of tubes for gas circulation and (D) body temperature pad.

### 3.1.3. Surgery and Target Area Illumination

Upon fur removal, the site was cleansed and disinfected with betadine (410087, Iodopovidone, Fisher Scientific, Portugal) using a sterile cotton swab, first applied on the centre of the incision site and then towards the margins with a circular motion. A 1-cm-long skin incision was performed with a scalpel (blade n.10, S2646-100EA, Sigma Aldrich, Lisbon, PT) along the midline starting from the eye level down to the neck. Skin retractors were applied in order to keep the skull exposed. After immersing another sterile cotton swab in 70% ethanol, the periosteum was slowly scrubbed and retracted. When the bregma and lambda were identifiable, a fibre optic light guide (8065812001, Alcon, USA) (Figure 3.3) – connected to a cold light source (Figure 3.3, left) – attached to the stereotactic frame holder (Figure 3.4) was positioned ~ 2 mm above the bregma to have a reference point when choosing the target coordinates. With a coordinate monitor, the fibre optic light guide tip was moved 3 mm posterior and 1.67 mm lateral to the bregma, covering an area of about 15 mm<sup>2</sup>, including the barrel cortex (Figure 3.2) (Franklin & Paxinos, 2019).



**Figure 3.3** – (Left) Cold light source with port adaptative to the (right) optic fibre guide.

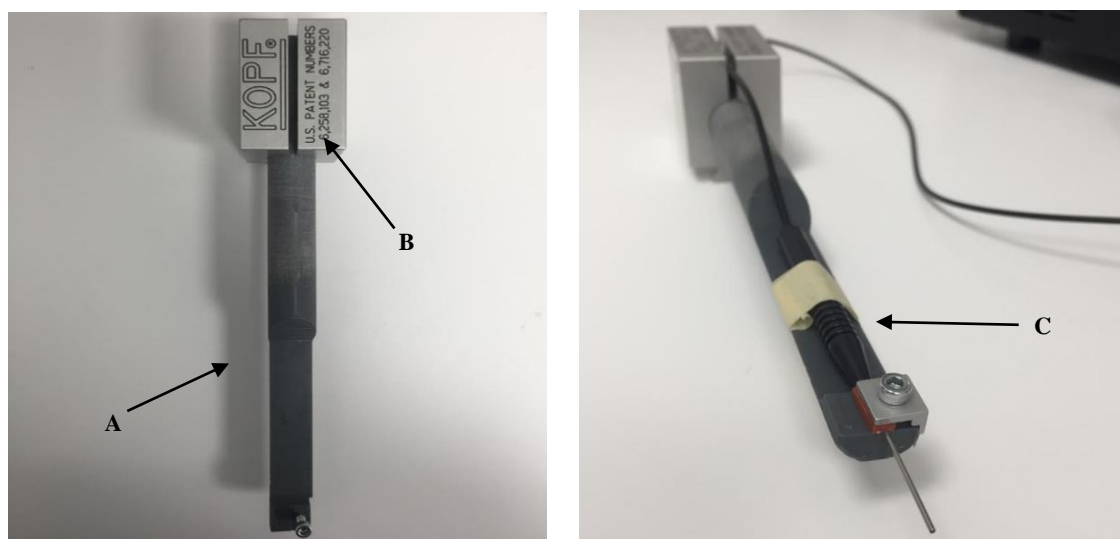


**Figure 3.4** – (A) and (B) Stereotaxic frame holder with (A) designed 3D printed in-house for possible and correct placing of the optic fibre guide (C).

The fibre optic light guide was then moved ~ 4 mm up the z-axis to enable the dye injection with a wider field of view. With the correct dose calculated (10 µl/g of body weight), the solution was delivered retro-orbitally at a slow pace and the Rose Bengal dye solution was instantly in the blood stream – confirmed by pink-coloured foot tips and tail veins. The optic fibre was immediately moved down until the tip of the fibre was less than 1 mm away from the cranium and the cold light source was instantly switched on, irradiating the target area for 15 minutes, for 6 of the animals (10 mW/mm<sup>2</sup>) (Figure 3.6). Illumination of the animal by any other light source was avoided. After this period of time, light exposure was interrupted. The skin retractors were then removed, and the wound was sutured with a reverse cutting needle and suture thread (W468H, PERMAHAND® Silk Suture, Ethicon, Johnson & Johnson Medical, Belgium). Betadine was applied on the surface of the sutured wound with a sterile cotton swab. The anaesthesia was stopped right after and the mouse was transferred from the stereotaxic frame on to a pre-warmed heating pad for a recovery without loss of temperature. A sham group (N = 5) underwent the same conditions except for the lesion-inducing illumination, yet the 15-minute interval post injection was respected.

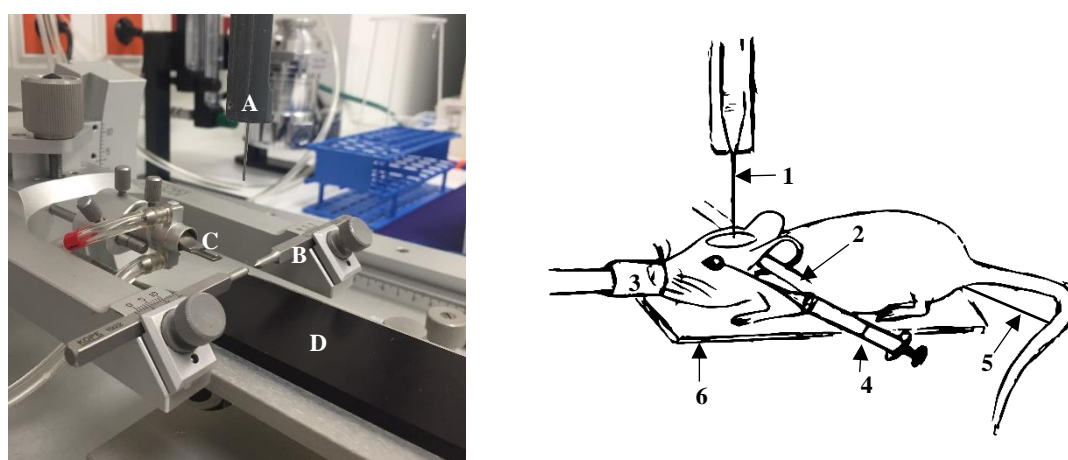


**Figure 3.5** – (Left) Surgical set-up before animal positioning. (A) Optic fibre light guide tip attached to stereotaxic holder for reference point and illumination step. (B) Ear bars for head fixation. (C) Bite bar attached to a nose cone for gas circulation. (D) heating temperature pad. (Right) Photochemical induction illustration. (1) Optic fibre light guide. (2) Ear bars. (3) Mouth cone for anaesthesia/gas circulation. (4) Rose Bengal dye retro-orbital injection. (5) Rectal temperature probe. (6) Heating temperature pad.

For a multi modal analgesia – considering the pre-operative Meloxicam analgesia, after the animal was allowed to recover from the surgery up to a point when it was already conscious and with its righting reflex, a 100 µl solution of Buprenorphine was delivered subcutaneously with a 1 ml syringe adapted to a 26 G needle. This allowed pain relief and fear-mediated distress reduction.

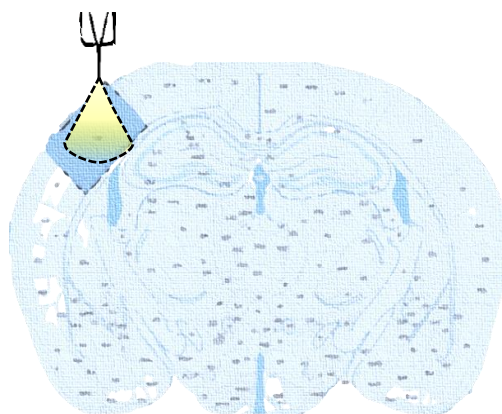


**Figure 3.6** – Coronal slice from anatomical map concerning the target cortical region (S1BF, selected in blue) for focal photothrombotic induction. Adapted from (Franklin & Paxinos, 2019).

### 3.1.4. Sample Preparation for *ex vivo* Experiments

Brains were extracted via transcardial perfusion with 4% Paraformaldehyde (PFA) from ten adult mice (N = 10, 5 from each group) at 3 h post the irradiation period. After extraction of the skull, the brains were immersed in a 4% PFA solution – immersion fixation – for 24 h and washed in a Phosphate-Buffered Saline solution afterwards, preserved in for at least 24 h. The specimens were subsequently placed in a 10-mm NMR tube filled with Fluorinert (F3556, Sigma Aldrich, Laborspirit Lisbon, Portugal) – a non-conductive, thermally and chemically stable fluid and hence an option for minimizing susceptibility artifacts in *ex vivo* MRI scanning –, secured with a stopper to prevent from floating. The tube was then sealed with paraffin film (Figure 3.7).

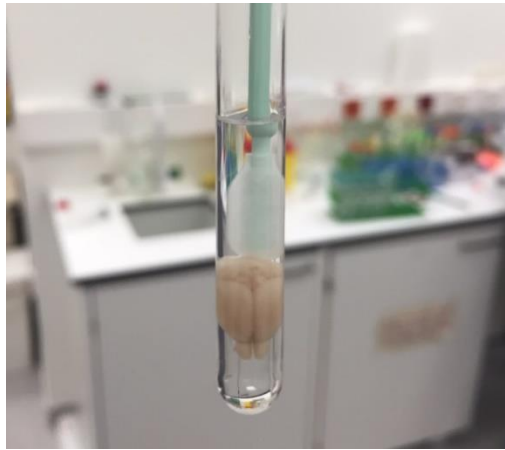


**Figure 3.7** – Mouse brain sample from control group immersed in Fluorinert inside a 10-mm NMR tube with a stopper to prevent from floating.

## 3.2 Histology

Histological analysis was encouraged and performed in one of the stroked *ex vivo* samples (stroke 4). 29 slices were obtained through Vibratome sectioning with a thickness of 0.04 mm and Mowiol containing 2.5 % 1,4 diazobicyclo-[2.2.2]-octane (DABCO, Sigma, D2522) was used as the mounting media. The brain sections were then fixed with 10% formalin and processed with hematoxylin–eosin (HE) and Nissl-Cresyl Violet staining for microscopy in order to have a perception of tissue damage and cell loss within the infarcted region, respectively. The histological staining was performed by the Champalimaud Histopathology Platform.

Histological images were acquired after scanning all slides on the ZEISS Axio Scan.Z1 (Zeiss, Germany) by the Champalimaud ABBE Platform - Advanced BioImaging and BioOptics Experimental Platform and processed via an image analysis software (FIJI, ImageJ).



### 3.3. dMRI Experiments

We have designed two MRI experiment series, namely, *ex vivo* (main) and *in vivo* (corroborating). First, *ex vivo* data were acquired from N=10 11-week-old male C57BL/6 mice brains after perfusion and brain extraction at 3 hours post light irradiation offset (stroke group and sham group, 5 samples per group). This allowed for the potential of CTI to be explored at an acute stage of focal ischemia without being constrained by acquisition time limitations or artifacts due to physiological noise. In order to confirm reproducibility, *in vivo* acquisitions were performed in N=2 11-week-old male C57BL/6J mice, one animal at 3 h post illumination offset and one animal which had not undergone surgery (Figure 3.8).

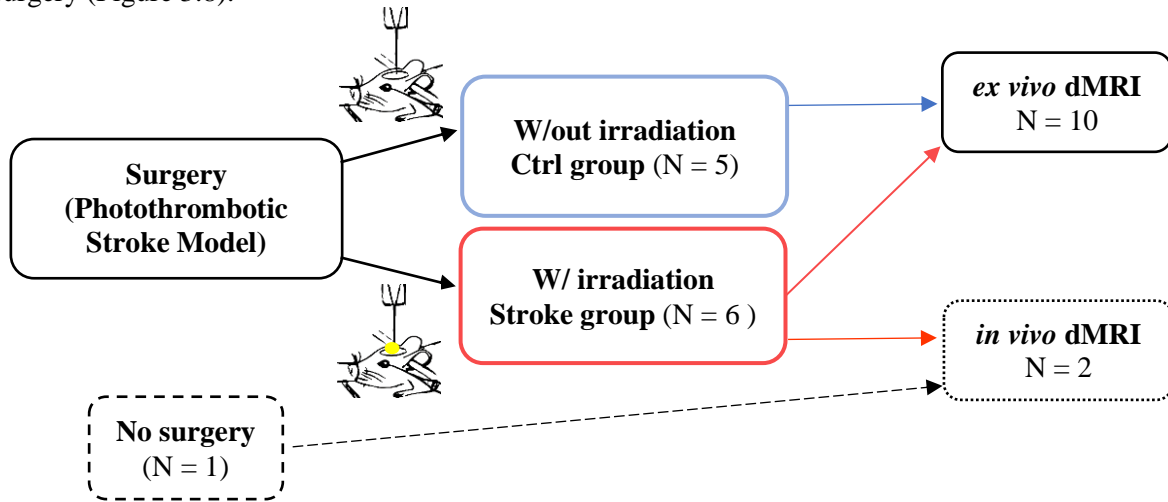


**Figure 3.8** – Study design representative scheme. A total of 11 mice underwent surgery, 10 of which were assigned to the *ex vivo* experiments and 1 of which was assigned to the corroborative *in vivo* study. In the *ex vivo* experiment, a group of 5 animals underwent photothrombotic ischemia induction, whereas the left 5 animals did not undergo irradiation, being therefore assigned to the sham *ex vivo* group. For the *in vivo* corroborative study, the mouse which underwent surgery was also irradiated for the stroke induction. A healthy animal was part of the *in vivo* imaging, for validation with previous studies.

#### 3.3.1 Ex vivo experiments

##### 3.3.1.a. MRI Protocol

All *ex vivo* MRI scans were performed on a 16.4 T Aeon Ascend Bruker scanner (Karlsruhe, Germany) equipped with an AVANCE IIIHD console and a Micro5 probe with gradient coils capable of producing up to 3000 mT/m in all directions and a birdcage RF volume coil, which provides a uniform spatial coverage throughout a large volume and whose configuration allows for a transverse RF field establishment. Imaging was performed with Paravision 6.0.1 (Bruker BioSpin MRI GmbH, Ettingen, Germany) and TopSpin 3.1.

Before placing the sample in the scanner, a 10 mm spinner was inserted on the sample NMR tube to assist the tube insertion and adjust the target height for the tube to be held inside the probe when scanning. For this aim, a trial was performed with a mock apparatus. Once inserted, the sample was maintained at 37°C due to the probe's variable temperature capability and it was allowed to acclimatize with the surroundings for at least 2 h prior to the beginning of diffusion MRI experiments. In order to guarantee that the brain was correctly oriented according to the x-y spatial plane, localizers (scout images) were acquired in three orthogonal planes, and the sample would be repositioned with the spinning option via TopSpin 3.1 in case the brain was tilted.

After the brain correct positioning, scan adjustments were executed (tuning of the coil to the relevant nucleus and matching of the impedance of the coil, i.e., the total effective resistance to alternating current, with that of the transmitter and receiver) to avoid sensitivity loss and get maximal energy to pass into the receiver from the transmitter.

In favour of shimming, i.e., correction for field inhomogeneities, a  $B_0$  map was also acquired covering the volume of the brain. Axial, sagittal and coronal T2-weighted images with high resolution and high SNR were acquired for anatomical reference and assessment of partial volume effects and stroke lesion size. These data were acquired using rapid acquisition with relaxation enhancement (RARE) sequences with the following parameters: TR = 4000 ms, TE = 50 ms, RARE factor (defined by the number of echoes which are distinctively phase-encoded) = 12, number of averages = 6. Concerning the axial images, the Field of View (FOV) was  $18 \times 18 \text{ mm}^2$ , and the matrix size was  $240 \times 132$ , resulting in an in-plane voxel resolution of  $75 \times 76 \mu\text{m}^2$ . For the sagittal images, FOV was set to  $18 \times 9 \text{ mm}^2$ , matrix size to  $240 \times 120$ , and subsequently in-plane voxel resolution resulted in  $75 \times 75 \mu\text{m}^2$  (sagittal). Both axial and sagittal acquisitions sampled the total of 33 slices with a thickness of 0.3 mm. For the coronal images, FOV was established as  $10.5 \times 10.5 \text{ mm}^2$ , the matrix size as  $140 \times 140$ , hence an in-plane voxel resolution of  $75 \times 75 \mu\text{m}^2$ , for 72 slices 0.225 mm thick.

Double diffusion encoding data were subsequently acquired for 25 coronal slices using an in house written EPI-based DDE pulse sequence. The diffusion encoding gradient pulse separation  $\Delta$  and mixing time  $\tau_m$  were set to 10 ms, and the pulsed gradient duration  $\delta$  was set to 1.5 ms. Acquisitions were repeated for five  $q_1$ - $q_2$  magnitude combinations (1498 - 0, 1059.2 - 1059.2, 1059.2 - 0, 749.0 - 749.0 and 749.0 - 0 mT/m) in which equal magnitude  $q_1$ - $q_2$  combinations were repeated for 135 parallel and perpendicular directions, reflecting the necessary diffusion gradient intensities for the requirements of the CTI protocol to be fulfilled (for the tensors associated with the fourth cumulant to be fitted). In this study, the selected gradient intensities were 3000, 1500 or 750  $\text{mm/s}^2$ . In addition, twenty acquisitions without any diffusion-weighted sensitization (zero b-value) were performed to guarantee a high ratio between the number of non-diffusion and diffusion-weighted acquisitions. For all experiments, the following parameters were used: TR/TE = 3000/49 ms, Field of View =  $11 \times 11 \text{ mm}^2$ , matrix size  $78 \times 78$ , resulting in an in-plane voxel resolution of  $141 \times 141 \mu\text{m}^2$ , slice thickness = 0.5 mm, number of segments = 2, number of averages = 8. For every  $b_{\max}$  value, the total acquisition time was approximately 1 h and 57 min.

The acquisitions were repeated due to consistent Gibbs ringing artifacts in raw data in every slice, further presented in Chapter 4. In the second round of acquisitions the receiver amplifier gain parameter was manually set to 101 dB in every experiment in order to guarantee its consistency.

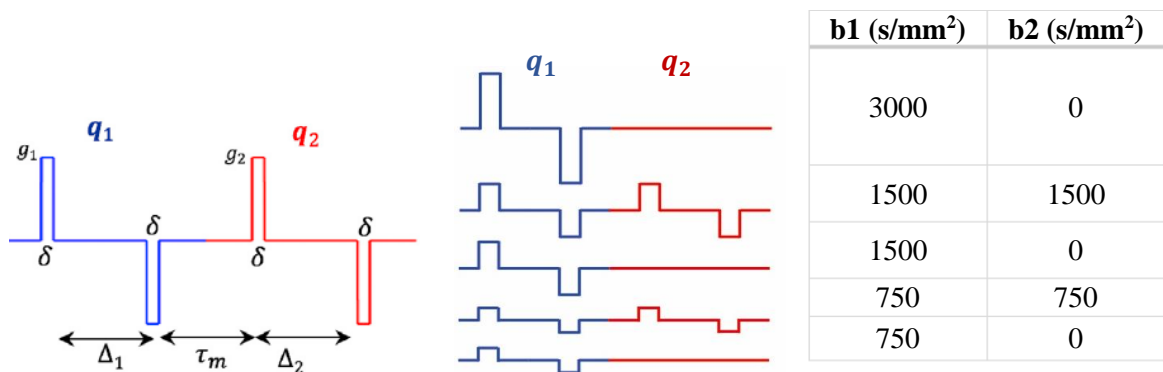


**Figure 3.9** – Acquisition parameters. (Left) Parameters of a DDE pulse sequence, in which  $\Delta_1$  and  $\Delta_2$  are the diffusion times,  $\delta$  is the diffusion gradient pulse duration,  $g_1$  and  $g_2$  are the gradient amplitudes, and  $t_m$  is the mixing time. Extracted from (Henriques et al., 2020). (Centre and Right) The five gradient DDE combinations and respective gradient strengths combinations, as well as two more combinations with  $b_1 = 1500 \text{ s/mm}^2$  and  $b_2 = 1500 \text{ s/mm}^2$ ; and  $b_1 = 750 \text{ s/mm}^2$  and  $b_2 = 750 \text{ s/mm}^2$ , but perpendicular  $q$ -vector directions) were used for the ex vivo CTI protocol, acquired for 135 directions.

### 3.3.2 *In vivo* experiments

#### 3.3.2.a. *Animal Preparation*

Adult 11-week-old male C57BL/6J male mice ( $N = 2$ ) were used in these experiments, weighing 24.6 g and 28.9 g. The animals were grown with a 12 h /12 h light/dark cycle with *ad libitum* access to food and water and kept in a temperature-controlled room before and after scanning.

For the anaesthesia induction, the animal was placed in a transparent custom-built plastic anesthetizing container, on top of an electrical heating pad, to prevent body temperature drops and thus reduce hypothermic risk. Gas anaesthesia with a mixture of medical air and 4% isoflurane (Vetflurane, Virbac, France) was monitored and maintained by an isoflurane vaporizer (VetEquip, United States of America).

Once the animal was adequately anesthetized (similarly as in section 3.1.2, prior to surgery), the isoflurane concentration was regulated and reduced to 2.5%. The mouse was then weighed using an analytical scale (Traveler TA1501, Ohaus, Switzerland) and transferred to the animal bed, prone positioned above a heated water pad – in order for the mouse body temperature not to oscillate during the experiments –, having its head placed with its upper incisors held on to a mouth bite bar. Oxygen concentrations were kept between 27% and 28%, monitored by a portable oxygen monitor (MX300-I, Viamed, United Kingdom). Ear bars were then used for a safe and efficient head fixation (into external meatus) and eye ointment (Bepanthen Eye Drops, Bepanthen, Germany) was applied to prevent the corneas from drying. A rectal temperature probe and a respiration sensor (Model 1030 Monitoring Gating System, SAI, United States of America) were placed for real-time monitoring of these physiological measurements, to guarantee the animal's welfare and immobilization. Considering the water molecules sensitivity towards temperature alterations, the waterbed temperature was cautiously monitored and controlled to avoid oscillations. Respiration rates were also monitored and maintained at physiological levels throughout dMRI scanning.

#### 3.3.2.b. *MRI Protocol*

The *in vivo* MRI data were acquired on a 9.4 T horizontal MRI scanner (BioSpec 94/20 USR, Bruker BioSpin, Germany) equipped a gradient system able to produce up to 660 mT/m in every direction, an 86 mm quadrature coil for transmission and a 4-element array surface cryocoil for reception. Imaging was executed with Paravision 6.0.1 (Bruker BioSpin MRI GmbH, Ettingen, Germany).

Once the mouse was sedated, the bed where the animal was placed was inserted in the scanner bore. To guarantee that the brain was well positioned while scanning, localizers were acquired in three orthogonal planes, and the mouse would be repositioned if the brain was tilted, according to the orientation of the tilt. After the brain correct positioning, scan adjustments were executed (tuning of the coil to the relevant nucleus and matching of the impedance, i.e., the total effective resistance to alternating current, of the coil with that of the transmitter and receiver) to avoid sensitivity loss and get maximal energy to pass into the receiver from the transmitter. In favour of shimming, i.e., correction for field inhomogeneities, a  $B_0$  map was also acquired covering the volume of the brain.

Sagittal  $T_2$ -weighted images were acquired for anatomical reference using a RARE pulse sequence with the following parameters: TR = 2000 ms, TE = 36 ms, RARE factor = 8, number of averages = 8. The field of view was  $24 \times 16.1 \text{ mm}^2$ , the matrix size was  $256 \times 256$ , resulting in an in-plane voxel resolution of  $150 \times 150 \text{ }\mu\text{m}^2$ . The slice thickness was 0.5 mm, and 21 slices were sampled.



Following an optimized protocol when compared to the *ex vivo* experiment, double diffusion encoding data were acquired for 5 coronal slices using an in house written EPI-based DDE pulse sequence. The diffusion encoding gradient pulse separation  $\Delta$  and mixing time  $\tau_m$  were set to 10 ms, and the pulsed gradient duration  $\delta$  was set to 4 ms. Acquisitions were repeated for five  $q_1$ - $q_2$  magnitude combinations (518.79 - 0, 366.84 – 366.84.2, 366.84 - 0, 259.4 – 259.4 and 259.4 - 0 mT/m), following equal combinations of directions as in the *ex vivo* experiments (Figure 3.10). In addition, twenty acquisitions without any diffusion-weighted sensitization ( $b$ -value = 0) were performed. For all experiments, the following parameters were used: TR/TE = 2800/44.5 ms, FOV =  $12 \times 12$  mm<sup>2</sup>, matrix size  $78 \times 78$ , resulting in an in-plane voxel resolution of  $181 \times 181$   $\mu$ m<sup>2</sup>, slice thickness = 0.85 mm, number of segments = 1, number of averages = 1 and partial Fourier acceleration of 1.25. For every  $b_{max}$  value, the total acquisition time was approximately 7 min.

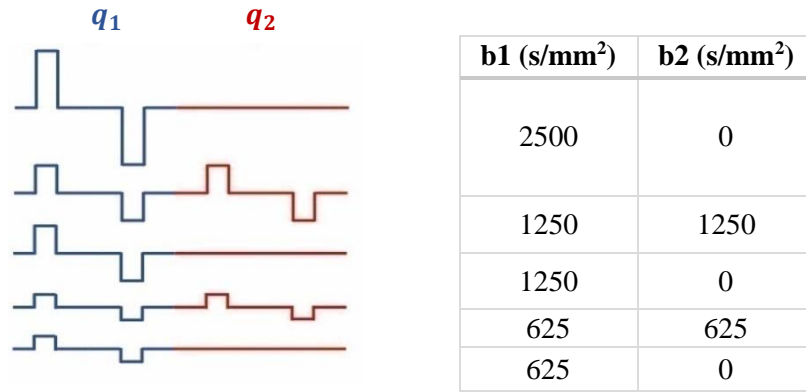


**Figure 3.10**– The 5 gradient DDE combinations (left) and respective gradient strengths combinations (right) used for the *in vivo* CTI protocol, acquired for 135 directions. Two more combinations (with  $b_1 = 1250$  s/mm<sup>2</sup> and  $b_2 = 1250$  s/mm<sup>2</sup>; and  $b_1 = 625$  s/mm<sup>2</sup> and  $b_2 = 625$  s/mm<sup>2</sup>, but perpendicular  $q$ -vector directions) were used.

### 3.2.3 Data Analysis

Before starting the diffusion data analysis, masks for all slice delineation were manually drawn on Matlab R2018b, as shown in Figure 3.11.

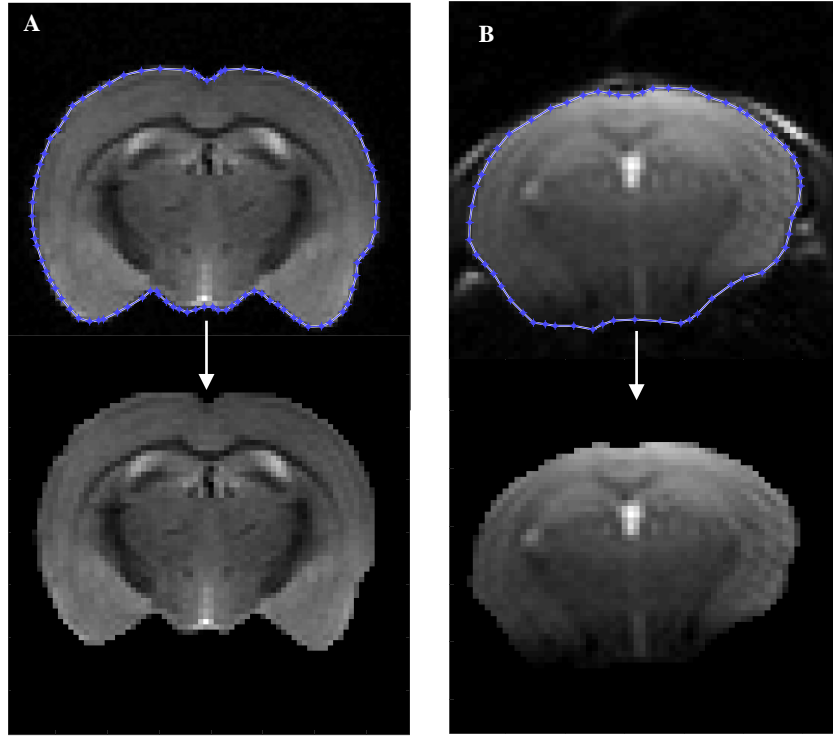


**Figure 3.11** – Manually drawn masks of representative control brains. (A) *ex vivo* and (B) *in vivo*. Since the *ex vivo* samples were immersed in Fluorinert, a proton-free substance, no signal in the background was detected when drawing the mask.

#### 3.2.3. a. Image Correction

All diffusion-weighted images were denoised using the Marchenko-Pastur Principal Component Analysis (PCA) denoising algorithm (Veraart et al., 2016), which harnesses the redundancy in the data using PCA and Random Matrix Theory and determines the noise level based on the Marchenko-Pastur distribution, aiming at an efficient and objective denoising of the data. Figure 3.12 shows the raw data prior and post PCA denoising. All datasets were then corrected for Gibbs ringing artifact (shown in Figure 3.13) (Henriques, 2018; Kellner et al., 2016) in Python (Dipy, version 1.0, (Garyfallidis et al., 2014)) which suppresses the Gibbs oscillations effects based on a total local variation (TV) analysis. In this case, TV was accessed with three neighbours and hence the artefact correction was done based on three adjacent points for each voxel (Figure 3.13).

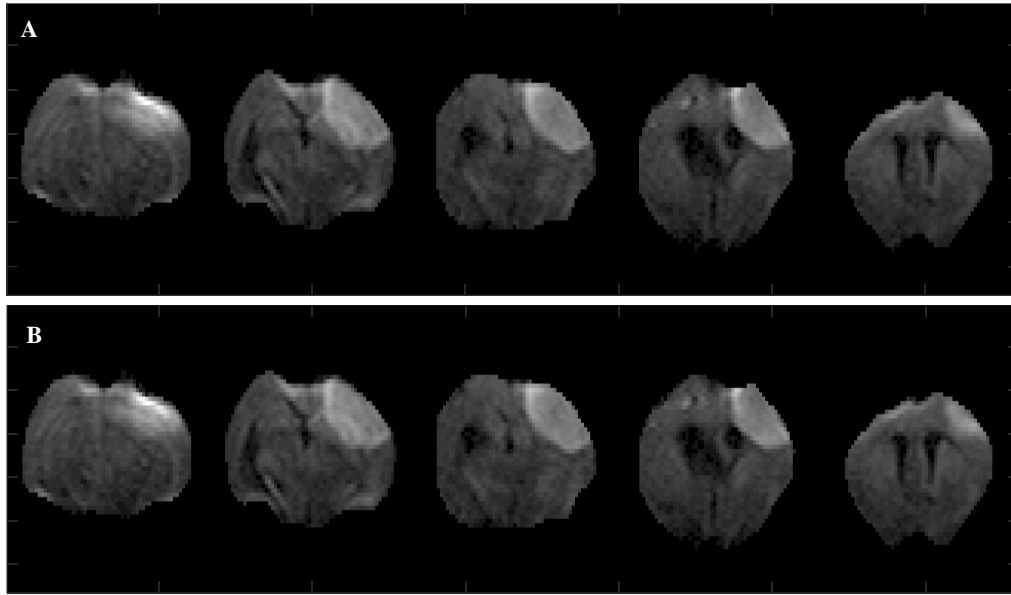


**Figure 3.12** – Representative dataset (in vivo stroked animal) prior to PCA denoising (A) and after PCA denoising (B). No considerable impact was noticed.

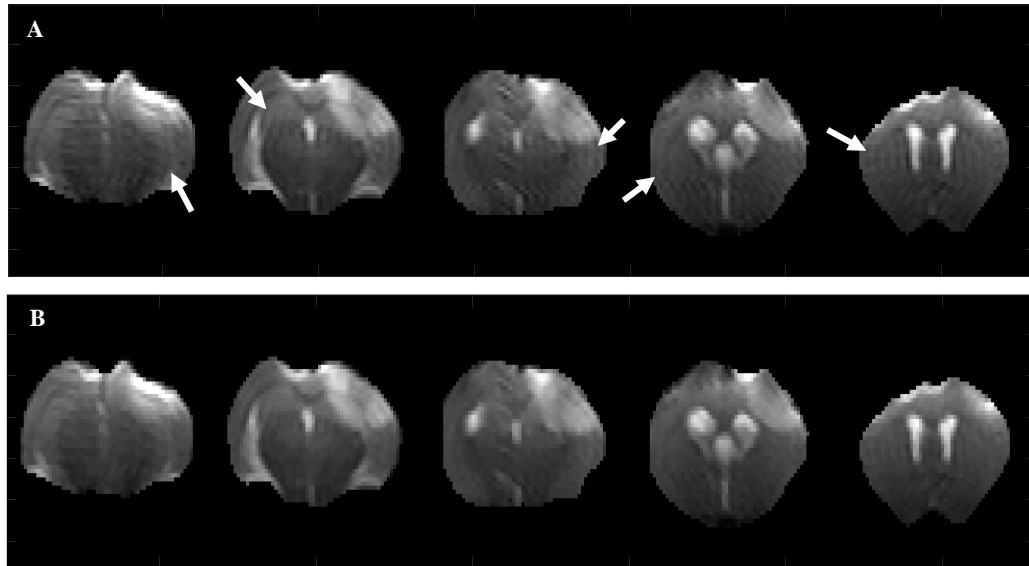


**Figure 3.13** – T2-weighted images from a mouse from the stroke group before Gibbs ringing correction (A) and after Gibbs ringing correction (B). White arrows are pointing towards the Gibbs ringing artifacts.

### 3.2.3. b. Image Registration

All diffusion-weighted datasets were first pre-processed by realigning the data via a sub-pixel registration method (Guizar-Sicairos, Thurman, & Fienup, 2008) in which each set of data for every total diffusion b-value would be realigned to a counter defined dataset with similar DDE gradient pattern combinations. CTI was then directly fitted to the data (normalized to b0 images – images without diffusion gradient weighting) using a linear-least squares fitting procedure, implemented in-house. CTI estimates were achieved by a fit gathering the diffusion datasets from all acquired b-values.

### 3.2.3. c. ROI Analysis

Region of Interest (ROI) analysis was performed by manual selection of the most important areas for every diffusion data slice in both hemispheres in all animals, containing the total lesion and counterpart region in the opposite hemisphere, and subsequent threshold selection of gray and white matter within the manually selected ROIs. To assess which metrics were more sensitive to stroke, regions were manually drawn for each considered metric. Therefore, white matter (WM) regions in the ipsilesional hemisphere with a differing contrast from its counterpart hemisphere were selected. The same method was applied for gray matter (GM) regions and at last a whole ROI containing both WM and GM was delimited. Thus, the sensitivity to stroke was evaluated by assessing the total number of voxels in MD, FA,  $K_T$ ,  $K_{aniso}$ ,  $K_{iso}$  and  $K_{intra}$  maps of the lesioned hemisphere. For each brain sample which had previously undergone ischemic insult and considering the previously selected ROI covering the total lesion area in the MD measure map, a ROI identical in size and symmetrical in location to the former was manually drawn. Identical regions were then delineated on the sham group hemispheres. Within these primarily drawn ROIs, GM and WM regions were selected according to threshold values pre-established for FA and MD measures (Table 3.1 and Figure 3.14). This set of ROIs was essential for a consistent comparison of diffusion measures at a global perspective of the lesion as well as a comparison along regions with different microstructural properties, between hemispheres and groups of animals, thus enabling a specificity analysis.

**Table 3.1** – Manually selected values for ROI thresholding of white matter (WM) and gray matter (GM) for both stroke and control groups of animals.

Groups		MD	FA
<b>Stroke</b>	WM	< 0.55	> 0.45
	GM	> 0.55	< 0.45
<b>Control</b>	WM	< 0.6	> 0.6
	GM	> 0.6	< 0.6

A statistical analysis was then conducted to assess whether the differences between mean values in each ROI for each metric averaged across mice (from each group) were significant through a one-way ANOVA test, and a Bonferroni correction was performed for multiple comparisons across the different diffusion metrics.

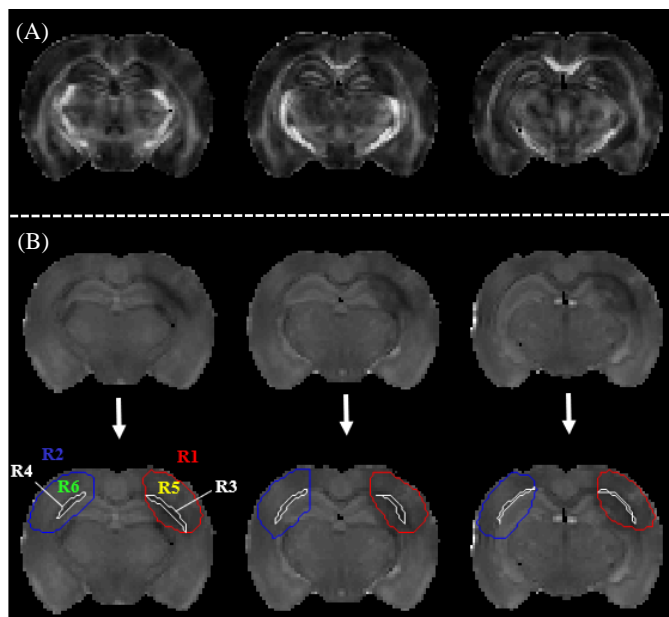


**Figure 3.14** – Three representative slices from the fractional anisotropy (FA) (A) and derived mean diffusivity (MD) (B) map of an extracted brain from the stroke group for lesion delineation. The ipsilesional and contralesional total ROIs were manually drawn and are contoured in red and blue, respectively. Regions in white account for the white matter (WM) ROIs, thresholded for both ipsi and contralesional hemispheres, and counter control animal group hemispheres according to FA and MD values (Table 3.1). R1 stands for the ipsilesional total lesion (WM + GM), R2 is the contralesional hemisphere area accounting for both gray and white matter; R3 and R4 are the white matter ROIs related to the lesioned region and its opposite hemisphere counterpart, respectively; R5 and R6 are the GM delimited ROIs in the stroke region and in the contralesional hemisphere region, respectively.

## 4. Results

In this section, the main and more relevant results from the conducted experiments are presented, as well the corresponding statistical analysis results from the *ex vivo* experiments.

### 4.1. *Ex vivo*

#### 4.1.1. Photothrombotic Stroke

The photothrombotic stroke model reproducibly induced well-delimited infarct cores in the targeted barrel cortex on the left hemisphere in all animals from the stroke group (five *ex vivo* brain samples (Figure 4.1) and one *in vivo* mouse brain).

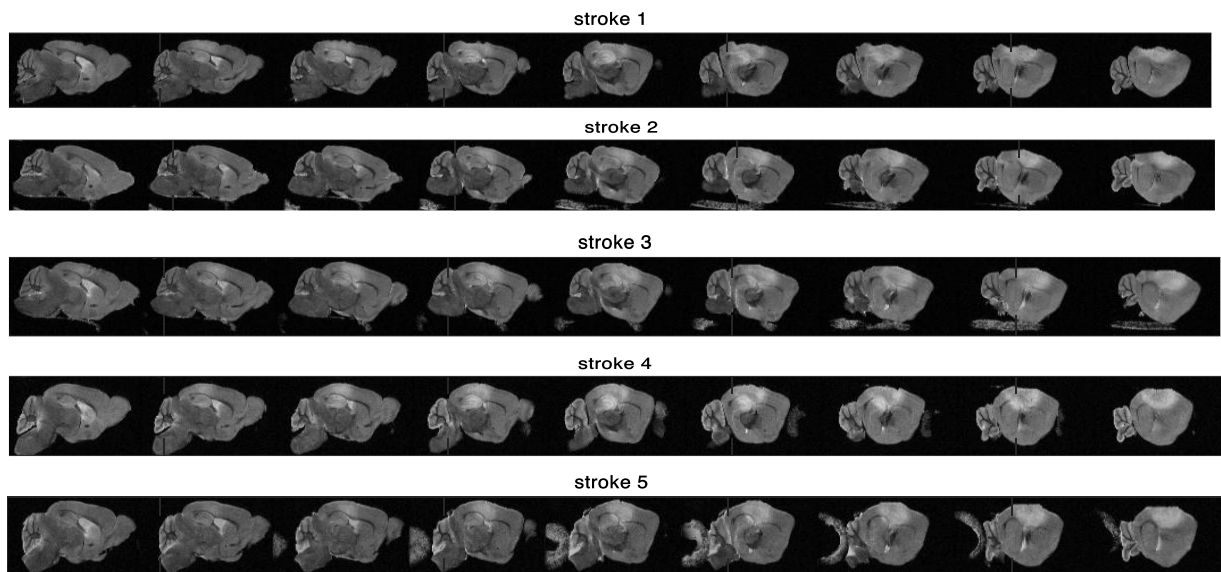


**Figure 4.1** – Raw T2-weighted images from all *ex vivo* brains 3 h post stroke onset for reproducibility analysis. 9 representative sagittal slices are presented from right to left. The ischemic territory is delimited by the hyperintense voxels (brighter subcortical regions in the somatosensory cortex).

It was possible clearly identify the infarcted region in the left hemisphere of all mice through the structural MRI images acquired before the dMRI acquisitions, as shown in T2-weighted images from one representative mouse brain *ex vivo* after ischemia, accounting for coronal, axial and sagittal slices in Figures 4.2, 4.3 and 4.4, respectively.

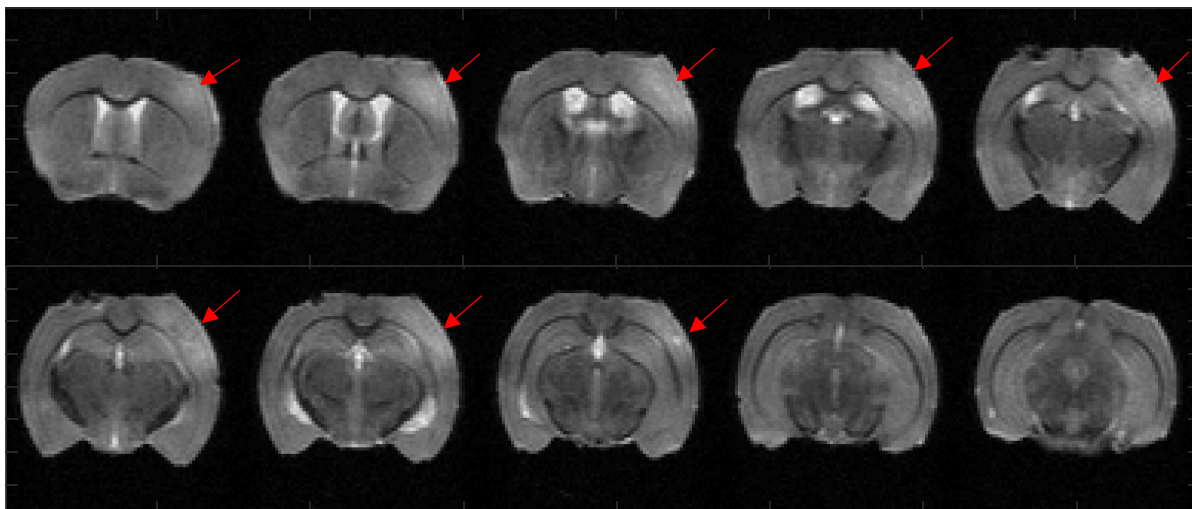


**Figure 4.2** – Raw T2-weighted images from one representative extracted brain from the stroke group. Representative coronal slices are presented from rostral to caudal direction (ex vivo). Red arrows point towards the stroke lesion.

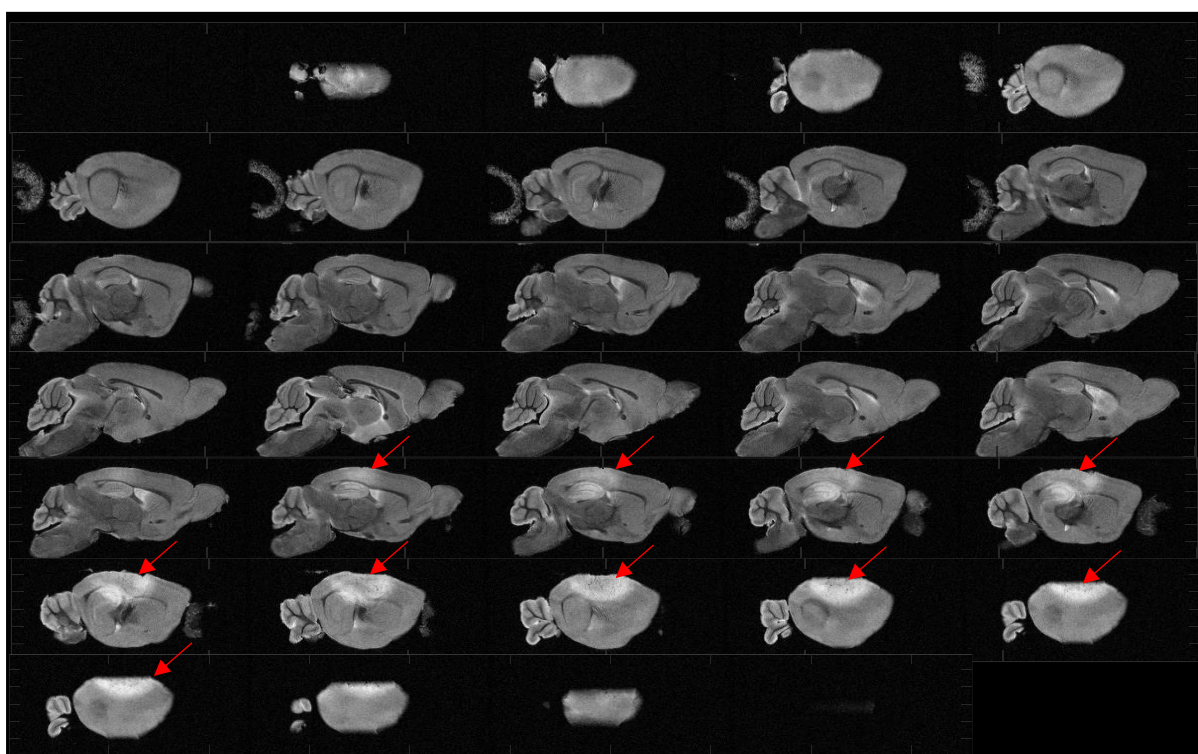


**Figure 4.3** – Raw T2-weighted sagittal images from one representative extracted brain from the stroke group. Representative sagittal slices are presented from right to left direction (ex vivo). Red arrows point towards the stroke lesion.



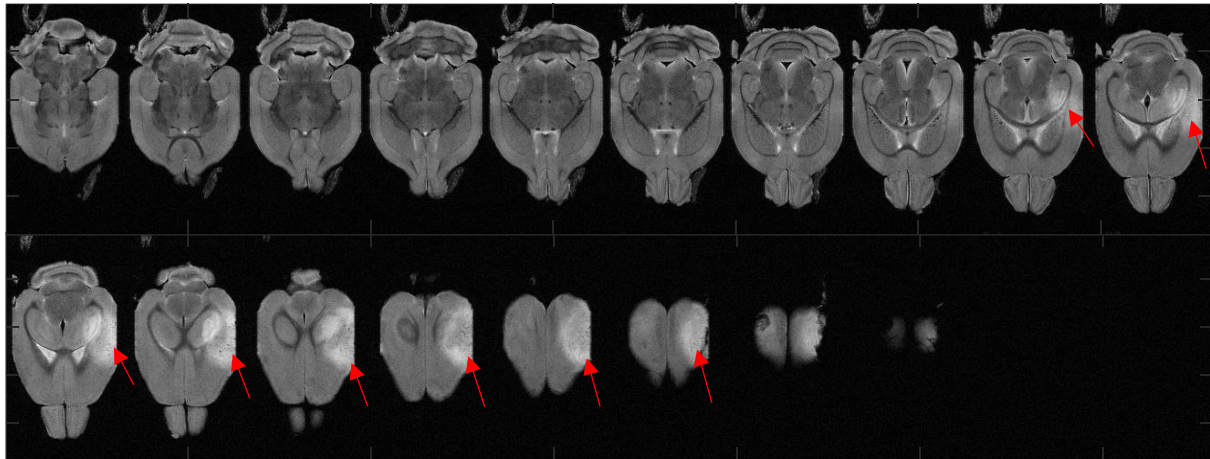


**Figure 4.4** – Raw RARE images from one representative extracted brain from the stroke group. Representative axial slices are shown from ventral to dorsal direction. Red arrows point towards the lesion.

Figure 4.5 shows representative T2-weighted images from one representative control brain, i.e., from an animal which underwent surgery but was not irradiated (SNR = 20.4). These images do not show any abnormalities, e.g., hyperintensity, as expected, when compared to the brain slices from the stroke group representative brain in Figure 4.2.

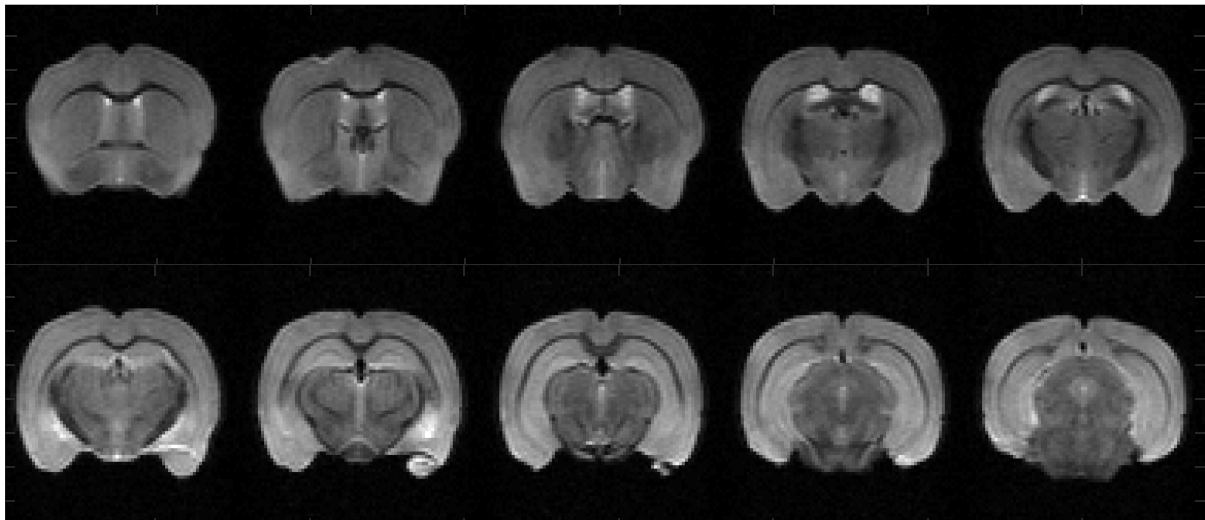


**Figure 4.5** – Raw T2-weighted images from one representative extracted brain from the control group. Representative coronal slices are presented from rostral to caudal direction (*ex vivo*).

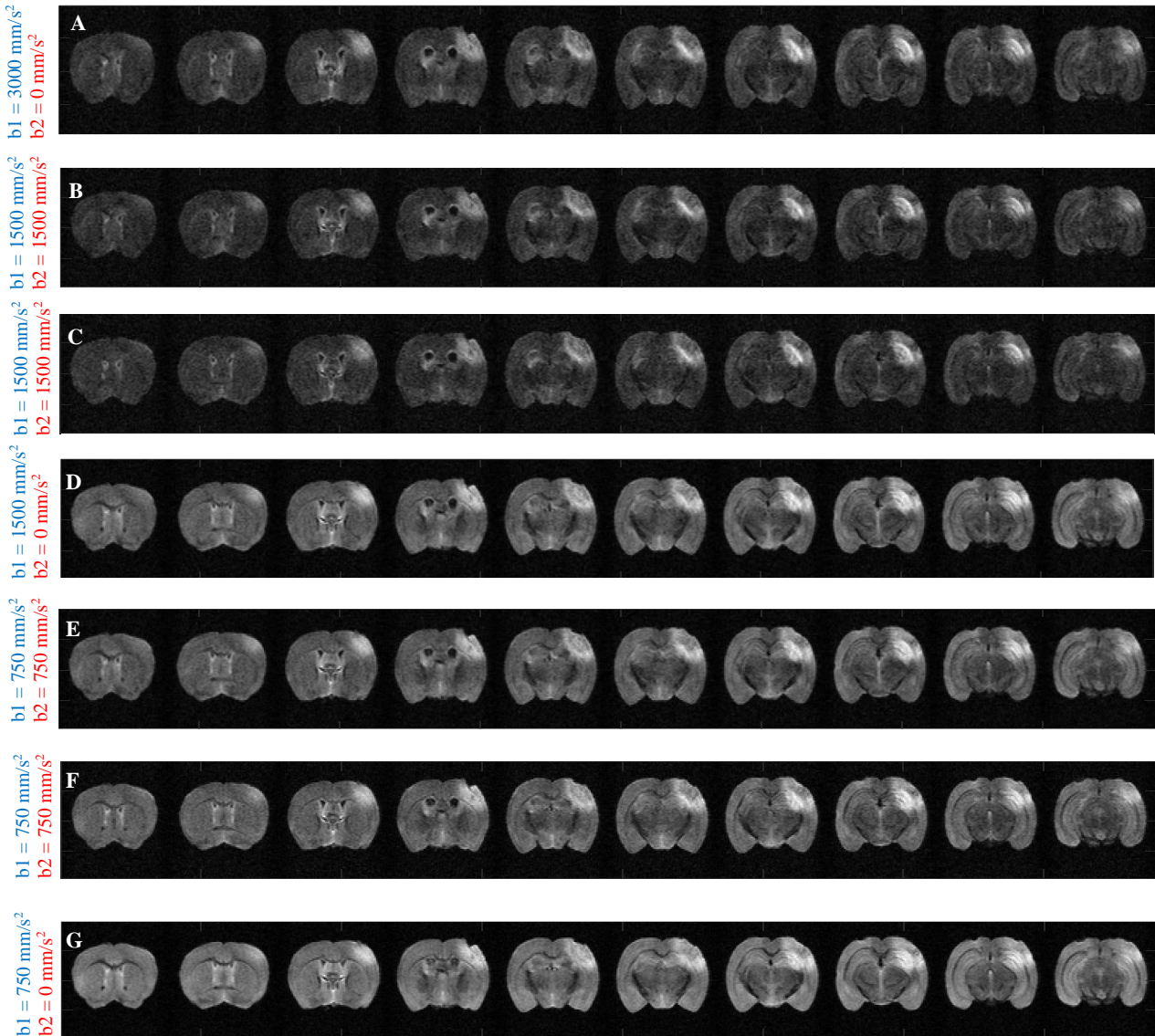
The MRI infarct volumes were calculated by the number of voxels within the designated masks (according to the MD ROIs previously drawn, presented in Figure 3.13) multiplied by the volume of each voxel and resulted in an average volume of  $21.81 \pm 5.14 \text{ mm}^3$  (mean  $\pm$  standard deviation of infarct volume across brains). Table 4.1 presents all resulting infarct volumes in all *ex vivo* brains from the stroke group.

**Table 4.1** – Photothrombotic infarct volumes from extracted *ex vivo* brains 3 h post ischemic onset.

<i>Stroke</i>	<i>Infarct volume /mm<sup>3</sup></i>
<b>1</b>	23.23
<b>2</b>	13.09
<b>3</b>	24.64
<b>4</b>	26.23
<b>5</b>	21.90

#### 4.1.2. dMRI Experiments

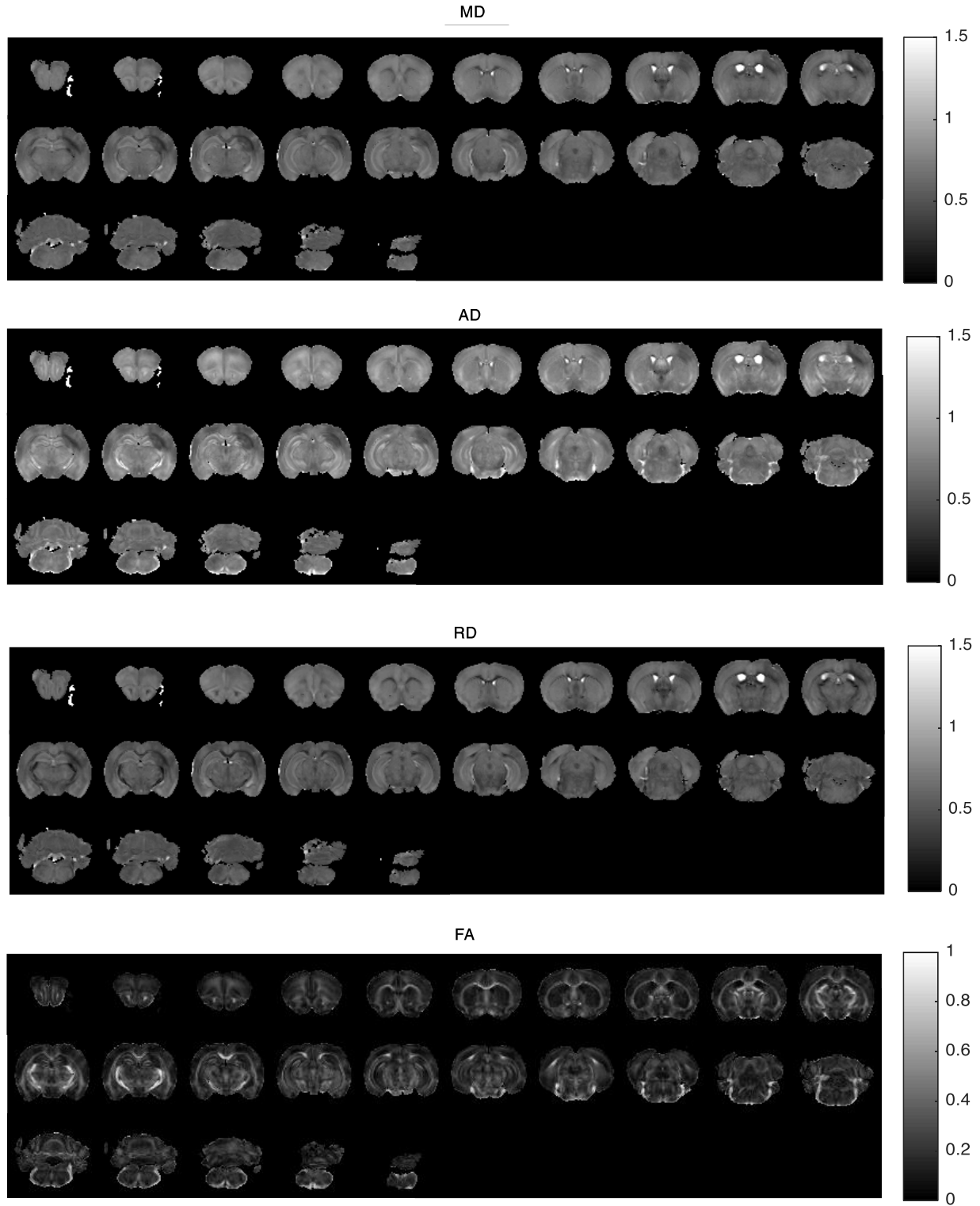
According to the acquisition protocol presented in Chapter 3 and Figure 3.4., seven DDE acquisitions were considered per sample, accounting also for pre-set gradient combinations with perpendicular  $q_2$  vectors. Raw data images from a representative sample from the stroke group for a total b-value gradient weighting of 3000, 1500 and 750  $\text{mm/s}^2$  over a representative direction are presented in Figure 4.6.



**Figure 4.6** – Double diffusion encoding images from a representative mouse brain over one direction. b-values for each shell of  $q_1$  and  $q_2$  vectors are: (A)  $b_1 = 3000 \text{ mm/s}^2$  and  $b_2 = 0 \text{ mm/s}^2$ ; (B)  $b_1 = 1500 \text{ mm/s}^2$  and  $b_2 = 1500 \text{ mm/s}^2$ ; (C)  $b_1 = 1500 \text{ mm/s}^2$  and  $b_2 = 1500 \text{ mm/s}^2$ , with perpendicular  $q_2$ ; (D)  $b_1 = 1500 \text{ mm/s}^2$  and  $b_2 = 0 \text{ mm/s}^2$ ; (E)  $b_1 = 750 \text{ mm/s}^2$  and  $b_2 = 750 \text{ mm/s}^2$ ; (F)  $b_1 = 750 \text{ mm/s}^2$  and  $b_2 = 750 \text{ mm/s}^2$ , with perpendicular  $q_2$ ; (G)  $b_1 = 750 \text{ mm/s}^2$  and  $b_2 = 0 \text{ mm/s}^2$ .

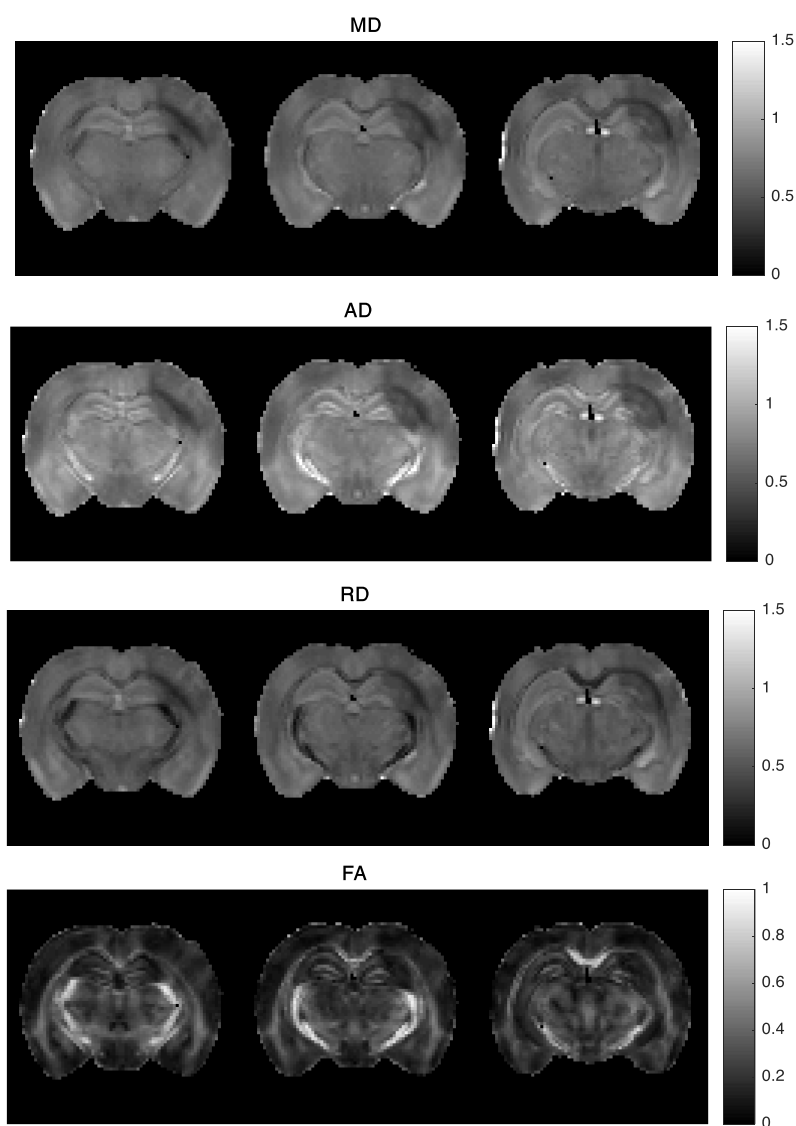


Subsequently to data denoising, correction for Gibbing-artifacts and sub-pixel registration, diffusion data were used to estimate tensors and their measures, starting by the acquisition parameters extraction of the b-matrix, which then was loaded in order for DTI to be estimated, supported by the weighted linear least squares estimator (Veraart et al., 2013). Then, the metrics MD, AD, RD and FA were calculated in each voxel for all animals from both groups and experiments.



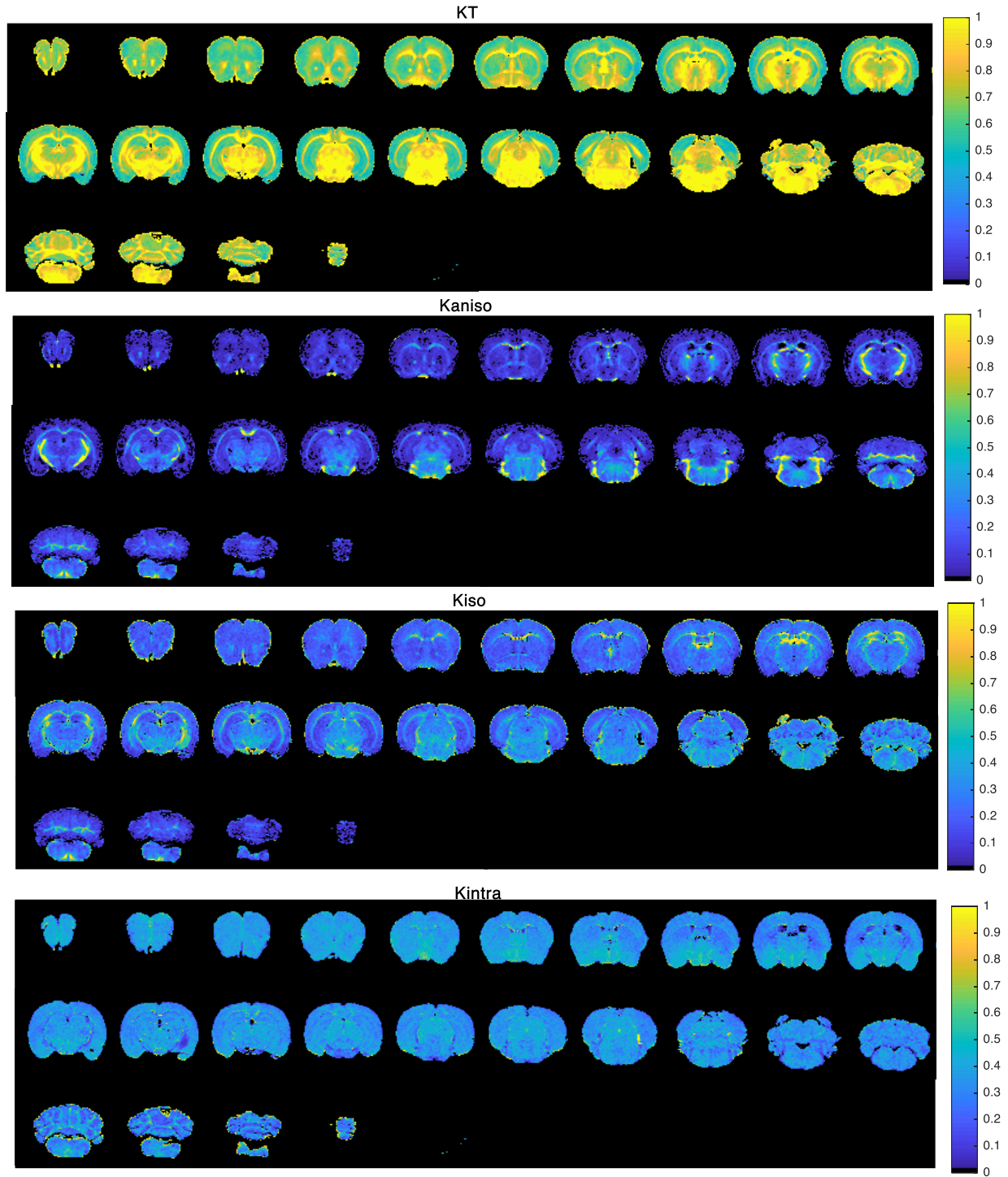
**Figure 4.7** – MD ( $\text{mm}^2/\text{s}$ ), RD ( $\text{mm}^2/\text{s}$ ), AD ( $\text{mm}^2/\text{s}$ ) and FA maps for representative stroked ex vivo brain.

Maps from representative slices from one animal from the stroke group are shown in Figure 4.8. The lesioned region is clearly depicted in all maps, presenting hypointense values in all metrics, affecting both white and gray matter.



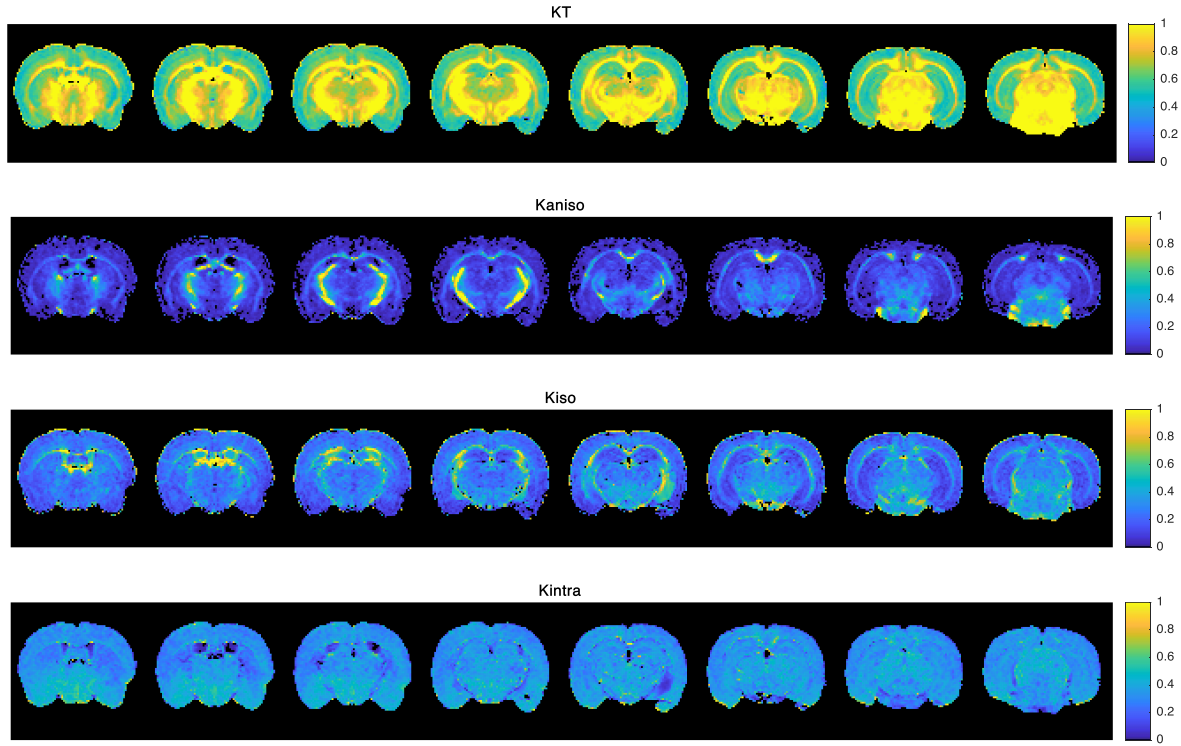
**Figure 4.8**– MD ( $\text{mm}^2/\text{s}$ ), RD ( $\text{mm}^2/\text{s}$ ), AD ( $\text{mm}^2/\text{s}$ ) and FA maps of 3 representative slices from representative stroked brain from Figure 4.7.

Figure 4.9 presents the kurtosis sources estimated from the CTI approach for 25 acquired slices for a representative control mouse brain.



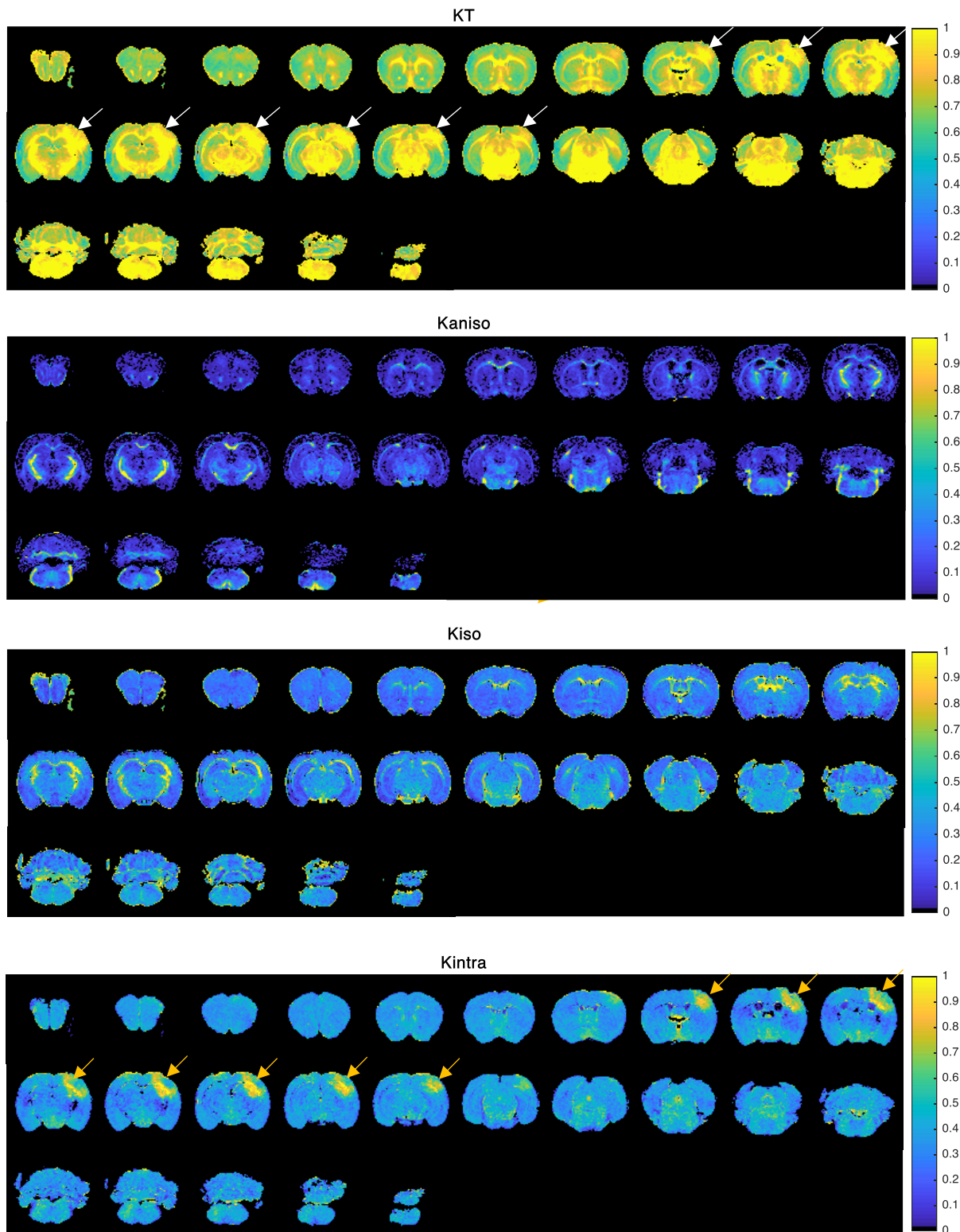
**Figure 4.9** – Kurtosis sources map (parula) for 25 representative slices from a control brain, ex vivo.  $K_T$  presents higher values than any other sources.  $K_{aniso}$  values reveal high intensities in white matter, whereas  $K_{iso}$  shows lower intensity values for both white and gray matter.

Figure 4.10 shows 8 slices from the previously presented representative control brain map.  $K_T$  presents higher values than any other sources.  $K_{aniso}$  values reveal high intensities in white matter, whereas  $K_{iso}$  is of low contribution for both white and gray matter, except for regions with dominant partial volume effects, similarly with the results presented by Henriques et al., 2020.



**Figure 4.10** – Kurtosis maps for 8 representative slices from the control brain sample from Figure 4.9.

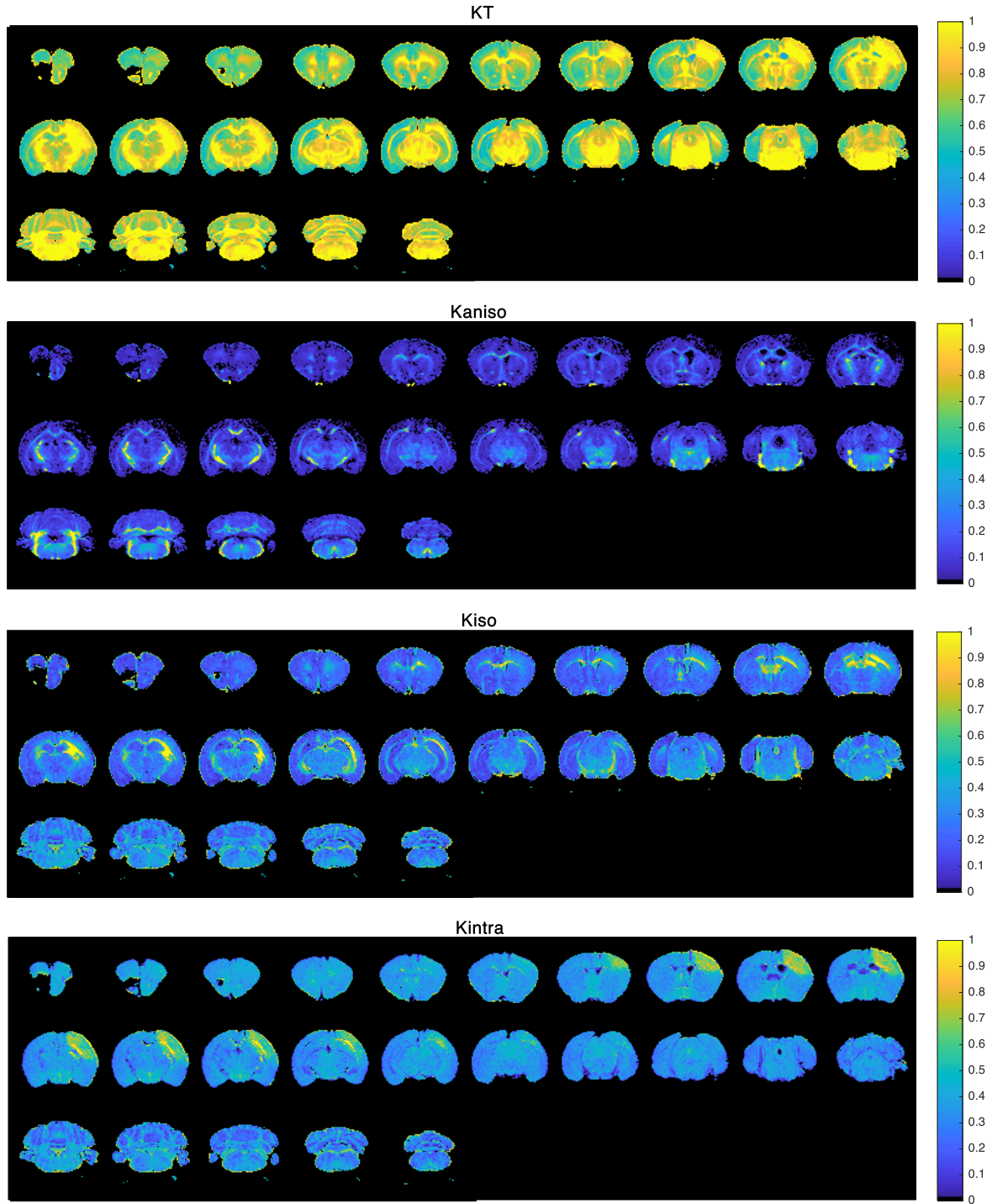
Figure 4.11 presents the kurtosis sources maps for 25 acquired slices for a representative stroked mouse brain.  $K_T$  presents higher values in the ipsilesional hemisphere, for both white and gray matter, as pointed by the white arrows.



**Figure 4.11** – Kurtosis sources map (parula) for 25 slices from a stroked brain, *ex vivo*.  $K_T$  presents higher values in the ipsilesional hemisphere, for both white and gray matter, as pointed by the white arrows. According to the  $K_{aniso}$  map, there is almost no contribution from the metric in the stroke lesion..  $K_{intra}$  reveals to have elevated contribution in both white and gray matter in the ipsilesional hemisphere, where the infarct core is located, as pointed by the yellow arrows.

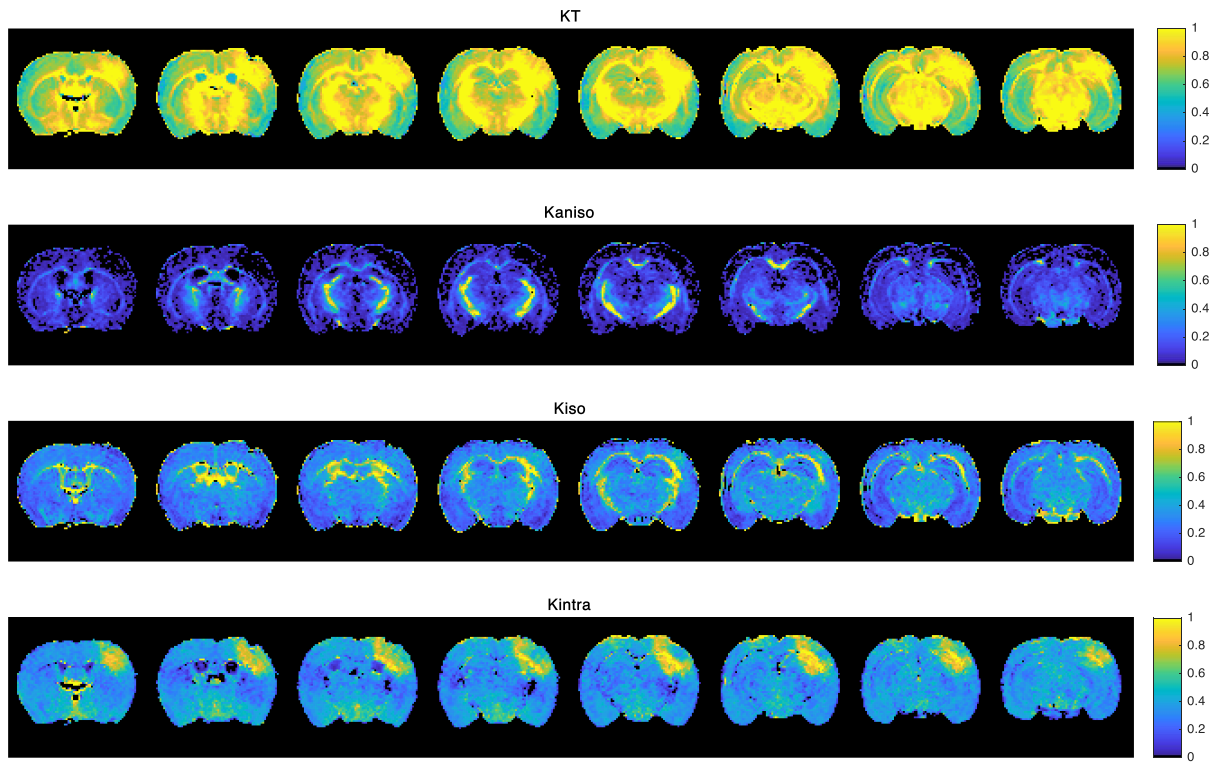


Figure 4.12 presents the kurtosis sources maps for 25 acquired slices for another stroked mouse brain, showing reproducibility across animals.



**Figure 4.12** - Kurtosis sources map (parula) for 25 slices from another stroked brain, ex vivo, presenting reproducibility when compared to Figure 4.11.

Figure 4.13 presents 8 representative slices from the sample presented in Figure 4.11. According to the  $K_{aniso}$  map, there is almost no contribution from the metric in the stroke lesion. In this case,  $K_{iso}$  reveals to have higher contribution than  $K_{aniso}$  in the infarcted region.  $K_{intra}$ , on the other hand, shows hyperintense values in both white and gray matter in the ipsilesional hemisphere, where the infarct core is located.



*Figure 4.13 – Kurtosis maps for 8 representative slices from the stroked ex vivo brain from Figure 4.11.*

## 4.1.2 ROIs Analysis

### 4.1.2.a. Sensitivity Analysis

To assess every kurtosis source metric sensitivity towards the infarcted region, ROIs were drawn manually in every *ex vivo* slice from each animal from the stroke group (N = 5). This process was repeated for each metric and the mean values from all animals with the respective standard error means were analysed in a bar plot. All plots are presented below in Figure 4.14. Importantly, of all metrics, intra-compartmental kurtosis was found to be more sensitive to the ischemic region than any other metric in gray matter and for all lesion covered voxels.  $K_{intra}$  presents  $1819 \pm 166$  (mean  $\pm$  standard error of the mean) voxels sensitive to the whole ROI (gray matter and white matter combined) and a total of  $1467 \pm 164$  voxels sensitive to the gray matter within the infarcted region (from Table 4.2).

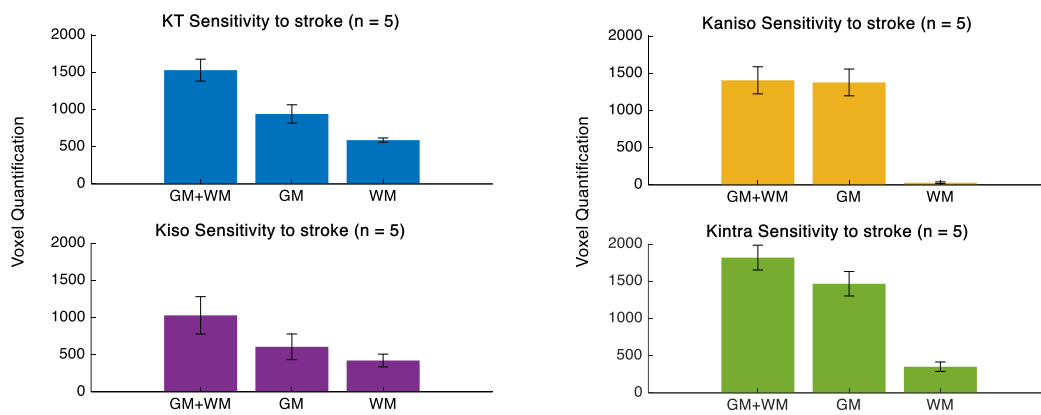


**Figure 4.14** - Sensitivity analysis in different metrics across different ROIs: R1 (GM + WM), R3 (WM) and R5 (GM). Different kurtosis sources are plotted along rows and each plot contains the respective kurtosis source measure for the R1, R3 and R5.

**Table 4.2** – Voxel quantification across selected ROIs (gray matter and white matter – GM and WM) within the infarcted region. The values presented reflect the mean number of voxels for all animals, the standard error of the mean ( $\mu \pm sem$ ) and respective associated volume.

$K_{source}$	ROI	No. voxels $\pm$ sem	Volume (mm <sup>3</sup> )
$K_T$	GM	$940 \pm 123$	9.34
	WM	$589 \pm 29$	5.85
$K_{aniso}$	GM	$1377 \pm 180$	13.69
	WM	$29 \pm 11$	0.29
$K_{iso}$	GM	$607 \pm 173$	6.03
	WM	$422 \pm 86$	4.20
$K_{intra}$	GM	$1467 \pm 164$	14.58
	WM	$351 \pm 64$	3.49



### 4.1.2.b. Specificity Analysis

Once CTI's metrics were established to reveal higher sensitivity towards the acute lesion, the next analysis to consider was related to specificity, in order to be able to consider the contribution from each non-Gaussian source on the ipsilesional regions of interest, when compared to the control counterpart regions. For this analysis, one should consider all the ROIs that play an important role for a accurate comparison: R1 – the ipsilesional region (WM + GM) and R2 – its counterpart in the opposite hemisphere, R3 and R4 – concerning the white matter region within R1 and the white matter region within R2, R5 and R6 – corresponding to the gray matter region within R1 and the gray matter region within R2, R7 – the left hemisphere region similarly located to where the lesion is in the stroke group, accounting for white and gray matter simultaneously, R8 – white matter within R7, and at last R9 – gray matter within R7. The signal intensities within all regions were averaged across each animal and then across all animals from the respective subgroup (“ipsilesional” and “contralesional” are subgroups from the stroke group, whereas “control” concerns the ipsilateral hemisphere from the sham group). The results are presented in Figure 4.15, measuring different kurtosis sources per row and different ROIs per column.

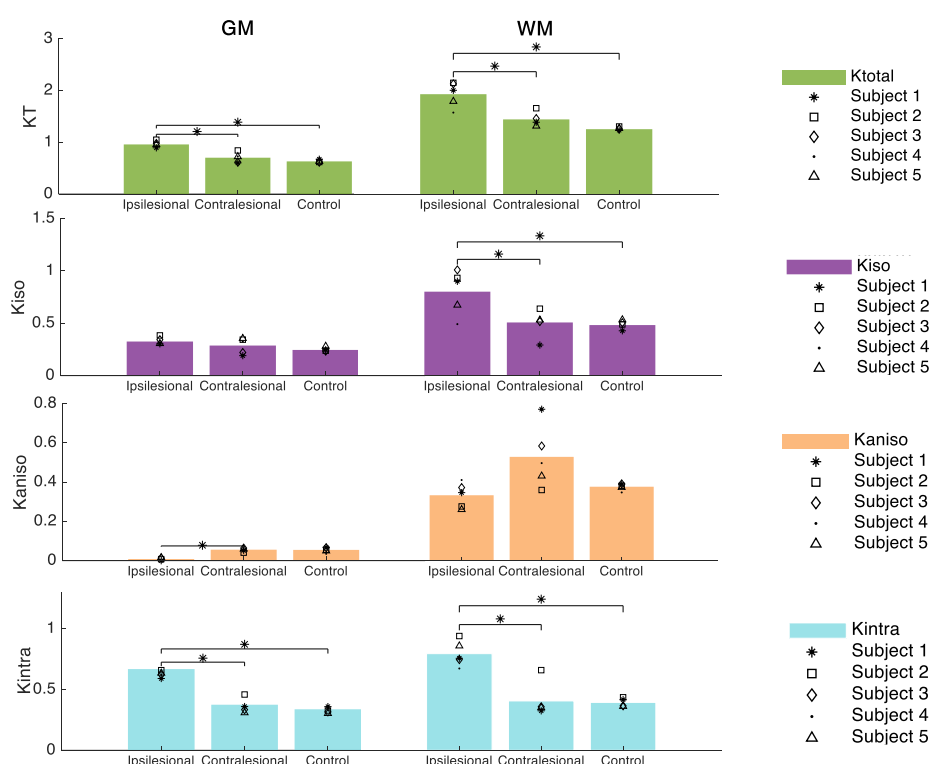


**Figure 4.15** - Specificity analysis after ANOVA (multiple comparisons) across different regions of interest (ROIs). Different kurtosis sources are plotted along rows and each plot contains the respective kurtosis source measure for the R1, R2 and R3, consecutively. Each column refers to only GM and only WM, respectively ( $\alpha = 0.05$ ).

A statistical analysis was then conducted to assess whether the differences between mean values in each ROI for each metric averaged across mice (from each group) were significant through a one-way ANOVA test, and a Bonferroni correction was performed for multiple comparisons across the different diffusion metrics.

The results suggest that from all kurtosis sources,  $K_T$  and  $K_{intra}$  reveal mean values for both gray matter and white matter with statistically significant differences for p-value < 0.05 between different subgroups. Within the gray matter ROIs (R5, R6 and R9), the mean  $K_T$  and  $K_{intra}$  values in the ipsilesional region (R5) are statistically significant from the mean values of the contralesional hemisphere ROI (R6), as well as from the ipsilateral ROI from the control group (R9). It is worth mentioning that the same applies for the white matter ROIs (R3, R4 and R8). However, the relative difference is shown to be more elevated in  $K_{intra}$  than in  $K_T$ . With regards to other sources,  $K_{iso}$  presented statistically significant differences within white matter regions between the ipsilesional region (R3) and the contralesional hemisphere ROI (R4) and the ipsilateral ROI from the control group (R8). Concerning the  $K_{aniso}$  source, differences were shown to be statistically significant between gray matter regions in the stroke group, thus between the ipsilesional and contralesional hemispheres (R5 and R6, respectively).

## 4.2 Histological Staining

Figure 4.16 shows example images of a coronal sectioned stroked brain for haematoxylin and eosin (HE) staining, on the left, and Nissl staining, on the right. A critical selected gray matter region was magnified with a factor of 2 on Fiji ImageJ, presenting cell damage associated with necrosis and a brighter coloured region in the lesion site associated with cell loss, in HE (A) and Nissl (B) staining, respectively.

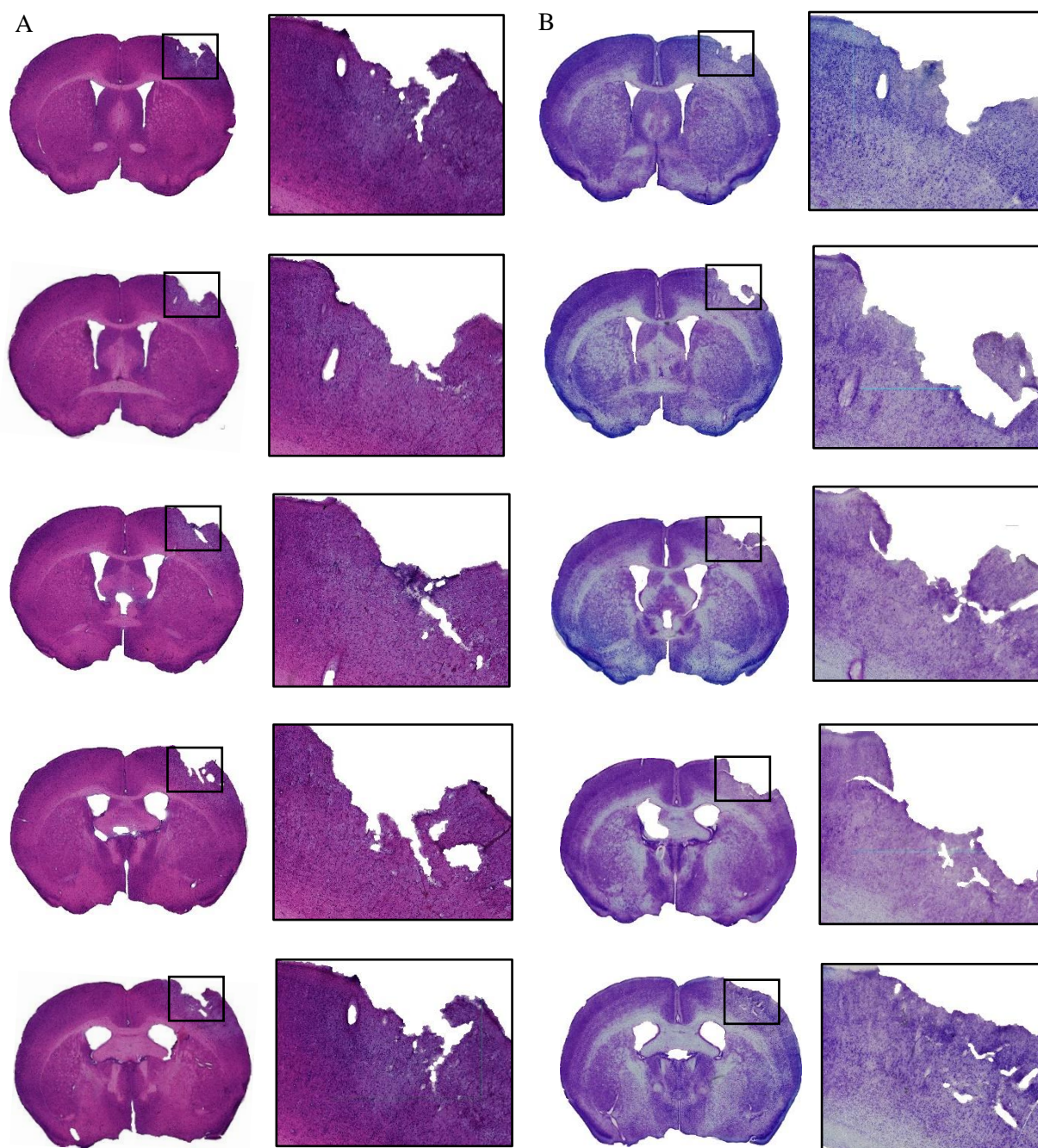


**Figure 4.16** – Representative (A) HE and (B) Nissl-stained brain sections showing the lesion in the subcortical region of the left hemisphere from a representative mouse brain perfused at 3 hours post ischemic stroke.

### 4.3. *In vivo*

Figure 4.17 and Figure 4.18 show T2-weighted images from the *in vivo* acquisition after stroke. The infarct volume was not calculated for the *in vivo* experiment since using *in vivo* MRI to assess volume is known to be likely to be biased by physiological noise sources and variations in heart rate and blood pressure because of anaesthesia, susceptible to affecting the capillary bed and tissue state – which in turn would affect the estimate (Albrecht et al, 2014; Bay et al., 2018). It is possible to observe in both sets of images that there is a slight tendency for signal to be higher on the dorsal side compared to ventral side, since the cryocoil used for reception is a surface coil, hence being closer to the dorsal region of the brain.

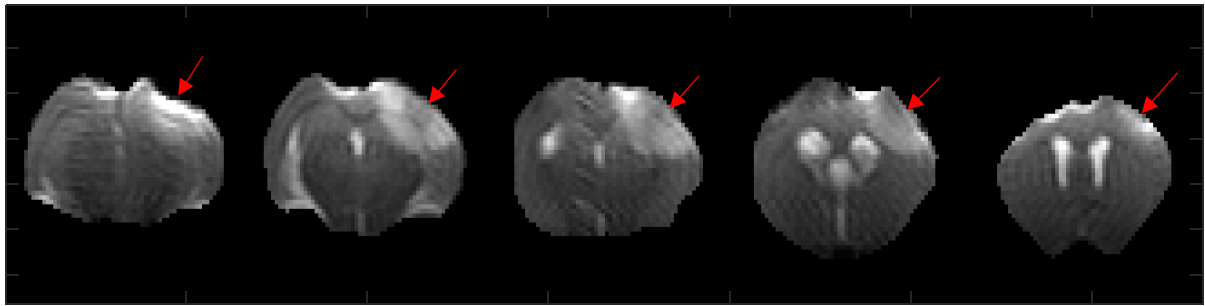


**Figure 4.17** – Raw T2-weighted images from the acquired *in vivo* mouse 3 h post stroke onset. A total of 5 coronal slices were acquired and are presented from rostral to caudal direction. The red arrows point towards the lesion site.

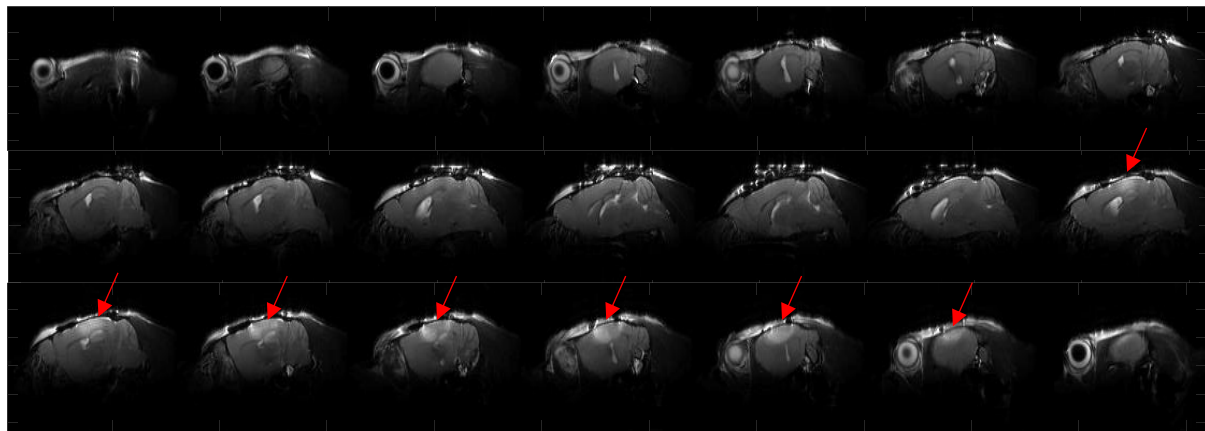


**Figure 4.18** – Raw T2-weighted images from the acquired *in vivo* mouse 3 h post stroke onset. 21 sagittal slices are presented from right to left. The red arrows point towards the lesion site.

The resulting CTI maps are presented in Figure 4.19 and 4.20 for a control mouse and a stroked mouse 3 h post ischemic insult, respectively. The *in vivo* maps corroborate with the results obtained *in vivo* by Henriques et al., 2020 in the case of the control healthy animal, and with the results *ex vivo* for the brain which underwent ischemia.

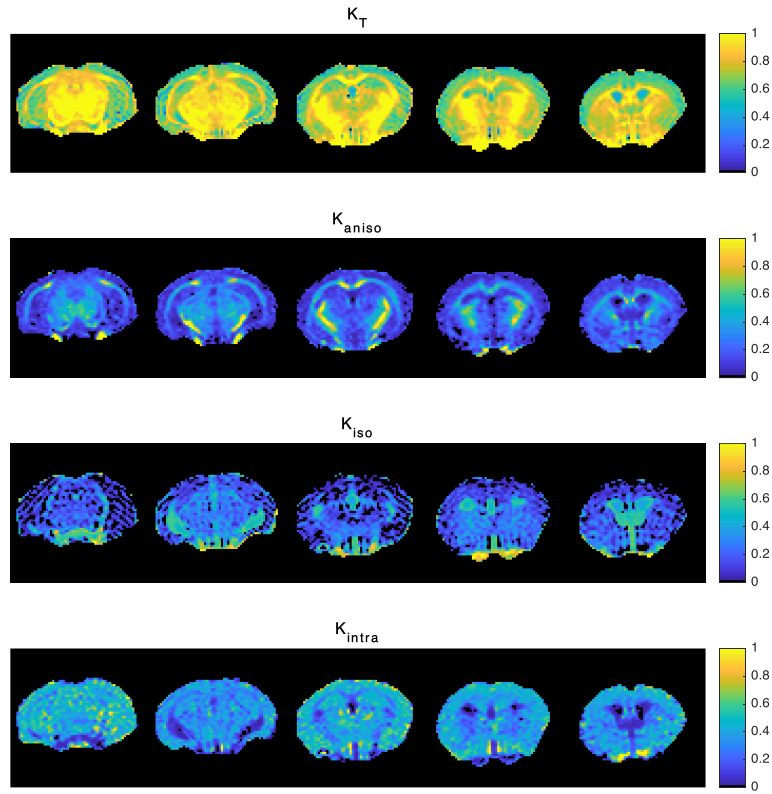


**Figure 4.19** – Kurtosis sources map (parula) for in vivo acquisitions for control animal.  $K_T$  presents higher values than any other sources.  $K_{aniso}$  values reveal high intensities in white matter, whereas  $K_{iso}$  shows lower intensity values for both white and gray matter.

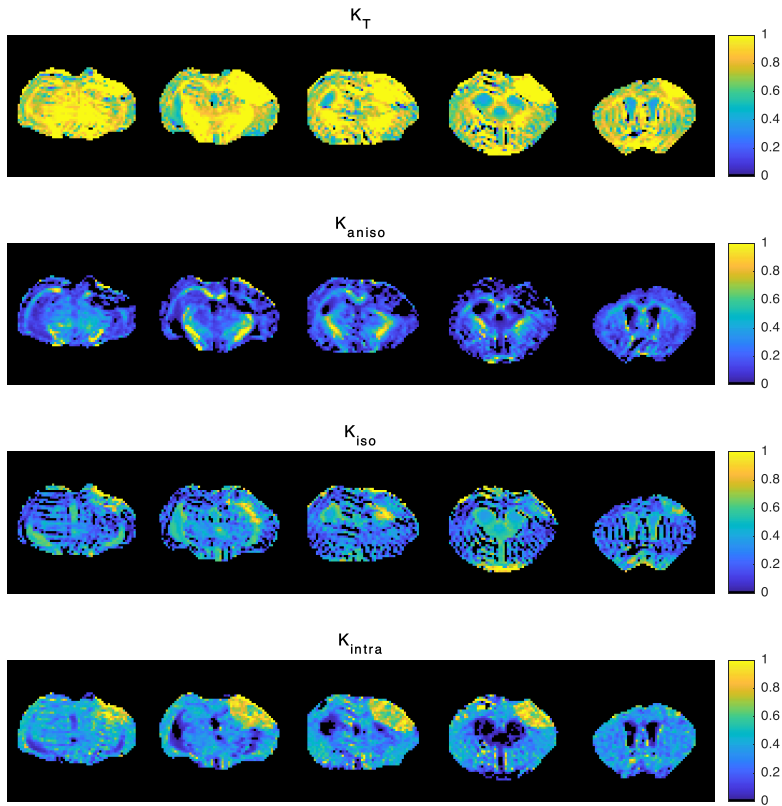


**Figure 4.20**– Kurtosis sources map (parula) for in vivo acquisitions from a stroked mouse.  $K_T$  presents high intensity values in the lesion area, whereas  $K_{aniso}$  seems to have little contribution in the same region, for both white and gray matter.  $K_{iso}$  shows elevated intensity values in white matter.  $K_{intra}$  reveals, as presented in the ex vivo maps, hyperintense values in the stroke region in the ipsilesional hemisphere, for both white and gray matter





## 5. Discussion

### 5.1 Technical Aspects

Rodent models have played important roles in investigating disease in general and ischemia in particular. Our study utilized the photothrombotic model of ischemia both *ex vivo* and *in vivo* to investigate how a new imaging methodology could highlight microstructural features emerging upon ischemia. We chose this particular model rather than other commonly used permanent occlusion models (such as the thromboembolic, MCAO or non-clot embolic models) since it allows a well-defined and reproducible infarcted area, has a very low mortality rate (in contrast with the other models, which tend to be very heterogeneous and variable in lesion size) (Dirnagl & Walz, 2016). In this study, male animals were used instead of females to avoid any hormonal imbalance.

The intravenous route for the solution administration was influenced by the variability rates reported in studies testing different administration approaches (Dirnagl & Walz, 2016)(Labat-gest & Tomasi, 2013). The lesion size tends to vary when the solution is administered intraperitoneally compared to intravenously. Furthermore, an intravenous application route provides a clear indication of correct administration – pink coloured tail veins and toes are promptly visible, indicating that the solution is present in the bloodstream. Our choice of the retroorbital route within the range of intravenous possibilities – retroorbital, tail vein and jugular vein – was of higher success rate upon training than tail vein administration, especially since the tail veins are not as visible in this strain of mouse (C57BL/6). This caused no inconvenience since both approaches are equally reliable (Yardeni et al., 2011). The jugular vein application route was excluded since it required more means and materials (surgical microscope and custom-modified catheter), hence being a more complex option for the common endpoint. After administration, irradiation was promptly started and lasted for 15 minutes to guarantee maximal results – given that the dye would have washed out from the bloodstream a few minutes prior to the end of the irradiation.

Our results show that, as expected, the lesion size was reproducible and consistent (Figure 4.1). However, by counteracting with the high variability persistent in humans, one could argue that this is not a good reproduction of the human ischemic infarct. Nonetheless, the model's consistency and reproducibility, whilst still implying the standard clot formation resemblance and underlying pathophysiological events, allowed for a successful assessment of the novel imaging methodology proposed here (CTI). A more heterogeneous model may not have served well for such purposes.

The very good reproducibility in terms of location and size is one of the main advantages of the Rose Bengal model (Jablonka et al., 2007; Labat-gest & Tomasi, 2013; Nowicka et al., 2008) and our results are consistent with these observations. Lesion volume (Table 4.1) was highly consistent, resulting from the elevated precision at which the x-y stereotaxic coordinates could be set (0.001 mm), the stable beam light intensity and the measured amount of solution to be administered (according to the weight of the animal). Only a single outlier was observed (Stroke 2), likely due to inadequate administration of the solution or inaccurate measurement of the height between the optic fibre tip and the skull, which might have led to an unwanted light spread.

Another factor contributing to the high reproducibility, this time in terms of dMRI methodology is our choice of *ex vivo* acquisitions as the main exploration path for the full potential of CTI. This assists in avoiding many acquisitions time limitations or artefacts related to physiological noise (animal movement, respiration, alterations in heart rate and temperature) in *in vivo* scans; furthermore, the *ex vivo* acquisitions enable a higher than usual resolution and general quality of data. All these assist with ensuring that the data acquired can be used to assess the new methodology more accurately.

The DDE EPI pulse sequences used in this study were optimized to avoid Gibbs-ringing artifacts, which were consistently present in all preliminary experiments, by manually correcting the receiver amplifier gain. This optimized protocol resulted in raw images with significantly attenuated Gibbs-ringing. This assisted with the denoising and Gibbs-ringing post-processing procedures that eventually provided robust, high signal to noise, and artifact free images (Figure 4.7). Our images did not seem to have improved with the PCA denoising, as shown in Figure 3.12, likely due to multi-channel interpolation effects or image reconstruction steps that might have led to a noise distribution alteration, different from the Marchenko–Pastur’s distribution. Suppressing noise of the dMRI data may be of high importance for CTI, since this involves the estimation of a large number of parameters from the differences on different DDE acquisitions at high b-values. Therefore, it would be pertinent in future studies to develop strategies to improve the performance of PCA denoising strategies on DDE dMRI data, such as individual channel denoising in order to attenuate interpolation effects.

When evaluating the conventional metrics already measured previously in the Rose Bengal model, our results were consistent with the literature, further providing confidence in the model’s efficacy. Namely, high resolution coronal, sagittal and axial T2 weighted images (Figure 4.2, 4.3 and 4.4, respectively) revealed the stroke lesion site with a hyperintense contrast, as expected. Control conditions evidenced no difference between hemispheres (Figure 4.5.), suggesting that no coil or otherwise other artifacts could contribute to the observed lesions in the stroked group. Elevated values in T2-weighted images in the lesioned region of the brain are corroborated in different studies at the same time point post ischemic stroke in mice and rats (Chen et al., 2007; Neumann-Haefelin et al., 2000).

## 5.2. dMRI Findings

In terms of dMRI metrics, since pathophysiological processes such as ischemic stroke alter the microstructural integrity in the tissue and subsequently provoke alterations in tissue anisotropy, FA presented decreased values in the WM ischemic region relatively to normal WM. This can be due to degeneration processes but also multiple crossing fibres in the voxel, showing consistency according to what has been reported in the literature at an early time point post stroke onset (Chen et al., 2008; Sorensen et al., 1999). It is worth noting that the results obtained at the 3 h time point might already reflect a subacute stage of ischemia, according to the pattern followed by FA – reported to be elevated during the first hour of focal cerebral ischemia and to decrease over the following 3 hours (Carano et al., 2000; Sotak, 2002). Although intriguing, this metric cannot resolve alterations involving structures with great dispersion, in GM for instance, which is an important limiting factor.

The observed acute reduction shown in the MD maps ( $39.4 \pm 8.9 \%$ ) is also consistent with previous studies – reported to decrease in the first hours post ischemic onset (Helpern et al., 1993; Jiang et al., 1997). As previously mentioned, at the studied time point, cytotoxic edema and peri-infarct depolarizations are expected to be occurring at a lower scale when compared to the first minutes within the beginning of the ischemic insult, while inflammation and apoptosis are starting to occur (González et al., 2011) (Figure 2.3). Hence, the resulting contrasts and estimated metrics may also reflect some contributions from vasogenic edema. Interestingly, the ADC decreases at an acute phase, which have been suggested to be associated with restricted or hindered diffusion due to cell swelling and neurite beading (Budde & Frank, 2010), could potentially be due to restricted diffusion in individual compartments with reflecting barriers, at a long diffusion time regime. It is important to note, however, that due to its lack of specificity, MD cannot be used to disentangle these different biological underpinnings.



### 5.2.1. CTI

Previous studies show that  $K_T$  is more sensitive than DTI metrics, such as MD, and less sensitive to vasogenic effects. Particularly in this model, studies have suggested that mean kurtosis remains elevated until the subacute phase, indeed enhancing an elevated degree of complexity and heterogeneity within the lesioned area (Jensen & Helper, 2010; Jensen et al., 2005). These observations are consistent with our  $K_T$  results; however, as for MD, this metric on its own is limited to a conflation of effects which might jeopardize specificity and further interpretations.

Once we were certain that the model reproduced well and that the metrics obtained from our conventional measurements are consistent with the literature, we turned to the new findings, namely, the CTI metrics in stroke, which are reported here for the first time.

In previous work, the changes in  $K_{aniso}$  exhibited elevated sensitivity towards microscopic diffusion anisotropy, i.e., diffusion anisotropy that rises from local microstructural anisotropy rather than effects of tissue orientation dispersion (Henriques et al., 2020). In our case, it was confirmed that this metric would be sensitive to alteration not only in well aligned structures (a tendency for a decrease in WM was perceived) but also in GM regions in which  $K_{aniso}$  was significantly sensitive to microscopic anisotropic decreases in stroke lesions (Figure 4.15). This result suggests a role for local changes in anisotropy, likely originating from beading effects (Budde & Frank, 2010), in ischemia.  $K_{iso}$  alterations in this study likely reflect more of a partial volume contribution from free water; considering that at this specific time point effects from vasogenic edema might already be occurring, our findings are prone to reflect a higher sensitivity to this effect. Nonetheless, it should be noted that the observed considerable WM changes might indicate augmented partial volume effects in the lesioned area, considering that WM is located adjacently to the ventricles, or a preliminary edema phenomena. The obtained results are rather promising since they point to an elevated sensitivity and specificity, mainly through its measurement of  $K_{intra}$ , towards focal ischemic tissue in gray matter at an early stage post ischemic onset. Interestingly, the CTI-derived  $K_{intra}$ , was more sensitive than  $K_T$  (measured in the more conventional approaches) evidencing both more voxels and a larger contrast. This higher sensitivity can be attributed by the higher specificity of  $K_{intra}$  to biological alterations. While  $K_T$  captures the alterations from all its different non-Gaussian sources which may oppose to each other (e.g.,  $K_{aniso}$  decreases vs  $K_{iso}$  and  $K_{intra}$  increases),  $K_{intra}$  only captures non-Gaussian diffusion effect that rises from diffusion within reflecting barriers (Henriques et al., 2020). Indeed, this is in line with previous studies suggesting that ischemia preferentially alters the microstructural complexity of intra-axonal environments (e.g., Hui et al., 2012).

Our results are just the first observations of these effects, and more studies are required to further investigate the mechanisms underlying the changes of different kurtosis sources upon ischemia, especially a further understanding of the alterations captured by  $K_{intra}$ . Note that, due to its novelty, the biological underpinnings of  $K_{intra}$  have not been fully explored yet.

Our preliminary histological staining corroborated the efficacy of the stroke model, and also agreed qualitatively with CTI metrics. A comparison between the two shows that higher  $K_{intra}$  values reflect the necrosis transition phenomena which is occurring along with cell loss visible in the Nissl staining counterpart slice (Jiang et al., 1997) (Figure 5.1).

In addition to further histological analyses, it is important to note that future studies could try to elucidate the relationship between  $K_{intra}$  estimates and properties of tissue intracellular space by combining the CTI methodology with MR spectroscopy targeting the diffusivity of intra-cellular metabolites (Shemesh et al., 2014).

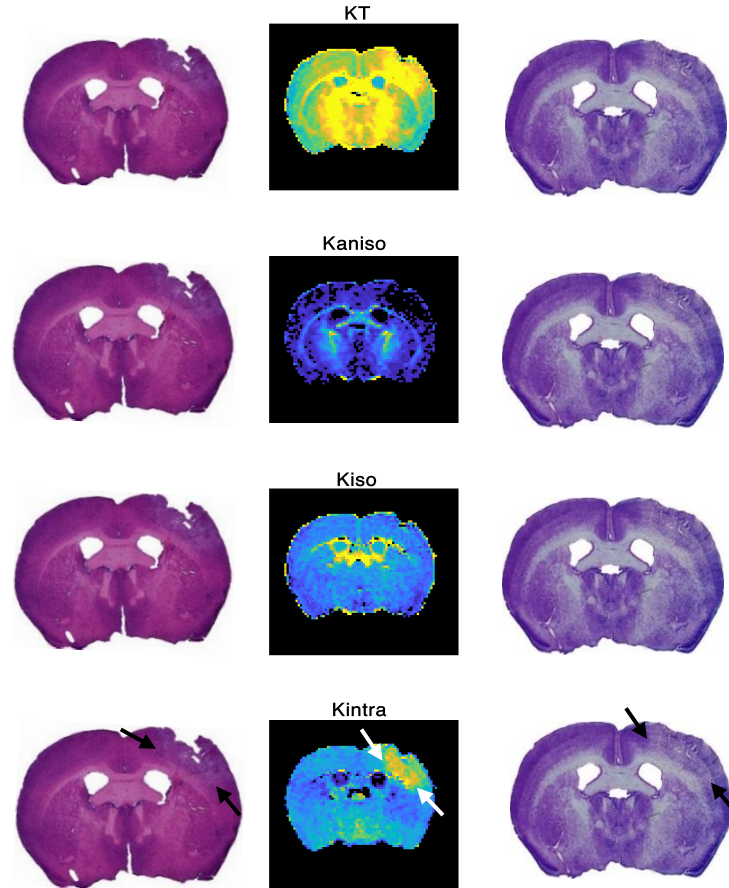


**Figure 5.1** – Comparison between histological HE and Nissl staining in a representative slice from a stroked brain and its counterpart slice in the CTI maps. Note that  $K_{intra}$  seems to be more selective to a transition to necrosis in the lesion core, where both HE and Cresyl violet (Nissl) staining present clearer regions, associated with the presence of less cell bodies. (black arrows in staining, white arrows in CTI maps)

According to our *in vivo* results, these proved to be reproducible at a first qualitative analysis with the *ex vivo* maps, exhibiting elevated  $K_T$  values and  $K_{intra}$  stroke specific intensities within the infarcted area, and hence indicating that the witnessed findings are not exclusively due to *ex vivo* effects. Although DDE paradigm for CTI requirements suggests considerable consistency across results *in vivo*, an optimization of the parameters is encouraged to be performed to correct for susceptibility artifacts, for instance, which were noticed in raw data. The use of an agar gel cap could be a potential alternative since it has been found to reduce this artifact in mouse brain (Adamczak et al., 2010). Moreover, a reasonable number of *in vivo* acquisitions are ought to be performed in the near future to increase statistical power.

## 6. Conclusions

This project aimed to harness advanced diffusion pulse sequences, to map for the first time metrics associated with the correlation tensor in tissue undergoing ischemic alterations. To achieve this goal, DDE sequences provided the necessary means for executing CTI in a mouse stroke model at 3 hours after infarct onset.

The photothrombotic model was successfully reproduced in all mice via a photosensitive dye injection followed by a photochemical activation. The suitability of the correlation tensor extraction and analysis was validated in this model, both *ex vivo* and *in vivo*. The use of DDE sequences written in-house enabled the characterization of different sources of kurtosis towards severely dynamic processes at a critical time point after focal unilateral ischemic stroke induction. Significant differences between the ischemic ROI (combining GM and WM), the contralesional ROI and the respective ipsilateral control hemisphere ROI were confirmed specifically in the powder averaged total kurtosis (combining all sources) for GM and WM separately, in the variance derived from isotropic tensors related kurtosis in WM, as well as in variance derived from intra-compartmental kurtosis (in GM).  $K_{intra}$  proved to be the source prevailing the most sensitive to alterations within the first hours post infarct, accounting for a higher number of affected voxels.

The present study shows that CTI is capable of resolving microscopic tissue features *ex vivo* and *in vivo*, which until now were obfuscated in conventional dMRI measurements. These are critical first steps towards resolving the contributions of cytotoxic and vasogenic edema sources, as well as potential for revealing salvageable tissue or ongoing excitotoxicity.

In conclusion, the conditions for a more sensitive and accurate detection of specific microstructural changes post-ischemia were successfully met throughout this work. Given the versatility of the used paradigm and the robustness of the results, a longitudinal assessment of the presented diffusion metrics in the same model is encouraged to be pursued as well as sequence improvement aiming at reducing acquisition time. Future perspectives also include the application of fMRI studies to assess functional outcomes along with CTI metrics in later stages. This will hopefully lead to an exhaustive and ground-breaking analysis inherent to stroke-driven alterations in tissue at critical time points, highly beneficial for the development of novel and more specific therapies.



## 7. References

- Adamczak, J. M., Farr, T. D., Seehafer, J. U., Kalthoff, D., & Hoehn, M. (2010). High field BOLD response to forepaw stimulation in the mouse. *NeuroImage*, 51(2), 704–712. <https://doi.org/10.1016/j.neuroimage.2010.02.083>
- Adluru, G., Gur, Y., Anderson, J. S., Richards, L. G., Adluru, G., & DiBella, E. V. R. (2014). Assessment of white matter microstructure in stroke patients using NODDI. *Conf Proc IEEE Eng Med Biol Soc. 2014*, 742–745. <https://doi.org/10.1109/EMBC.2014.6943697>
- Albrecht, M., Henke, J., Tacke, S., Markert, M., & Guth, B. (2014). Effects of isoflurane, ketamine-xylazine and a combination of medetomidine, midazolam and fentanyl on physiological variables continuously measured by telemetry in Wistar rats. *BMC Veterinary Research*, 10(1), 198. <https://doi.org/10.1186/s12917-014-0198-3>
- Amarenco, P., Bogousslavsky, J., Caplan, L. R., Donnan, G. A., & Hennerici, M. G. (2009). Classification of stroke subtypes. *Cerebrovascular Diseases*, 27(5), 493–501. <https://doi.org/10.1159/000210432>
- Assaf, Y., & Cohen, Y. (1998). Non-Mono-Exponential Attenuation of Water and N-Acetyl Aspartate Signals Due to Diffusion in Brain Tissue. *Journal of Magnetic Resonance*, 131(1), 69–85. <https://doi.org/10.1006/jmre.1997.1313>
- Baird, A. E., & Warach, S. (1998). *Magnetic Resonance Imaging of Acute Stroke*. 583–609.
- Barbier, E. L., Lamalle, L., & Décorps, M. (2001). Methodology of brain perfusion imaging. *Journal of Magnetic Resonance Imaging*, 13(4), 496–520. <https://doi.org/10.1002/jmri.1073>
- Baron, J. C., Bousser, M. G., Rey, A., Guillard, A., Comar, D., & Castaigne, P. (1981). Reversal of focal “misery-perfusion syndrome” by extra-intracranial arterial bypass in hemodynamic cerebral ischemia a case study with 180 positron emission tomography. *Stroke*, 12(4), 454–459. <https://doi.org/10.1161/01.STR.12.4.454>
- Basser, P. J. (1995). Inferring Microstructural Features and the Physiological State of Tissues from Diffusion Weighted Images. *NMR in BIOMEDICINE*, 8(September), 333–344. Retrieved from <http://eutils.ncbi.nlm.nih.gov/entrez/eutils/elink.fcgi?dbfrom=pubmed&id=8739270&retmode=ref&cmd=prlinks>
- Basser, P. J., Mattiello, J., & LeBihan, D. (1994). MR diffusion tensor spectroscopy and imaging. *Biophysical Journal*, 66(1), 259–267. [https://doi.org/10.1016/S0006-3495\(94\)80775-1](https://doi.org/10.1016/S0006-3495(94)80775-1)
- Basser, P. J., & Ozarslan, E. (2014). Introduction to Diffusion MRI. In H. Johansen-Berg & T. Behrens (Eds.), *Diffusion MRI: From Quantitative Measurement to In vivo Neuroanatomy* (Second Edi, pp. 3–6). Elsevier Inc.
- Bay, V., Kjølby, B. F., Iversen, N. K., Mikkelsen, I. K., Ardalán, M., Nyengaard, J. R., ... Hansen, B. (2018). Stroke infarct volume estimation in fixed tissue: Comparison of diffusion kurtosis imaging to diffusion weighted imaging and histology in a rodent MCAO model. *PLOS ONE*, 13(4), e0196161. <https://doi.org/10.1371/journal.pone.0196161>
- Beaulieu, C. (2002). The basis of anisotropic water diffusion in the nervous system - A technical review. *NMR in Biomedicine*, 15(7–8), 435–455. <https://doi.org/10.1002/nbm.782>
- Bernstein, M. A., King, K. F., & Xiaohong, J. Z. (2004). Handbook of MRI Pulse Sequences. In *Bulletin of the Chemical Society of Ethiopia* (1st Editio, Vol. 21). <https://doi.org/10.4314/bcse.v21i3.21211>
- Bihan, D. Le. (1995). Molecular diffusion, tissue microdynamics and microstructure. *NMR in Biomedicine*, 8(7), 375–386. <https://doi.org/10.1002/nbm.1940080711>
- Bloch, F. (1946). Nuclear induction. *Physical Review*, 70(7–8), 460–474. <https://doi.org/10.1103/PhysRev.70.460>
- Bogousslavsky, J., Melle, G. Van, & Regli, F. (1988). Original Contributions The Lausanne Stroke Registry: Analysis of 1,000 Consecutive Patients With First Stroke. *AHA/ASA Journal*.
- Brown, R. (1829). The Philosophical Magazine and Annals of Philosophy. *New Series*, 4(21)(21), 161–173. Retrieved from Mechanics
- Budde, M. D., & Frank, J. A. (2010). Neurite beading is sufficient to decrease the apparent diffusion coefficient after ischemic stroke. *Proceedings of the National Academy of Sciences of the United States of America*, 107(32), 14472–14477. <https://doi.org/10.1073/pnas.1004841107>
- Callaghan, P. T. (1991). *Principles of Nuclear Magnetic Resonance Microscopy*. Oxford University

- Press.
- Canazza, A., Minati, L., Boffano, C., Parati, E., & Binks, S. (2014). Experimental models of brain ischemia: A review of techniques, magnetic resonance imaging, and investigational cell-based therapies. *Frontiers in Neurology*, 5 FEB(February), 1–16. <https://doi.org/10.3389/fneur.2014.00019>
- Carano, R. A. D., Li, F., Irie, K., Helmer, K. G., Silva, M. D., Fisher, M., & Sotak, C. H. (2000). Multispectral analysis of the temporal evolution of cerebral ischemia in the rat brain. *Journal of Magnetic Resonance Imaging*, 12(6), 842–858. [https://doi.org/10.1002/1522-2586\(200012\)12:6<842::AID-JMRI7>3.0.CO;2-5](https://doi.org/10.1002/1522-2586(200012)12:6<842::AID-JMRI7>3.0.CO;2-5)
- Carr H. Y., & E.M., P. (1983). Effects of diffusion on free precession in nuclear magnetic resonance experiments. *Physical Review*, Vol. 246, p. 1983. Retrieved from <http://link.aps.org/doi/10.1103/PhysRev.94.630>
- Chang, D. C., Rorschach, H. E., Nichols, B. L., & Hazlewood, C. F. (1973). Implications of Diffusion Coefficient Measurements for the Structure of Cellular Water. *Annals of the New York Academy of Sciences*, 204(1), 434–443. <https://doi.org/10.1111/j.1749-6632.1973.tb30796.x>
- Chavhan, G. B., Babyn, P. S., Thomas, B., Shroff, M. M., & Haacke, E. M. (2009). Principles, Techniques, and Applications of T2\*-based MR Imaging and Its Special Applications. *RadioGraphics*, 29(5), 1433–1449. <https://doi.org/10.1148/rg.295095034>
- Chen, F., Suzuki, Y., Nagai, N., Jin, L., Yu, J., Wang, H., ... Ni, Y. (2007). Rodent stroke induced by photochemical occlusion of proximal middle cerebral artery: Evolution monitored with MR imaging and histopathology. *European Journal of Radiology*, 63(1), 68–75. <https://doi.org/10.1016/j.ejrad.2007.01.005>
- Chen, F., Suzuki, Y., Nagai, N., Peeters, R., Coenegrachts, K., Coudyzer, W., ... Ni, Y. (2004). Visualization of stroke with clinical MR imagers in rats: a feasibility study. *Radiology*, 233(3), 905–911. <https://doi.org/10.1148/radiol.2333031658>
- Chen, Z., Ni, P., Zhang, J., Ye, Y., Xiao, H., Qian, G., ... Zeng, Y. (2008). Evaluating ischemic stroke with diffusion tensor imaging. *Neurological Research*, 30(7), 720–726. <https://doi.org/10.1179/174313208X297968>
- Cheung, M. M., Hui, E. S., Chan, K. C., Helpen, J. A., Qi, L., & Wu, E. X. (2009). Does diffusion kurtosis imaging lead to better neural tissue characterization? A rodent brain maturation study. *NeuroImage*, 45(2), 386–392. <https://doi.org/10.1016/j.neuroimage.2008.12.018>
- Chiang, T., Messing, R. O., & Chou, W.-H. (2011). Mouse Model of Middle Cerebral Artery Occlusion. *Journal of Visualized Experiments*, (48). <https://doi.org/10.3791/2761>
- Colsenet, R., Mariette, F., & Cambert, M. (2005). NMR relaxation and water self-diffusion studies in whey protein solutions and gels. *Journal of Agricultural and Food Chemistry*, 53(17), 6784–6790. <https://doi.org/10.1021/jf050162k>
- Copen, W. A., Schwamm, L. H., González, R. G., Wu, O., Harmath, C. B., Schaefer, P. W., ... Sorensen, A. G. (2001). Ischemic stroke: Effects of etiology and patient age on the time course of the core apparent diffusion coefficient. *Radiology*, 221(1), 27–34. <https://doi.org/10.1148/radiol.2211001397>
- Copen, William A., Schaefer, P. W., & Wu, O. (2011). MR Perfusion Imaging in Acute Ischemic Stroke. *Neuroimaging Clinics of North America*, 21(2), 259–283. <https://doi.org/10.1016/j.nic.2011.02.007>
- Cory, D. G., Miller, J. B., Turner, R., & Garroway, A. N. (1990). Multiple-pulse methods of <sup>1</sup>H N.M.R. imaging of solids: Second-averaging. *Molecular Physics*, 70(2), 331–345. <https://doi.org/10.1080/00268979000101031>
- Danial, N. N., & Korsmeyer, S. J. (2004). Cell Death : Critical Control Points Review. *Cell Press*, 116, 205–219.
- de Graaf, R. A. (2018). *In Vivo NMR Spectroscopy: Principles and Techniques* (3rd Editio). Wiley-Blackwell.
- Dijkhuizen, R. M., Ren, J., Mandeville, J. B., Wu, O., Ozdag, F. M., Moskowitz, M. A., ... Finklestein, S. P. (2001). Functional magnetic resonance imaging of reorganization in rat brain after stroke. *Proceedings of the National Academy of Sciences of the United States of America*, 98(22), 12766–12771. <https://doi.org/10.1073/pnas.231235598>
- Dijkhuizen, R. M., Singhal, A. B., Mandeville, J. B., Wu, O., Halpern, E. F., Finklestein, S. P., ... Lo,

- E. H. (2003). Correlation between brain reorganization, ischemic damage, and neurologic status after transient focal cerebral ischemia in rats: A functional magnetic resonance imaging study. *Journal of Neuroscience*, 23(2), 510–517. <https://doi.org/10.1523/jneurosci.23-02-00510.2003>
- Ding, G., Jiang, Q., Li, L., Zhang, L., Gang Zhang, Z., Ledbetter, K. A., ... Chopp, M. (2006). Detection of BBB disruption and hemorrhage by Gd-DTPA enhanced MRI after embolic stroke in rat. *Brain Research*, 1114(1), 195–203. <https://doi.org/10.1016/j.brainres.2006.07.116>
- Dirnagl, U., & Walz, W. (2016). Rodent Models of Stroke. In *Neuromethods* (Vol. 120).
- Donnan, G. A., Fisher, M., Macleod, M., & M Davis, S. (2009). Stroke. *The Lancet*, 373(9674), 14612–14623. [https://doi.org/10.1016/S0140-6736\(09\)60833-3](https://doi.org/10.1016/S0140-6736(09)60833-3)
- Einstein, A. (1905). INVESTIGATIONS ON THE THEORY OF THE BROWNIAN MOVEMENT. *DOVER PUBLICATIONS*. <https://doi.org/10.1016/j.chroma.2008.07.021>
- Fieremans, E., Jensen, J. H., & Helpert, J. A. (2011). White matter characterization with diffusional kurtosis imaging. *NeuroImage*, 58(1), 177–188. <https://doi.org/10.1016/j.neuroimage.2011.06.006>
- Franklin, K., & Paxinos, G. (2019). *Paxinos and Franklin's the Mouse Brain in Stereotaxic Coordinates* (5th ed.).
- Garyfallidis, E., Brett, M., Amirbekian, B., Rokem, A., van der Walt, S., Descoteaux, M., & Nimmo-Smith, I. (2014). Dipy, a library for the analysis of diffusion MRI data. *Frontiers in Neuroinformatics*, 8. <https://doi.org/10.3389/fninf.2014.00008>
- Ginsberg, M. D. (2003). Adventures in the pathophysiology of brain ischemia: Penumbral, gene expression, neuroprotection: The 2002 Thomas Willis lecture. *Stroke*, 34(1), 214–223. <https://doi.org/10.1161/01.STR.0000048846.09677.62>
- Gonza, R. G., Schaefer, P. W., Buonanno, F. S., Schwamm, L. H., Budzik, R. F., Rordorf, G., ... Koroshetz, W. J. (1999). Diffusion-weighted MR Imaging: Diagnostic Accuracy in Patients Imaged within 6 Hours of Stroke Symptom Onset. *Radiology*, 155–162.
- González, R. G., Hirsch, J. A., Lev, M. H., Schaefer, P. W., & Schwamm, L. H. (2011). *Acute Ischemic Stroke* (Second Edi; R. G. González, J. A. Hirsch, M. H. Lev, P. W. Schaefer, & L. H. Schwamm, Eds.). <https://doi.org/10.1007/978-3-642-12751-9>
- Granziera, C., D'Arceuil, H., Zai, L., Magistretti, P. ., Sorensen, A. ., & de Crespigny, A. . (2007). Long-Term Monitoring of Post-Stroke Plasticity After Transient Cerebral Ischemia in Mice Using In Vivo and Ex Vivo Diffusion Tensor MRI. *The Open Neuroimaging Journal*, 1, 10–17. <https://doi.org/10.2174/1874440000701010010>
- Grysiewicz, R. A., Thomas, K., & Pandey, D. K. (2008). Epidemiology of Ischemic and Hemorrhagic Stroke: Incidence, Prevalence, Mortality, and Risk Factors. *Neurologic Clinics*, 26(4), 871–895. <https://doi.org/10.1016/j.ncl.2008.07.003>
- Guizar-sicairos, M., Thurman, S. T., & Fienup, J. R. (2008). Guizar\_Efficient\_subpixel\_. *Optics Letters*, 33(2), 156–158.
- Hahn, E. L. (1950). Spinechoes. *Phys Rev Lett*, Vol. 80, pp. 580–594.
- Heiss, W., Kracht, L. W., Thiel, A., Grond, M., & Pawlik, G. (2001). *Penumbral probability thresholds of cortical flumazenil binding and blood flow predicting tissue outcome in pateints with cerebral ischemia.pdf*>. 20–29.
- Helpert, J. A., Dereski, M. O., Knight, R. A., Ordidge, R. J., Chopp, M., & Qing, Z. X. (1993). Histopathological correlations of nuclear magnetic resonance imaging parameters in experimental cerebral ischemia. *Magnetic Resonance Imaging*, 11(2), 241–246. [https://doi.org/10.1016/0730-725X\(93\)90028-C](https://doi.org/10.1016/0730-725X(93)90028-C)
- Henriques, R. N. (2018). *Advanced Methods for Diffusion MRI Data Analysis and their Application to the Healthy Ageing Brain* (Cambridge University). <https://doi.org/10.17863/CAM.29356>
- Henriques, R. N., Jespersen, S. N., & Shemesh, N. (2019). Microscopic anisotropy misestimation in spherical-mean single diffusion encoding MRI. *Magnetic Resonance in Medicine*, 81(5), 3245–3261. <https://doi.org/10.1002/mrm.27606>
- Henriques, R. N., Jespersen, S. N., & Shemesh, N. (2020). Correlation tensor magnetic resonance imaging. *NeuroImage*, 211(January). <https://doi.org/10.1016/j.neuroimage.2020.116605>
- Hermann, D. M., & Doeppner, T. R. (2016). From Bedside to Bench : How Clinical Reality Should Instruct Stroke Modeling. In U. Dirnagl (Ed.), *Rodent Models of Stroke* (Second, Vol. 120, pp. 1–6). <https://doi.org/10.1007/978-1-4939-5620-3>

- Horsfield, M. A., & Jones, D. K. (2002). Applications of diffusion-weighted and diffusion tensor MRI to white matter diseases - A review. *NMR in Biomedicine*, 15(7–8), 570–577. <https://doi.org/10.1002/nbm.787>
- Hossmann, K. A. (2006). Pathophysiology and therapy of experimental stroke. *Cellular and Molecular Neurobiology*, 26(7–8), 1057–1083. <https://doi.org/10.1007/s10571-006-9008-1>
- Hossmann, K. A., & Mies, G. (2007). Multimodal Mapping of the Ischemic Penumbra in Animal Models. In G. A. Donnan, J. C. Baron, S. M. Davis, & F. R. Sharp (Eds.), *The Ischemic Penumbra* (pp. 77–92). Informa Healthcare.
- Howells, D. W., Porritt, M. J., Rewell, S. S., O’Collins, V., Sena, E. S., van der Worp, H. B., ... Macleod, M. R. (2010). Different Strokes for Different Folks: The Rich Diversity of Animal Models of Focal Cerebral Ischemia. *Journal of Cerebral Blood Flow & Metabolism*, 30(8), 1412–1431. <https://doi.org/10.1038/jcbfm.2010.66>
- Huettel, S. A., Song, A. W., & McCarthy, G. (2014). Functional Magnetic Resonance Imaging, Third Edition. In *Functional Magnetic Resonance Imaging, Third Edition*. <https://doi.org/10.1088/1475-7516/2003/08/005>
- Hui, E. S., Fieremans, E., Jensen, J. H., Tabesh, A., Feng, W., Bonilha, L., ... Helpert, J. A. (2012). Stroke assessment with diffusional kurtosis imaging. *Stroke*, 43(11), 2968–2973. <https://doi.org/10.1161/STROKEAHA.112.657742>
- Jablonka, J. A., Witte, O. W., & Kossut, M. (2007). Photothrombotic infarct impairs experience-dependent plasticity in neighboring cortex. *NeuroReport*, 18(2), 165–169. <https://doi.org/10.1097/WNR.0b013e328010feff>
- Jensen, J. H., & Helpert, J. A. (2010). MRI quantification of non-Gaussian water diffusion by kurtosis analysis. *NMR in Biomedicine*, 23(7), 698–710. <https://doi.org/10.1002/nbm.1518>
- Jensen, J. H., Helpert, J. A., Ramani, A., Lu, H., & Kaczynski, K. (2005). Diffusional kurtosis imaging: The quantification of non-Gaussian water diffusion by means of magnetic resonance imaging. *Magnetic Resonance in Medicine*, 53(6), 1432–1440. <https://doi.org/10.1002/mrm.20508>
- Jespersen, S. N. (2012). Equivalence of double and single wave vector diffusion contrast at low diffusion weighting. *NMR in Biomedicine*, (September 2011), 813–818. <https://doi.org/10.1002/nbm.1808>
- Jespersen, S. N., Lundell, H., Sønderby, C. K., & Dyrby, T. B. (2013). Orientationally invariant metrics of apparent compartment eccentricity from double pulsed field gradient diffusion experiments. *NMR in Biomedicine*, 26(12), 1647–1662. <https://doi.org/10.1002/nbm.2999>
- Jiang, Q., Chopp, M., Zhang, Z. G., Knight, R. A., Jacobs, M., Windham, J. P., ... Welch, K. M. A. (1997). The temporal evolution of MRI tissue signatures after transient middle cerebral artery occlusion in rat. *Journal of the Neurological Sciences*, 145(1), 15–23. [https://doi.org/10.1016/S0022-510X\(96\)00286-9](https://doi.org/10.1016/S0022-510X(96)00286-9)
- Kellner, E., Dhital, B., Kiselev, V. G., & Reiser, M. (2016). Gibbs-ringing artifact removal based on local subvoxel-shifts. *Magnetic Resonance in Medicine*, 76(5), 1574–1581. <https://doi.org/10.1002/mrm.26054>
- Labat-gest, V., & Tomasi, S. (2013). Photothrombotic ischemia: a minimally invasive and reproducible photochemical cortical lesion model for mouse stroke studies. *Journal of Visualized Experiments : JoVE*, (76), 1–6. <https://doi.org/10.3791/50370>
- Latour, L. L., Svoboda, K., Mitra, P. P., & Sotak, C. H. (1994). Time-dependent diffusion of water in a biological model system. *Proceedings of the National Academy of Sciences of the United States of America*, 91(4), 1229–1233. <https://doi.org/10.1073/pnas.91.4.1229>
- Lauterbur, P. (1973). Image Formation by Induced Local Interactions: Examples Employing Nuclear Magnetic Resonance. *Nat. Phys. Sci.*, 241, 20.
- Le Bihan, D., & Johansen-Berg, H. (2012). Diffusion MRI at 25: Exploring brain tissue structure and function. *NeuroImage*, 61(2), 324–341. <https://doi.org/10.1016/j.neuroimage.2011.11.006>
- Ljunggren, S. (1983). A simple graphical representation of fourier-based imaging methods. *Journal of Magnetic Resonance (1969)*, 54(2), 338–343. [https://doi.org/10.1016/0022-2364\(83\)90060-4](https://doi.org/10.1016/0022-2364(83)90060-4)
- Lodder, J. (1984). CT-detected hemorrhagic infarction ; relation with the size of the infarct , and the presence of midline shift. *Acta Neurol Scand*, 329–335.
- Longa, E. Z., Weinstein, P. R., Carlson, S., & Cummins, R. (1989). Reversible middle cerebral artery occlusion without craniectomy in rats. *Stroke*, 20(1), 84–91. <https://doi.org/10.1161/01.STR.20.1.84>



- Macrae, I. (2011). Preclinical stroke research - advantages and disadvantages of the most common rodent models of focal ischaemia. *British Journal of Pharmacology*, 164(4), 1062–1078. <https://doi.org/10.1111/j.1476-5381.2011.01398.x>
- Macrae, I. M., Robinson, M. J., Graham, D. I., Reid, J. L., & McCulloch, J. (1993). Endothelin-1-Induced Reductions in Cerebral Blood Flow: Dose Dependency, Time Course, and Neuropathological Consequences. *Journal of Cerebral Blood Flow & Metabolism*, 13(2), 276–284. <https://doi.org/10.1038/jcbfm.1993.34>
- Meng, X., Fisher, M., Shen, Q., Sotak, C. H., & Duong, T. Q. (2004). Characterizing the Diffusion/Perfusion Mismatch in Experimental Focal Cerebral Ischemia. *Annals of Neurology*, (1), 207–212. <https://doi.org/10.1002/ana.10803>
- Merino, J. G., & Warach, S. (2010). Imaging of acute stroke. *Nature Publishing Group*, 6(10), 560–571. <https://doi.org/10.1038/nrneurol.2010.129>
- Mhairi, M. I. (1992). New models of focal cerebral ischaemia. *British Journal of Clinical Pharmacology*, 34(4), 302–308. <https://doi.org/10.1111/j.1365-2125.1992.tb05634.x>
- Mitra, P. P. (1995). Multiple wave-vector extensions of the NMR pulsed-field-gradient spin-echo diffusion measurement. *Physical Review*, 51(21), 74–78.
- Mohr, J. P., Biller, J., Hilal, S. K., Yuh, W. T. C., Tatemichi, T. K., Tali, E., ... Marler, J. R. (1995). *Magnetic Resonance Versus Computed Tomographic Imaging in Acute Stroke*. 26(5), 807–812.
- Morancho, A., García-Bonilla, L., Barceló, V., Giralt, D., Campos-Martorell, M., Garcia, S., ... Rosell, A. (2012). A new method for focal transient cerebral ischaemia by distal compression of the middle cerebral artery. *Neuropathology and Applied Neurobiology*, 38(6), 617–627. <https://doi.org/10.1111/j.1365-2990.2012.01252.x>
- Moseley, M. E., Cohen, Y., Mintorovitch, J., Chileuitt, L., Shimizu, H., Kucharczyk, J., ... Weinstein, P. R. (1990). Early detection of regional cerebral ischemia in cats: Comparison of diffusion- and T2-weighted MRI and spectroscopy. *Magnetic Resonance in Medicine*, 14(2), 330–346. <https://doi.org/10.1002/mrm.1910140218>
- Moseley, M. E., Kucharczyk, J., Mintorovitch, J., Cohen, Y., Kurhanewicz, J., Derugin, N., ... Norman, D. (1990). Diffusion-weighted MR imaging of acute stroke: Correlation with T2-weighted and magnetic susceptibility-enhanced MR imaging in cats. *American Journal of Neuroradiology*, 11(3), 423–429.
- Murphy, T. H., & Corbett, D. (2009). Plasticity during stroke recovery: From synapse to behaviour. *Nature Reviews Neuroscience*, 10(12), 861–872. <https://doi.org/10.1038/nrn2735>
- Murphy, T. H., Li, P., Betts, K., & Liu, R. (2008). Two-photon imaging of stroke onset in vivo reveals that NMDA-receptor independent ischemic depolarization is the major cause of rapid reversible damage to dendrites and spines. *Journal of Neuroscience*, 28(7), 1756–1772. <https://doi.org/10.1523/JNEUROSCI.5128-07.2008>
- Neumann-Haefelin, T., Kastrup, A., de Crespigny, A., Yenari, M. A., Ringer, T., Sun, G. H., & Moseley, M. E. (2000). Serial MRI After Transient Focal Cerebral Ischemia in Rats. *Stroke*, 31(8), 1965–1973. <https://doi.org/10.1161/01.str.31.8.1965>
- Niendorf, T., Dijkhuizen, R. M., Norris, D. G., Campagne, M. V. L., & Nicolay, K. (1996). Biexponential Diffusion Attenuation in Various States of Brain Tissue : Implications for Diffusion-Weighted Imaging. *Magnetic Resonance in Medicine*, 36(6), 847–857.
- Norrving, B. (2014). Oxford Textbook of Stroke and Cerebrovascular Disorders. In *Oxford* (Vol. 53). <https://doi.org/10.1017/CBO9781107415324.004>
- Novikov, D. S., Kiselev, V. G., & Jespersen, S. N. (2018). On modeling. *Magnetic Resonance in Medicine*, (June 2017), 3172–3193. <https://doi.org/10.1002/mrm.27101>
- Nowicka, D., Rogozinska, K., Aleksy, M., Witte, O. W., & Skangiel-Kramska, J. (2008). Spatiotemporal dynamics of astroglial and microglial responses after photothrombotic stroke in the rat brain. *Acta Neurobiologiae Experimentalis*, 68(2), 155–168. Retrieved from <http://www.ncbi.nlm.nih.gov/pubmed/18511952>
- Pillai, D. R., Dittmar, M. S., Baldaranov, D., Heidemann, R. M., Henning, E. C., Schuierer, G., ... Schlachetzki, F. (2009). Cerebral Ischemia-Reperfusion Injury in Rats—A 3 T MRI Study on Biphasic Blood-Brain Barrier Opening and the Dynamics of Edema Formation. *Journal of Cerebral Blood Flow & Metabolism*, 29(11), 1846–1855. <https://doi.org/10.1038/jcbfm.2009.106>
- Porritt, M. J., Pekna, M., Pekny, M., Andersson, H. C., Hou, L., & Nilsson, M. (2012). Photothrombosis-

- Induced Infarction of the Mouse Cerebral Cortex Is Not Affected by the Nrf2-Activator Sulforaphane. *PLoS ONE*, 7(7), 17–19. <https://doi.org/10.1371/journal.pone.0041090>
- Prinz, V., & Endres, M. (2016). *Modeling Focal Cerebral Ischemia in Rodents: Introduction and Overview*. 120, 19. <https://doi.org/10.1007/978-1-4939-5620-3>
- Qian, C., Li, P. C., Jiao, Y., Yao, H. H., Chen, Y. C., Yang, J., ... Teng, G. J. (2016). Precise characterization of the penumbra revealed by MRI: A modified photothrombotic stroke model study. *PLoS ONE*, 11(4), 1–13. <https://doi.org/10.1371/journal.pone.0153756>
- Quast, M. J., Huang, N. C., Hillman, G. R., & Kent, T. A. (1993). The evolution of acute stroke recorded by multimodal magnetic resonance imaging. *Magnetic Resonance Imaging*, 11(4), 465–471. [https://doi.org/10.1016/0730-725X\(93\)90465-P](https://doi.org/10.1016/0730-725X(93)90465-P)
- Rosenblum, W. I., & El-Sabban, F. (1977). Platelet Aggregation in the Cerebral Microcirculation Effect of Aspirin and Other Agents. *Circulation Research*, 40(3).
- Roth, J. M. (2011). Recombinant Tissue Plasminogen Activator for the Treatment of Acute Ischemic Stroke. *Baylor University Medical Center Proceedings*, 24(3), 257–259. <https://doi.org/10.1080/08998280.2011.11928729>
- Russel, E. J. (1997). Diagnosis of Hyperacute Ischemic Infarct with CT: Key to Improved Clinical Outcome after Intravenous Thrombolysis? *Radiology*, 315–318.
- Sarkar, S., Ghosh, S., Ghosh, S. K., & Collier, A. (2007). Role of transcranial Doppler ultrasonography in stroke. *Postgraduate Medical Journal*, 83(985), 683–689. <https://doi.org/10.1136/pgmj.2007.058602>
- Schröder, H., Moser, N., & Huggenberger, S. (2020). The Mouse Circle of Willis. In *Neuroanatomy of the Mouse* (pp. 333–340). [https://doi.org/10.1007/978-3-030-19898-5\\_15](https://doi.org/10.1007/978-3-030-19898-5_15)
- Sharkey, J. (1993). Perivascular Microapplication of Endothelin-1: A New Model of Focal Cerebral Ischaemia in the Rat. *Journal of Cerebral Blood Flow & Metabolism*, 13(5), 865–871. <https://doi.org/10.1038/jcbfm.1993.108>
- Shemesh, N., Jespersen, S. N., Alexander, D. C., Cohen, Y., Drobnjak, I., Dyrby, T. B., ... Mitra, P. P. (2016). Conventions and Nomenclature for Double Diffusion Encoding NMR and MRI. *Magnetic Resonance in Medicine*, 87(April 2015), 82–87. <https://doi.org/10.1002/mrm.25901>
- Shemesh, N., Rosenberg, J. T., Dumez, J. N., Muniz, J. A., Grant, S. C., & Frydman, L. (2014). Metabolic properties in stroked rats revealed by relaxation-enhanced magnetic resonance spectroscopy at ultrahigh fields. *Nature Communications*, 5, 1–8. <https://doi.org/10.1038/ncomms5958>
- Shigeno, T., Teasdale, G. M., McCulloch, J., & Graham, D. I. (1985). Recirculation model following MCA occlusion in rats. *Journal of Neurosurgery*, 63(2), 272–277. <https://doi.org/10.3171/jns.1985.63.2.0272>
- Sorensen, A. G., Wu, O., Copen, W. A., Davis, T. L., Gonzalez, R. G., Koroshetz, W. J., ... Weisskoff, R. M. (1999). Human Acute Cerebral Ischemia: Detection of Changes in Water Diffusion Anisotropy by Using MR Imaging. *Radiology*, 212(3), 785–792. <https://doi.org/10.1148/radiology.212.3.r99se24785>
- Sotak, C. H. (2002). The role of diffusion tensor imaging in the evaluation of ischemic brain - A review. *NMR in Biomedicine*, 15(7–8), 561–569. <https://doi.org/10.1002/nbm.786>
- Srinivasan, A., Goyal, M., Azri, F. Al, & Lum, C. (2006). State-of-the-art imaging of acute stroke. *Radiographics*, 48109, 75–96.
- Stejskal, E. O. (1965). Use of Spin Echoes in a Pulsed Magnetic-Field Gradient to Study Anisotropic, Restricted Diffusion and Flow. *The Journal of Chemical Physics*, 43(10), 3597–3603. <https://doi.org/10.1063/1.1696526>
- Stejskal, E. O., & Tanner, J. E. (1965). Spin diffusion measurements: Spin echoes in the presence of a time-dependent field gradient. *The Journal of Chemical Physics*, 42(1), 288–292. <https://doi.org/10.1063/1.1695690>
- Szczepankiewicz, F., Eriksson, S., Nilsson, M., Topgaard, D., & Lasi, S. (2014). Microanisotropy imaging : quantification of microscopic diffusion anisotropy and orientational order parameter by diffusion MRI with magic-angle spinning of the q-vector. *Frontiers in Physics*, 2(February), 1–14. <https://doi.org/10.3389/fphy.2014.00011>
- Tamura, A., Graham, D. I., McCulloch, J., & Teasdale, G. M. (1981). Focal Cerebral Ischaemia in the Rat: 1. Description of Technique and Early Neuropathological Consequences following Middle

- Cerebral Artery Occlusion. *Journal of Cerebral Blood Flow & Metabolism*, 1(1), 53–60. <https://doi.org/10.1038/jcbfm.1981.6>
- Torrey, H. C. (1956). Bloch Equations with Diffusion Terms. *Physical Review*, 104(3), 563–565.
- Umesh Rudrapatna, S., Wieloch, T., Beirup, K., Ruscher, K., Mol, W., Yanev, P., ... Dijkhuizen, R. M. (2014). Can diffusion kurtosis imaging improve the sensitivity and specificity of detecting microstructural alterations in brain tissue chronically after experimental stroke? Comparisons with diffusion tensor imaging and histology. *NeuroImage*, 97, 363–373. <https://doi.org/10.1016/j.neuroimage.2014.04.013>
- van Bruggen, N., Thibodeaux, H., Palmer, J. T., Lee, W. P., Fu, L., Cairns, B., ... Ferrara, N. (1999). VEGF antagonism reduces edema formation and tissue damage after ischemia/reperfusion injury in the mouse brain. *Journal of Clinical Investigation*, 104(11), 1613–1620. <https://doi.org/10.1172/JCI8218>
- van der Zijden, J. P., van der Toorn, A., van der Marel, K., & Dijkhuizen, R. M. (2008). Longitudinal in vivo MRI of alterations in perilesional tissue after transient ischemic stroke in rats. *Experimental Neurology*, 212(1), 207–212. <https://doi.org/10.1016/j.expneurol.2008.03.027>
- van Meer, M. P. A., Otte, W. M., van der Marel, K., Nijboer, C. H., Kavelaars, A., van der Sprenkel, J. W. B., ... Dijkhuizen, R. M. (2012). Extent of bilateral neuronal network reorganization and functional recovery in relation to stroke severity. *Journal of Neuroscience*, 32(13), 4495–4507. <https://doi.org/10.1523/JNEUROSCI.3662-11.2012>
- Veraart, J., Novikov, D. S., Christiaens, D., Ades-aron, B., Sijbers, J., & Fieremans, E. (2016). Denoising of diffusion MRI using random matrix theory. *NeuroImage*, 142, 394–406. <https://doi.org/10.1016/j.neuroimage.2016.08.016>
- Veraart, J., Sijbers, J., Sunaert, S., Leemans, A., & Jeurissen, B. (2013). Weighted linear least squares estimation of diffusion MRI parameters: Strengths, limitations, and pitfalls. *NeuroImage*, 81, 335–346. <https://doi.org/10.1016/j.neuroimage.2013.05.028>
- Watson, B. D., Dietrich, W. D., Busto, R., Wachtel, M. S., & Ginsberg, M. D. (1985). Induction of reproducible brain infarction by photochemically initiated thrombosis. *Annals of Neurology*, 17(5), 497–504. <https://doi.org/10.1002/ana.410170513>
- Webb, A. (2003). *Introduction to biomedical imaging*. <https://doi.org/10.1109/issmddb.2008.4574999>
- Welch, K. M. A., Windham, J., Knight, R. A., Nagesh, V., Hugg, J. W., Jacobs, M., ... Levine, S. R. (1995). A Model to Predict the Histopathology of Human Stroke Using Diffusion and T2-Weighted Magnetic Resonance Imaging. *Stroke*, 26(11), 1983–1989.
- Wey, H.-Y., Desai, V. R., & Duong, T. Q. (2014). A review of current imaging methods used in stroke research. *Neurological Research*, 35(10), 1092–1102. <https://doi.org/10.1179/1743132813Y.0000000250.A>
- Wey, H. Y., Desai, V. R., & Duong, T. Q. (2013). A review of current imaging methods used in stroke research. *Neurological Research*, 35(10), 1092–1102. <https://doi.org/10.1179/1743132813Y.0000000250>
- Wu, O., Chutinet, A., & Bayrlee, A. (2010). Diffusion In Acute Stroke. In D. Jones (Ed.), *Diffusion MRI: Theory, Methods, and Applications* (1st ed., pp. 518–525). <https://doi.org/10.1093/med/9780195369779.001.0001>
- Xing, C., Arai, K., Lo, E. H., & Hommel, M. (2012). Pathophysiologic cascades in ischemic stroke. *International Journal of Stroke*, 7(5), 378–385. <https://doi.org/10.1111/j.1747-4949.2012.00839.x>
- Yardeni, T., Eckhaus, M., Morris, H. D., Huizing, M., & Hoogstraten-Miller, S. (2011). Retro-orbital injections in mice. *Lab Animal*, 40(5), 155–160. <https://doi.org/10.1038/labana0511-155>
- Yuh, W. T., Crain, M. R., Loes, D. J., Greene, G. M., Ryals, T. J., & Sato, Y. (1991). MR imaging of cerebral ischemia: findings in the first 24 hours. *AJNR. American Journal of Neuroradiology*, 12(4), 621–629. Retrieved from <http://www.ncbi.nlm.nih.gov/pubmed/1688348>
- Zhuo, J., Xu, S., Proctor, J. L., Mullins, R. J., Simon, J. Z., Fiskum, G., & Gullapalli, R. P. (2012). Diffusion kurtosis as an in vivo imaging marker for reactive astrogliosis in traumatic brain injury. *NeuroImage*, 59(1), 467–477. <https://doi.org/10.1016/j.neuroimage.2011.07.050>



## 8. Appendix

The developed work in the course of this project was accepted to be presented at the following conferences:

1. “Brain Stroke: Why, how, and hope” – FENS Conference, 2020 (postponed to April 2021) Copenhagen, Denmark

Title: Mapping Microstructural Dynamics in a Mouse Stroke Model Using Advanced Diffusion MRI

Authors: Rita Alves, Rafael Henriques, Noam Shemesh

2. Innovate Competition – iMed Conference 12.0, 2020, Lisbon, Portugal

Title: Mapping Microstructural Dynamics in a Mouse Stroke Model Using Advanced Diffusion MRI

Authors: Rita Alves, Rafael Henriques, Noam Shemesh